

MASTER THESIS

Thesis submitted in partial fulfillment of the requirements for the degree of Master of Science in Engineering at the University of Applied Sciences Technikum Wien - Degree Program Medical Engineering & eHealth

Application, analysis and evaluation of novel medical image annotation and segmentation tools

By: Bc. Jan Sucháček
Student Number: 2310228017

Supervisor: Dr. Benjamin Ramberger, MSc. BSc. BSc.
FH-Prof. Ing. Richard Pasteka, MSc, PhD

Vienna, May 18, 2024

Author's Declaration

"As author and creator of this work to hand, I confirm with my signature knowledge of the relevant copyright regulations governed by higher education acts (see Urheberrechtsgesetz /Austrian copyright law as amended as well as the Statute on Studies Act Provisions / Examination Regulations of the UAS Technikum Wien as amended).

I hereby declare that I completed the present work independently and that any ideas, whether written by others or by myself, have been fully sourced and referenced. I am aware of any consequences I may face on the part of the degree program director if there should be evidence of missing autonomy and independence or evidence of any intent to fraudulently achieve a pass mark for this work (see Statute on Studies Act Provisions / Examination Regulations of the UAS Technikum Wien as amended).

I further declare that up to this date I have not published the work to hand nor have I presented it to another examination board in the same or similar form. I affirm that the version submitted matches the version in the upload tool."

Vienna, May 18, 2024

.....
Author's signature

Kurzfassung

In dieser Arbeit wird die Erstellung von 3D-Modellen der oberen Atemwege des Menschen anhand von CT-Scans untersucht, um das Verständnis komplexer anatomischer Details der oberen Atemwege zu verbessern, die Erkennung pathologischer Veränderungen zu unterstützen und therapeutische Entscheidungen zu erleichtern. Diese Modelle ermöglichen auch die Simulation und Bewertung der Luftstromeigenschaften in den oberen Atemwegen.

Zur Erstellung dieser 3D-Modelle wurden zwei Annotationen und drei Segmentierungsmethoden auf einen Datensatz von sechs Patienten-CT-Scans angewendet. Verschiedene Metriken wie die Anzahl der Dreiecke, die Oberfläche, das Volumen, das Modellschnittvolumen, der Dice-Koeffizient und der Modell-zu-Modell-Abstand wurden für alle resultierenden 3D-Modelle berechnet, um die Modelle zu charakterisieren und die Methoden zu vergleichen. Eine detaillierte Analyse konzentrierte sich auf vier anatomische Bereiche: Nasenhöhle mit Nebenhöhlen, Rachen, Kehlkopf und Luftröhre.

Zusätzlich wurde eine CFD-Simulation (Computational Fluid Dynamics) an einem Modell durchgeführt, um den Luftstrom in den oberen Atemwegen während der Atmung zu analysieren. Diese Simulation lieferte Einblicke in die Strömungsdynamik in den oberen Atemwegen, wodurch sich die Notwendigkeit invasiver Untersuchungen verringern könnte.

Die Ergebnisse dieser Arbeit zeigen das Potenzial von 3D-Modellen der oberen Atemwege zur Verbesserung der diagnostischen Genauigkeit, der Behandlungsplanung und der Patientenergebnisse in der Atemwegsmedizin.

Schlagworte

3D Modelle der oberen Atemwege, CT Scans, Bildsegmentierung, Bildbeschriftung, Computational Fluid Dynamics (CFD)

Abstract

This thesis explores the creation of 3D models of the human upper airways from CT scans to enhance the understanding of complex anatomical details of the upper airways, assist in detecting pathological changes, and facilitate therapeutic decision-making. These models also enable simulation and assessment of airflow characteristics within the human upper airways.

To generate these 3D models, two annotation and three segmentation methods were employed on a dataset of six patient CT scans. Various metrics, such as the number of triangles, surface area, volume, model intersection volume, Dice coefficient, and model-to-model distance, were calculated for all resulting 3D models to characterize the models and compare the methods. A detailed analysis focused on four anatomical parts: the nasal cavity with sinuses, pharynx, larynx, and trachea, was performed.

Additionally, a computational fluid dynamics (CFD) simulation was conducted on one model to analyze airflow in the upper airways during breathing. This simulation provided insights into airflow dynamics inside the upper airways, potentially reducing the need for invasive examinations.

The findings of this thesis demonstrate the potential of 3D upper airway models to improve diagnostic accuracy, treatment planning, and patient outcomes in respiratory medicine.

Keywords

3D Upper Airway Models, CT Scans, Image Segmentation, Image Annotation, Computational Fluid Dynamics (CFD)

SUCHÁČEK, Jan. *Application, analysis and evaluation of novel medical image annotation and segmentation tools*. Master's Thesis. Vienna: FH Technikum Wien, Faculty of Life Science Engineering, Medical Engineering & eHealth, 2024. Advised by Dr. Benjamin Ramberger, MSc. BSc. BSc.

ACKNOWLEDGEMENT

I would like to thank both of my supervisors, Dr. Benjamin Ramberger, MSc, BSc, BSc, and FH-Prof. Ing. Richard Pasteka, MSc, PhD, for providing valuable comments, sharing their expertise, and overall helpful attitude.

I would also like to thank René Donner, developer of the Medical Volume Annotator software, for his support and friendly cooperation in using this efficient annotation platform.

Contents

1	Introduction	9
1.1	Human Respiratory System	10
1.1.1	Upper Airway System	11
1.1.2	Lower Airway System	13
1.2	Image Segmentation	15
1.2.1	Segmentation by Intensity Homogeneity	15
1.2.2	Edge-Based Segmentation	16
1.2.3	Deep Learning-based Segmentation Methods	18
1.2.4	Metrics for Quantitative Assessment of Segmented 3D Models	21
1.3	Image Annotation	22
1.3.1	Types of Image Annotation	23
1.3.2	Image Annotation Techniques	26
1.4	Computational Fluid Dynamics	27
2	Material and Methods	30
2.1	Dataset	30
2.2	Annotation and Segmentation of the HUA	31
2.3	Methods for HUA Annotation	32
2.3.1	Medical Volume Annotator	32
2.3.2	V7	34
2.4	Methods for HUA Segmentation	35
2.4.1	3D Slicer	35
2.4.2	Synopsys Simpleware Software	38
2.4.3	3D U-Net Model for Automatic Segmentation of the Upper Airways	40
2.5	Spatial Registration of Models	42
2.6	Comparative Analysis	42
2.6.1	Quantitative Characterization of Models' Geometry	42
2.6.2	Characterization of Models' Geometry in Relation to the Tar- get Model	43
2.7	CFD Simulation	44
2.7.1	Repair of the Model	45
2.7.2	Definition of Model Boundaries	45
2.7.3	Meshing of the Model	46
2.7.4	CFD Simulation Computation	46

3	Results	48
3.1	Comparative Analysis	49
3.1.1	Quantitative Characterization of Models' Geometry	49
3.1.2	Characterization of Models' Geometry in Relation to the Target Model	53
3.1.3	Detailed Analysis of Upper Airway Models by Individual Anatomical Parts	58
3.2	CFD Simulation	65
3.2.1	Meshing of the Model	65
3.2.2	CFD Simulation Computation	66
4	Discussion	69
4.1	Methods for HUA Models Generation	69
4.1.1	Medical Volume Annotator	69
4.1.2	V7	69
4.1.3	3D Slicer	72
4.1.4	Simpleware Software	72
4.1.5	3D U-Net Model for Automatic Airway Segmentation	74
4.2	Spatial Registration of Models	75
4.3	Comparative Analysis	76
4.3.1	Quantitative Characterization of Models' Geometry	76
4.3.2	Characterization of Models' Geometry in Relation to the Target Model	76
4.4	Detailed Analysis of Upper Airway Models by Individual Anatomical Parts	78
4.4.1	Quantitative Characterization of Anatomical Parts' Geometry	80
4.4.2	Characterization of Anatomical Parts' Geometry in Relation to the Target Model	80
4.5	CFD Simulation	81
4.5.1	Repair of the Model and Definition of Model Boundaries	81
4.5.2	Meshing of the Model	82
4.5.3	CFD Simulation Computation	82
5	Conclusion	83
	Bibliography	84
	List of Abbreviations	92
	Appendix	94

1 Introduction

Respiratory diseases represent the third most common cause of death in EU countries, placing them among the most severe and life-threatening diseases alongside cardiovascular diseases and cancer [1]. Therefore, there is an effort to develop novel tools or improve existing ones to enable more precise, faster, and confident diagnosis of respiratory diseases.

Focusing on the upper airways, one of the most common diseases is upper airway obstruction, characterized by narrowing or occlusion (partial or complete) of the airways, potentially compromising ventilation [2]. Given the urgency of this issue, accurate segmentation or annotation of upper airway structures from CT/MRI scans, leading to the generation of 3D upper airway models, is crucial for understanding respiratory disorders. These 3D upper airway models enable healthcare professionals to fully understand the complexities and intricate anatomical details of the upper airways, aiding in the detection of life-threatening pathological changes. Compared to the 2D slice-by-slice approach of evaluating CT/MRI scans, 3D models of the upper airway offer physicians a much more detailed anatomical overview and better spatial orientation, facilitating faster and more precise diagnoses. Additionally, 3D models of the upper airway can be used for planning surgical interventions or educational purposes. Furthermore, the simulation of airflow in the upper airway model helps to understand what happens inside the airway during breathing, potentially reducing the need for invasive examinations to assess the severity of respiratory tract diseases. Such simulations of airflow in upper airway models can also be utilized to assess surgical outcomes.

Since manual annotation and segmentation of upper airways are very time-consuming and prone to errors, efforts have been made to employ semi-automatic and automatic tools, which provide more stable and reliable results in significantly shorter time. In this thesis, two different methods for annotation and three methods for segmentation of human upper airways were utilized for the generation of 3D upper airway models from CT scans. Additionally, the five methods used were compared based on the metrics calculated from the resulting upper airway models. Computational fluid dynamics simulation (CFD) of airflow was performed for one of the upper airway models.

The first chapter of this thesis provides a comprehensive theoretical overview of the human respiratory system anatomy and physiology, image segmentation and annotation techniques, and computational fluid dynamics. The second chapter covers a detailed description of the practical work, including dataset description, methods used for annotation and segmentation of the human upper airway, metrics used for comparative analysis, an explanation of all the steps involved in CFD simulation.

The third chapter of this thesis presents metrics calculated for all the resulting upper airway models, followed by a comparison of the five methods used for generation of these models. A more detailed analysis of anatomical parts of upper airway models created from one CT scan by the five methods was performed, and quantitative metrics were calculated and presented. The fourth chapter discusses all the outcomes and functionality of specific methods and tools used in this work.

1.1 Human Respiratory System

The human respiratory system is a complex and essential network of organs responsible for the exchange of gases - oxygen and carbon dioxide. Each organ in this complex system plays crucial role in inspiration and supply of oxygen and elimination of carbon dioxide [3, 4].

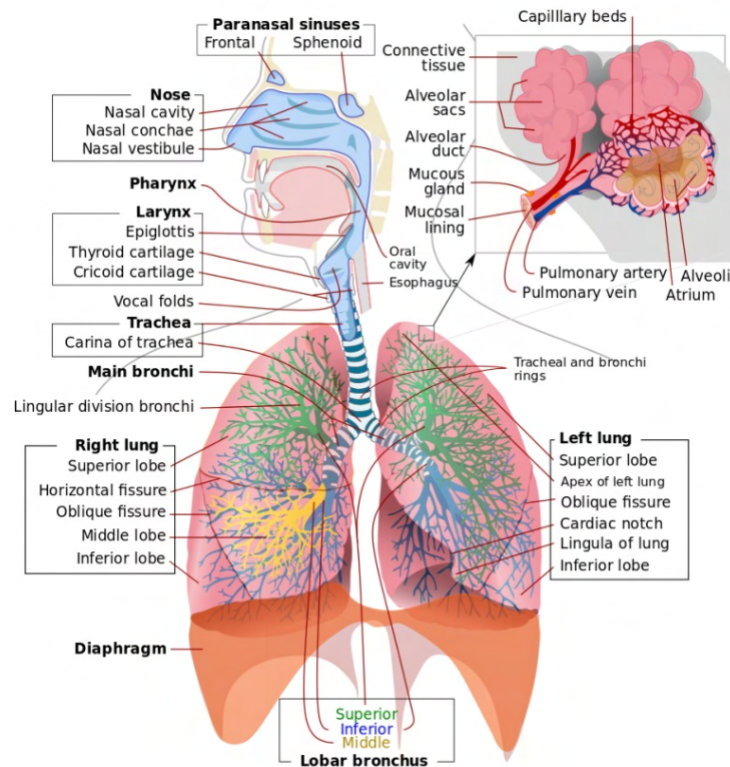


Fig. 1.1: Scheme of human respiratory system [5].

Anatomically, the respiratory system has two main parts: the upper airway system and lower airway system [3, 4].

- **The upper airway system (UAS)** comprises the nasal cavity, oral cavity, pharynx, larynx - see Figure 1.2. The upper airway has an important role in

transporting inhaled air to the lungs and its main functions include phonation, olfaction, digestion and also filtration, humidification and warming of the inhaled air.

- **The lower airway system (LAS)** is composed of the trachea, bronchi, bronchioles, alveolar duct and alveoli. All these structures, except the trachea, are contained in the left and the right lung - see Figure 1.3. The main function of the LAS is conducting and gas exchange.

1.1.1 Upper Airway System

The upper respiratory tract commence with the nasal cavity and extend through the nasopharynx and oropharynx, reaching the larynx and the extrathoracic trachea [3, 4].

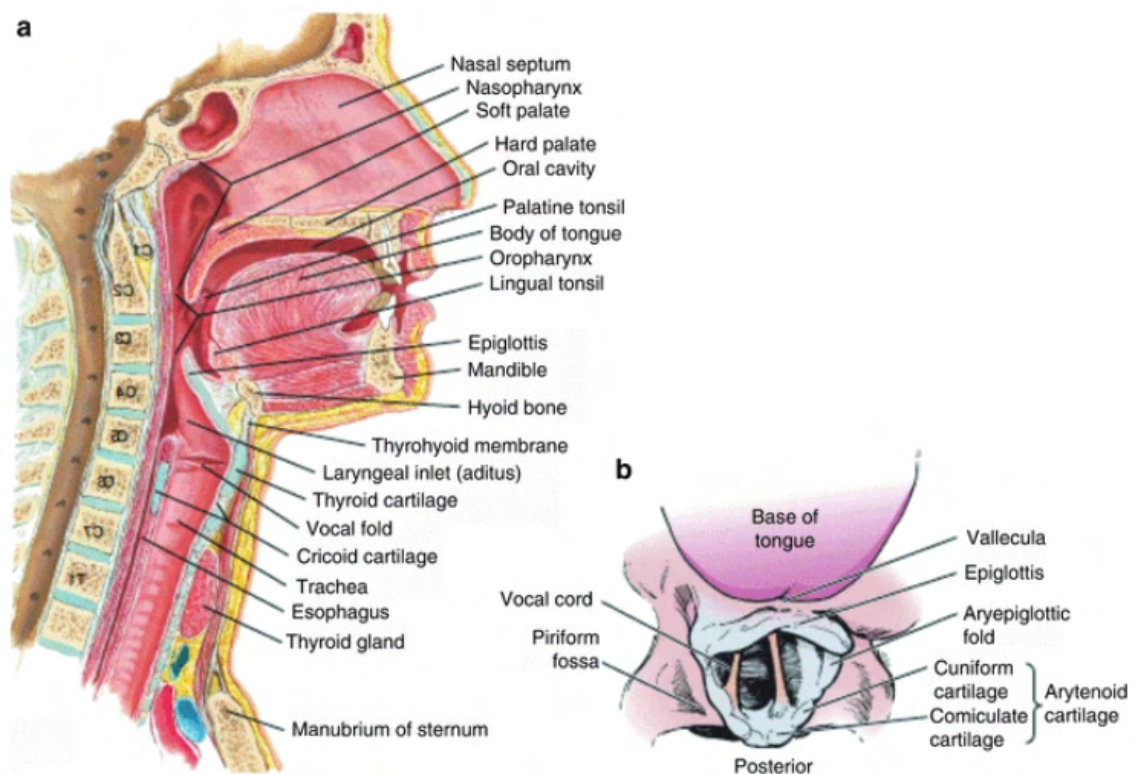


Fig. 1.2: Human upper airway system. a) sagittal view of the upper airway anatomy. b) anatomy of the larynx and vocal cords as seen through laryngoscopy [6].

The Nose and Nasal Cavity

The nose serves as the initial entry point for inhaled air and with nasal cavity plays a crucial role in conditioning and filtering the inhaled air before it reaches the lower respiratory tract. The nose consists of a bridge, tip, and nostrils. The nasal

cavity is divided into two separate compartments by the nasal bony and cartilaginous septum. Inside the nasal cavity, there is a lining with a specialized mucous membrane containing ciliated cells and goblet cells. The main function of goblet cells is the production of mucus, which serves as a protective barrier which traps particles and microorganisms from the inhaled air. Under the mucous membrane is a dense network of blood vessels that warms the inhaled air and helps maintain optimal temperature and humidity. In addition, the nose is equipped with a wide range of olfactory receptors that contribute to our sense of smell [3, 4].

The Pharynx

The air flows from the nasal cavity through the oral cavity to the pharynx. The pharynx is a muscular tube about 13 cm long, which is connecting the nasal cavity and the oral cavity to the larynx and esophagus. The pharynx is divided into three sections. The nasopharynx is superior part and is located behind the nasal cavity. In the nasopharynx are the adenoids, a lymphoid tissue, which play an important role in immune defense of organism. There is also structure called Eustachian tube that connects the middle ear to the nasopharynx and equalizes ear pressure. The oropharynx is middle part and is directly connected to the oral cavity, extends from the soft palate to the epiglottis. Another part of immune system, called the palatine tonsils, is located in the lateral walls of the oropharynx. The oropharynx also serves as a common pathway for both air and food. The laryngopharynx is positioned below the oropharynx and extends to the larynx. The laryngopharynx divides into the trachea and esophagus, before the point of diverging the laryngopharynx is common pathway for both air and food. To prevent food and water entering the trachea during swallowing, the epiglottis closes the entrance to the larynx [3, 4].

The Epiglottis

The epiglottis, a cartilaginous flap-like structure situated in the larynx and connected to the thyroid cartilage, plays a crucial role in swallowing by sealing the laryngeal inlet. Its primary purpose is to safeguard the lungs from the entry of water and food during the swallowing process [3, 4].

The Larynx

The larynx is positioned between the pharynx and the trachea. The larynx is composed of cartilages, muscles, and ligaments, which collectively carry out diverse functions such as safeguarding the airway and facilitating phonation. Besides conducting the air into the lungs and airway protection function, in the larynx are

located the vocal cords, which are essential for voice production. The vocal cords can be seen in the Figure 1.2 b) [3, 4].

1.1.2 Lower Airway System

The lower respiratory tract includes the structures responsible for conducting inhaled air deeper into the lungs, where the process of gas exchange takes place. The LAS consists of the trachea, bronchi, bronchioles, and alveoli. This system plays an important role in supplying oxygen to the bloodstream and removing carbon dioxide [3, 4].

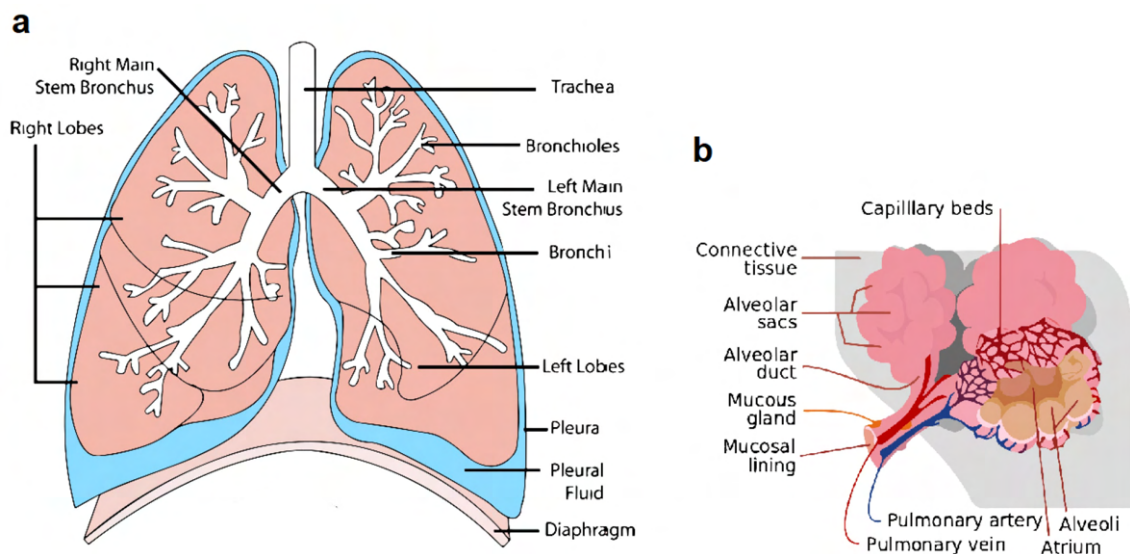


Fig. 1.3: Human lower airway system and bronchioli. a) human lower airway system, b) bronchioli [7, 8].

The Trachea

The trachea is a rigid tube composed of 16 to 20 C-shaped cartilage rings and is around 10 to 12 cm long. This structure, which is also commonly known as a windpipe, leads from the larynx (the UAS) and divides into the right and left primary bronchi. The inner lining of the trachea possesses ciliated cells and goblet cells that produce mucus, working together to filter and eliminate particles from the inhaled air [3, 4].

The Bronchi and Bronchioles

The trachea branches into two primary bronchi, leading into the left and right lungs. In the lungs the primary bronchi further splits into narrower branches - secondary (lobar) and tertiary bronchi. In the left lung are 2 lobar bronchi and in the right

lung are 3 lobar bronchi carrying air into each of the main lobes of the lung. Tertiary bronchi further divides into many very narrow bronchioles that spreads throughout the lungs and end with respiratory (terminal) bronchioles, which give rise to the formation of 2 to 11 alveolar ducts. Bronchioles are the smallest branches of the respiratory tree. Since the bronchi are an extension of the trachea, they have very similar structure to the trachea. The bronchi are reinforced with cartilage and their lining contains ciliated cells and mucus glands that continue the air filtering function on its way to the lungs. Bronchioles lack cartilage structure and are mainly composed of smooth muscle tissue [3, 4].

The Lungs

The lungs are responsible for the exchange of gas between the air and blood, therefore the lungs are vital and main organs of the lower respiratory system. The lungs are a paired cone shaped organ (right and left lobe) with spongy structure and pinkish-gray hue. Both of the lungs are located in the thoracic cage. Anatomically, the right and left lung are similar, but asymmetrical. The right lung is divided by an oblique and horizontal fissure into 3 lobes - the right upper lobe (RUL), the right middle lobe (RML), and the right lower lobe (RLL). The left lung is divided by an oblique fissure and consists of 2 lobes - the left upper lobe (LUL) and the left lower lobe (LLL) [4, 9].

As was mentioned above, left and right primary bronchi enter the appropriate lung lobes and throughout the lungs are gradually divided up to the smallest and narrowest branches of respiratory tree - bronchioles. Terminal bronchioles lead through the alveolar duct to clusters of air sacs called alveoli. Alveoli are the sacs structures responsible for gas exchange between the respiratory system and the circulatory system - the molecules of oxygen from inhaled air diffuse through the alveolar wall into the bloodstream. In the opposite direction the molecules of carbon dioxide are moved from the blood into the alveoli and then are expelled during exhalation. This gas exchange is enabled by the extensive network of capillares which surrounds elveoli. Oxygenated blood is then distributed to the whole body through network of blood vessels. The alveoli walls are lined with a thin layer of epithelial cells of 2 types. **Type I pneumocytes** facilitate efficient gas diffusion at the alveoli-capilares level. **Type II pneumocytes** secrets surfactant into the alveolar space. Surfactant helps maintain alveolar surface tension and prevents collapse during exhalation [4, 9, 10].

The lungs are surrounded by a serous membrane called the pleura, consisting of two layers. The visceral pleura (inner layer) covers the lung's outer surface. The parietal pleura (outer layer) lines the inner surface of the chest wall. The pleural

space, lying between these layers, contains a small amount of pleural fluid. Pleural fluid serves to minimize friction and facilitate smooth movement of the lungs and inflation during breathing [11].

Several muscles, including the dome-shaped diaphragm and intercostal muscles, contribute to both inspiration and expiration. These muscles play a role in generating negative pressure within the thorax during inhalation, allowing the lungs to fill as their pressure becomes lower than the atmospheric pressure. Conversely, these muscles also assist in creating positive pressure within the thorax during exhalation, aiding in the emptying of the lungs as their pressure exceeds the atmospheric pressure [9].

1.2 Image Segmentation

Image segmentation is one of the fundamental steps of image analysis. It is basically the division of the original image into meaningful and non-overlapping areas, which represent various objects of the real scene, such as soft tissues, bones and blood vessels. The output of the segmentation is an image with the same dimensions as the original image and in which the specific regions are separated. If the goal of segmentation is to separate a specific object and the background, then the output segmented image is binary. For image segmentation it is possible to use various local parameters of brightness function, or the brightness value itself can be used [12].

1.2.1 Segmentation by Intensity Homogeneity

Thresholding

Thresholding is the simplest segmentation method in terms of principle and implementation. The fundamental problem in thresholding is to determine the value of thresholds that define a unique interval of segmentation parameter values. The most common segmentation parameter tends to be the brightness value of a pixel. Histogram or quantitative methods for calculating the optimal threshold can be used to determine the threshold values. A modification of ordinary thresholding is adaptive thresholding. In the adaptive thresholding method, the threshold value is not fixed for each pixel of the whole image but is evaluated locally in a specific window. Another method that is based on setting threshold values is the double thresholding method. In this method, two threshold values are set. These thresholds define an interval of values on both sides. The pixels of the image falling with their values in the interval between the given thresholds are assigned the value 1, all other pixels are assigned the value 0, thus the binary image [12].

Splitting and Merging Regions Method

The method of splitting and merging regions is also based on segmentation according to the homogeneity of pixel intensity values. Areas that are inhomogeneous in terms of a given parameter (intensity) are recursively divided into smaller ones. Such segmentation is performed until homogeneity is achieved within the sub-areas. In the next steps, similar neighboring homogeneous regions resulting from the subdivision are then joined by [12].

Region Growing Method

The region growing method is another segmentation technique whose main parameter is the pixel intensity value. The first step is to select the initiation points of the growing process, called seeds. Then the surrounding pixels of the initiation points are checked and according to the selected criterion it is decided whether or not these surrounding pixels belong to the emerging segment. If a pixel has been added to the emergent segment, it becomes the new starting point around which the surrounding pixels are evaluated [12].

K-means Clustering Algorithm

K-means clustering is a widely used algorithm for image segmentation, leveraging unsupervised learning to group pixels into predefined number (k) of clusters based on similarities in their feature space [13].

1.2.2 Edge-Based Segmentation

The first step of edge-oriented segmentation techniques is often edge detection. This is an approach that is used to detect pixels in which there are step changes in brightness values. It is often at the locations where sharp changes in brightness occur that the boundaries between regions are found. An important step in edge detection is to set a threshold value, which is used to decide whether or not a given brightness jump will be considered an edge [12].

Hough Transform

The Hough transform is one of the edge-oriented segmentation techniques. This segmentation method is mainly used for partial image segmentation, where objects of known shapes that can be described by a mathematical equation (e.g. lines or circles) are searched for in the image [12].

Active Contour Method ("Snakes" Method)

The active contour method uses edge-oriented segmentation, and its principle is to gradually shape contours up to the edge of an object in the image. The active contour model is a directed curve that first approximately bounds the object in the image and then deforms due to so-called internal, image and external forces. The internal forces control the smoothness of the waveform, the image forces direct the contour shaping towards the edge of the object, and the external forces are the result of the initial location of the contour [12].

Level-sets Method

The level-sets segmentation methods use a similar approach to the active contour method. The curve is represented by a so-called zero level (zero level-set), which is a cut in the x,y plane by some multidimensional function. This function is called level-set function and assigns to each point in the x,y plane its height above the zero level. The surface of the function is gradually adapted with respect to the specified curvature metrics and image gradients. The basic difference of the level-set method versus the classical active contours is that we do not change the shape of the curve directly, but through the level-set function [12].

Watershed Method

The watershed method is in between edge-based and region-based segmentation. This method is not applied to the original brightness image, but to the parametric image. The parametric image is derived from the original brightness image most often using local difference operators, i.e. those that approximate the first derivatives by differences. This method is based on raising an imaginary water level and gradually flooding the terrain (image) with water. The water level rises from the local minima of the terrain and forms a so-called basin. At the moment when the water from the two basins should merge, a dam (a border between adjacent basins) is inserted between them to break the connection. The rising of the level is stopped when the maximum ground level is reached, when the level has nowhere further to rise. In this way, the entire surface has been flooded and only the resulting dykes remain. The result is several basins separated by dykes, showing the division of the areas of the original image. Possible disadvantage of this method is that it tends to over-segmentation of the image, so further post-processing approaches are required [12, 14].

1.2.3 Deep Learning-based Segmentation Methods

In recent years, significant progress has been made in achieving more accurate segmentation results thanks to the use of machine learning methods. Machine learning is one branch of artificial intelligence, where the basic idea is to design an algorithm that allows a computer to learn how to best solve a given problem. The result of the proposed machine learning algorithm is a mathematical function $y = f(x)$ that computes the desired output y from the input information stored in the vector x . The two most commonly solved problems using machine learning algorithms are classification and regression. In the case of classification tasks, the object represented by the input feature vector x is assigned to one of the discrete classification classes [15].

Some of the principles used by machine learning-based segmentation methods include deep convolutional neural networks (CNNs) or support vector machines (SVMs).

Support Vector Machines (SVM)

Support vector machines is a frequently used method for linear classification. This method is based on the partitioning of objects in the feature space by a hyperplane. The assumption of the hyperplane division is that it tries to maximize the distance between the hyperplane and the closest objects. The optimal result is achieved if the largest possible width of the so-called discriminative hyperplane that separates the given classification classes is chosen. The objects that are closest to the separating hyperplane are called support vectors [15].

Convolutional Neural Networks (CNN)

A specific type of neural networks are convolutional neural networks (CNN). Convolutional neural networks belong to the group of deep learning algorithms and were created mainly for processing data in the form of matrices, an example can be 2D images with three color channels [16, 17, 18].

These networks use the mathematical operation called convolution in at least one of their layers, therefore a given layer and the whole network is called **convolutional**. CNN can take in an input image, assign importance (learnable **weights** and **biases**) to various objects in the image, and be able to differentiate one from the other. CNNs have ability to automatically learn hierarchical representations of features from the input data. The pre-processing required in a CNN is much lower as compared to other classification algorithms. The basic idea of CNN is to share the weights of feature mapping in different positions of the previous layer network,

and to reduce the number of parameters by using spatial relative relationships to improve training performance [16, 17, 18].

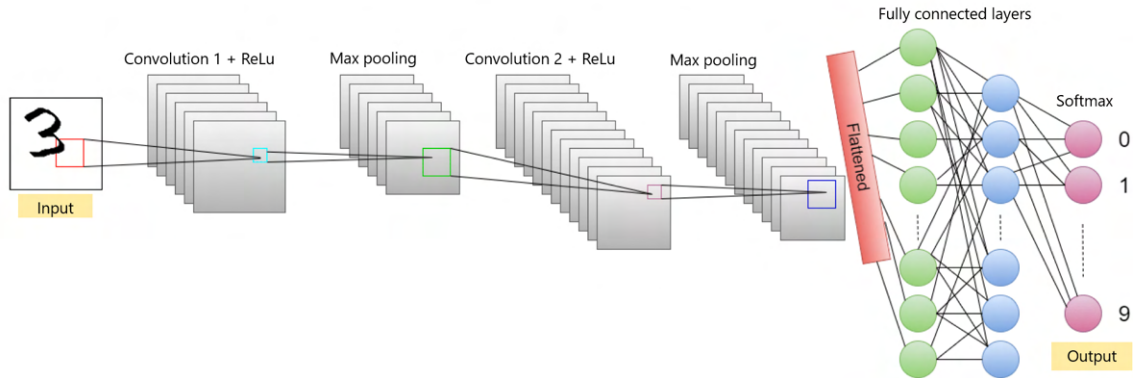


Fig. 1.4: CNN architecture scheme [19].

The core building block of a CNN is the **convolutional layer** (the first layer of a convolutional network), which is where the majority of computation occurs. The convolutional layer applies a filter (kernels) to the input data to produce a feature map that highlights the presence of a given feature in the image. In a convolutional layer, multiple filters are applied over the image to extract different features from large-scale data. CNNs have excellent feature extraction capabilities and good feature expression capabilities. The layers are hierarchically arranged in such a way so that they detect simpler patterns first (lines, curves, edges, etc.) and more complex patterns (objects, etc.) further along. Then follows the **pooling layers** (downsampling), which are used to reduce the spatial dimensions of the feature maps while retaining important information. Max pooling, for example, selects the maximum value from a group of neighboring pixels, reducing the size of the feature maps, and making the network more computationally efficient. After several convolutional and pooling layers, the final feature maps are flattened and connected to one or more **fully connected layers** (the final layer). These layers are responsible for the task of classification based on the features extracted through the previous layers and their different filters. While convolutional and pooling layers tend to use ReLu activation functions (introduce non-linearity to the network and this non-linearity allows the CNN to learn complex relationships and representations in the data), fully connected layers usually leverage a softmax activation function to classify inputs appropriately, producing a probability from 0 to 1 [16, 17, 18, 21].

Compared to other machine learning methods, convolutional neural networks achieve very high success rates in practical applications. This type of neural network belongs to the group of so-called supervised learning, where it is necessary to know the desired classification outputs of the training objects to train the network [17].

U-Net

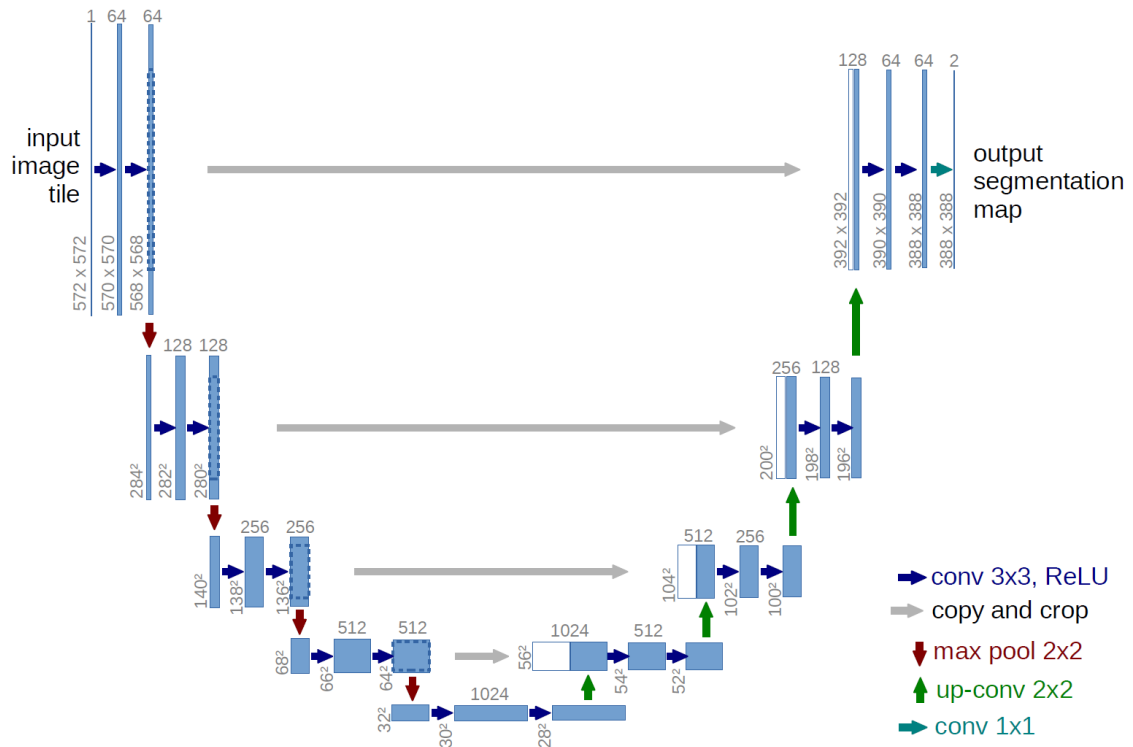


Fig. 1.5: U-net architecture. Blue boxes correspond to a multi-channel feature map. The number of channels is denoted on top of the box. The x-y-size is provided at the lower left edge of the box. White boxes represent copied feature maps. The arrows denote the different operations explained in the legend [20].

U-Net is a special CNN architecture and was designed for biomedical images analysis, which was widely used in medical image segmentation (semantic segmentation). U-Net network is composed of **U-channel** and **skip-connection**. The U-channel consists of the encoder-decoder structure (that ensures feature extraction). The **encoder** forms the first half of the U-Net, also called descending part, and has four submodules, each of which contains two convolutional layers. After each submodule, there is a max pool, to realize down sampling. This process progressively reduces the spatial dimensions while increasing the number of feature channels. At the bottom of the U-Net architecture is a **bottleneck** or bridge, which typically consists of additional convolutional layers. This bottleneck captures and retains high-level context information. The second half of the U-Net is a **decoder** and contains four submodules. The spatial resolution of the feature maps is increased successively by up-sampling. Each up-sampling step consists of an up-convolutional layer, concatenation with the corresponding feature map from the encoding path (skip connection) and two convolutional layers with ReLU activations. One of the key innovations of

U-Net is the use of **skip connections** ("copy and crop"), which directly connect the corresponding feature maps from the encoding (contracting) path to the decoding (expansive) path. These connections enable the network to combine low-level and high-level features, helping to preserve fine-grained details during segmentation. The final layer of this architecture typically consists of a 1x1 convolutional layer followed by a softmax activation function, producing a probability map for each pixel in the input image. This map represents the likelihood of each pixel belonging to a certain class in the segmentation task [20, 21].

U-Net is well-suited for medical image segmentation primarily because its architecture allows simultaneously combine low-level and high-level information. The incorporation of low-level information contributes to improve accuracy, while the high-level information facilitates the extraction of complex features [20, 21].

1.2.4 Metrics for Quantitative Assessment of Segmented 3D Models

Metrics for quantitative assessment of segmented models are essential for evaluating the quality of segmentation. For assessment of segmented models it is necessary to have ground truth segmented model, which can be obtained e.g. by manual segmentation done by experienced human expert (radiologist,physician) [22].

Dice Similarity Coefficient

The Dice similarity coefficient (DSC), also called the overlap index or F1-score, is the most used metric in evaluating medical image segmentation. It quantifies the spatial overlap between two sets of voxels - segmented binary volume and ground truth binary volume (reference volume). The coefficient ranges from 0 to 1, where 0 indicates no overlap between the sets (complete dissimilarity), and 1 indicates perfect overlap (complete similarity). Higher Dice coefficient implies a better similarity between the two sets.

$$\text{Dice} = \frac{2 \times |V_{GT} \cap V_S|}{|V_{GT}| + |V_S|} \quad (1.1)$$

where V_{GT} is the ground truth volume, and V_S is the resulting segmented volume [22].

Hausdorff Distance

Since the Hausdorff distance is a surface distance metric, it quantifies the difference between the surfaces of the ground truth volume and predicted segmentation. Haus-

dorff distance quantifies the maximum distance between a point in the predicted segmentation and the nearest point in the ground truth segmentation. It describes the maximum dissimilarity between the predicted segmentation and ground truth segmentation. The Hausdorff distance is generally sensitive to outliers. Because noise and outliers are common in medical image segmentation, it is not recommended to use the Hausdorff distance directly [22].

Jaccard Index (Intersection over Union = IoU)

The Jaccard index measures the similarity between two sets of voxels and is often used to evaluate the overlap between the segmented and reference (ground truth) volumes. Both, Dice coefficient and Jaccard index metrics, measure the same aspects and provide the same system ranking. Therefore, it does not provide additional information to select both of them together as validation metrics [22].

Average Symmetric Surface Distance (ASSD)

The Average symmetric surface distance is boundary-based metric used to quantify the accuracy of segmentation boundaries. The ASSD provides a symmetric evaluation of the distances between the surfaces of predicted and ground truth segmentations and therefore can help to detect shape differences between the reference and the segmented object [23].

The ASSD determines the average difference between the surface of the segmented object and the reference in 3D and is defined as the average of all the distances from points on the boundary of segmented region to the boundary of the ground truth, and vice versa. A value of 0 refers to a perfect segmentation (distance of 0 to the reference boundary), while there exists no fixed upper bound [23].

1.3 Image Annotation

Image annotation involves assigning labels to images, where a human operator assesses a set of images, identifies relevant objects in each image and annotates the image by indicating details such as the shape and label of each relevant object. These annotations are often used as a training dataset for supervised artificial intelligence (AI) models, particularly in computer vision models. The model utilizes human annotations as its ground truth to learn to autonomously detect objects or label images. This process is pivotal for training models in tasks like object recognition, image classification and image segmentation [24, 25, 26, 27].

Image annotations can be executed through either manual processes or by employing automated annotation tools. Automated annotation tools are pre-trained

algorithms offering accurate annotation results and are particularly valuable for complex annotation tasks like creating segment masks, which are very time-intensive. These tools can also complement manual annotation by providing a starting point for further refinement [24, 25, 26, 27].

The quantity of labels assigned to an image varies based on the project's type and scope. Some instances require a single label to represent the entire image, while others involve annotating specific objects, segmenting images into relevant regions, or identifying landmarks as focal points of interest [24, 25, 26, 27].

1.3.1 Types of Image Annotation

Image annotation is the practice of assigning labels to enables AI models recognize and detect specific aspects within a visual representation. Different types of image annotation aims to represent different aspects of an image [26].

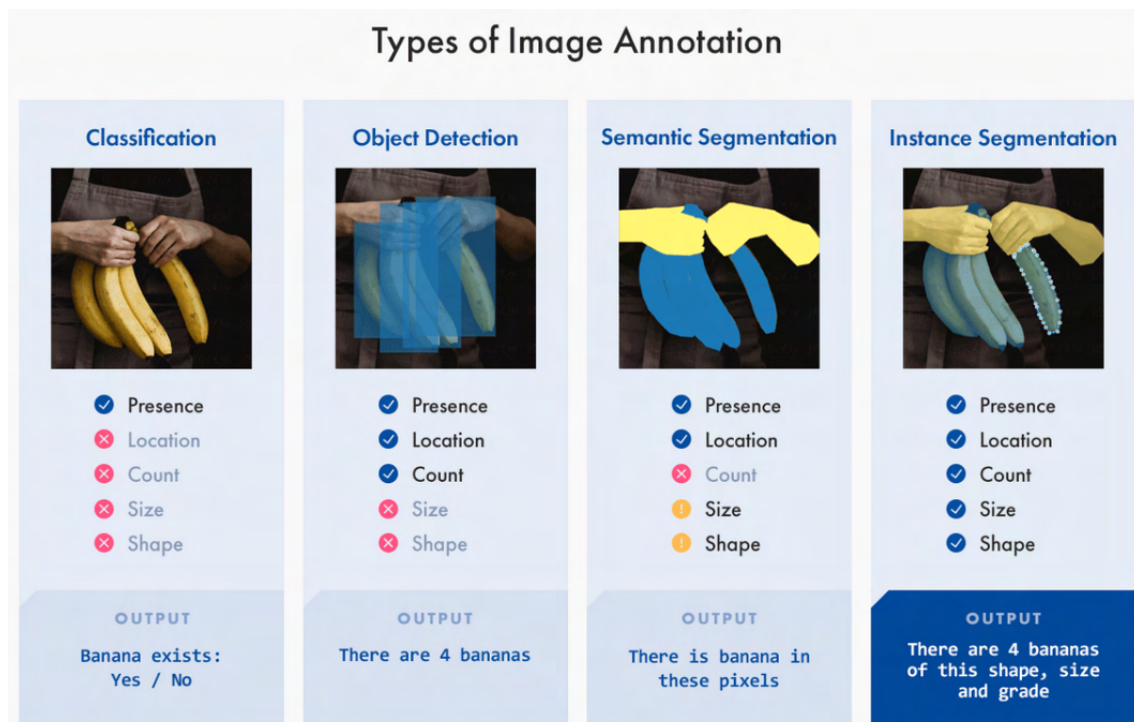


Fig. 1.6: Types of image annotation [26].

Image Classification

Image classification is a form of image annotation that aims to understand an image as a whole by assigning it a label. It is the process of identifying and categorizing the class to which the image belongs. Image classification generally applies to images in which a single object is present. It is usually used to train a model to recognize an

object in an unlabeled image that looks like an object in other labeled images that were used to train the model [26].

Object Recognition/Detection

In contrast to image classification, which assigns a label to an entire image, object detection involves labeling various objects within an image. Object detection specifically identifies objects of interest, assigns corresponding labels, and determines their location and quantity. Techniques compatible with object recognition (detection), such as bounding boxes or polygons, allow the labeling of distinct objects within a single image [24, 26].

Image Segmentation

This method is based on dividing an image into multiple segments and assigning a specific label to each segment - essentially performing pixel-level classification and labeling. Segmentation is commonly applied for complex tasks that require enhanced precision in input categorization, particularly in tracing objects and margins within images. Image segmentation facilitates the identification of boundaries and objects in an image. The outputs of image segmentation annotations are presented as segment masks — binary masks of the same shape as the image. In these masks, segments corresponding to object regions are marked with the respective class ID, while the remaining regions are labeled as zero [24, 26].

Here the three classes of image segmentation will be described:

- **Semantic segmentation** represents a specific type of image segmentation in which the algorithm divides the image into pixel regions based on distinct categories. It identifies and labels similar objects under the same classification, outlining boundaries between them. Semantic segmentation is employed when the aim is to comprehend the presence and location of objects. This method involves dividing the image into clusters and assigning a label to each cluster, ensuring that every pixel is associated with a class. For instance, in semantic segmentation, an algorithm might group together a group of people under a category "person", generating a single mask for each category. As this segmentation task does not distinguish between different instances or objects within the same category, it is commonly referred to as the most straightforward segmentation method [26, 27].
- **Instance segmentation** refers to a segmentation approach focused on separating and segmenting individual object instances from the image. Unlike isolating categories from the image, instance segmentation algorithms aim to

identify and separate similar objects within groups. This technique facilitates the identification and labeling of each distinct object in an image. The instance segmentation process involves tracking and quantifying the presence, location, count, size, and shape of objects within the image [26, 27].

- **Panoptic segmentation** is an annotation method, where instance segmentation and semantic segmentation meet - leveraging semantic segmentation to label background data and employing instance segmentation to categorize objects within the image. This technique involves classifying all pixels in the image (semantic segmentation) and determining the instances to which these pixels belong (instance segmentation). By seamlessly blending semantic and instance segmentation, panoptic segmentation delivers labeled data for both background (semantic) and objects (instance). Panoptic segmentation tackles the dual challenges of recognizing object instances and comprehending the overall scene context. It unifies the advantages of both segmentation methods, providing a comprehensive understanding of the visual content in images [26, 27].

Semantic Segmentation vs. Instance Segmentation vs. Panoptic Segmentation

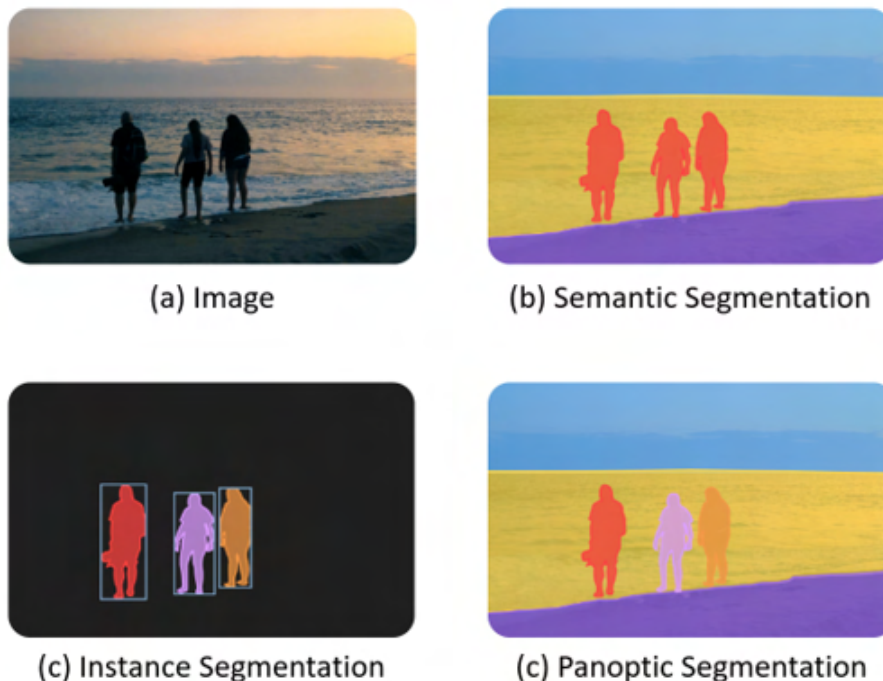


Fig. 1.7: Types of image segmentation [27].

1.3.2 Image Annotation Techniques

Various tasks require different forms of data annotation to enable direct utilization of the processed data in training. The choice of annotation technique usually depends on the specific requirements of the task and the complexity of the objects to be annotated. For straightforward tasks like classification, simple tags are sufficient for annotation. Conversely, complex tasks such as segmentation demand the data to have pixel map annotations and object detection requires bounding box annotations. All these annotation techniques can be performed manually by human annotators or automated using specialized software tools [27].

Bounding Boxes

Bounding boxes are used to draw rectangles around the target objects, especially applicable for relatively symmetrical objects, such as vehicles, pedestrians, and road signs. This method is often used when the shape of the object is of less interest. Bounding boxes can be either two-dimensional (2D) or three-dimensional (3D). A 3D bounding box is also called a cuboid. These annotations are typically essential for object detection algorithms where the box denotes the object boundaries. However, they are generally less precise compared to segmentation or polygonal annotations [24, 26, 27].

Polylines

Polylines, along with bounding boxes, are among the most straightforward image annotation methods to grasp. They are employed for annotating line segments like wires, lanes, and sidewalks. Utilizing small lines connected at vertices, polylines excel at delineating shapes of structures such as pipelines, rail tracks, and streets. These annotations manifest as a set of lines drawn across the input image [24, 27].

Polygons

Polygons are used to annotate the edges of objects that possess an often-asymmetrical shape, deviating from symmetry or rectangularity. Annotating with polygons involves a very specific approach, requiring the selection of a series of points and manual drawing lines along the object's edges. Compared to bounding boxes, polygon masks typically offer higher precision due to the greater number of corners they can encompass. This precision results from the flexibility of polygons, as they are not restricted to the four vertices of bounding boxes. Moreover, polygonal masks are space-efficient, easily vectorizable and provide a balance between space utilization and accuracy. These masks are used to train object detection and semantic

segmentation algorithms. Polygon masks are commonly employed for annotating medical imaging data [24, 27].

Key Points (Landmarks)

Key points play a crucial role in annotating highly specific features on the target object, such as facial characteristics, body parts, and postures. When applied to a human face, key points enable the precise identification of the eyes, nose, and mouth. Particularly, this technique finds frequent application in security purposes, facilitating rapid facial recognition by computer vision models. Key point annotation is extensively employed in various applications, including emotion detection, facial recognition, biometric boarding, gesture recognition, and determining the position and orientation of the human body. This type of annotation involves placing markers on coordinates in the image that hold particular significance, providing a precise location for a specific feature or object within the image [24, 27].

In the medical field, the significant application of medical image annotation lies in diagnosing diseases like cancer, brain tumors, and other nerve-related disorders. For instance, through precise pixel annotation techniques applied to images of benign and malignant tumors, medical doctors can make faster and more accurate diagnoses. In medical image annotation, annotators highlight the areas requiring special attention, employing methods such as bounding boxes, polygons, or other techniques relevant to the specific use case. The quantity of available data enables healthcare professionals to provide more precise information to patients as predictive algorithms and image annotation techniques are now offering better predictive models [24].

1.4 Computational Fluid Dynamics

Computational fluid dynamics (CFD) is a tool used to simulate the movement and behavior of fluids (liquids and gases), emerging as an efficient alternative for understanding airflow in the human upper airway (HUA). It aids in preparing patients for surgery, planning surgical procedures, and predicting surgical outcomes. In recent years, CFD has been widely employed to analyze airflow in both healthy and diseased human conducting airways. Advancements in medical imaging techniques enable the reconstruction of unique and realistic respiratory tract geometries from scanned images, facilitating their conversion into geometric models for CFD simulation. The rapid development of new computational and numerical methods, coupled with powerful hardware, has reduced computation time, allowing researchers to study critical airflow in the upper airway before surgery. This makes CFD a vital

and useful tool for analyzing and predicting various flow properties in the human upper airways by computationally solving flow equations using numerical methods and algorithmic processes [28, 29].

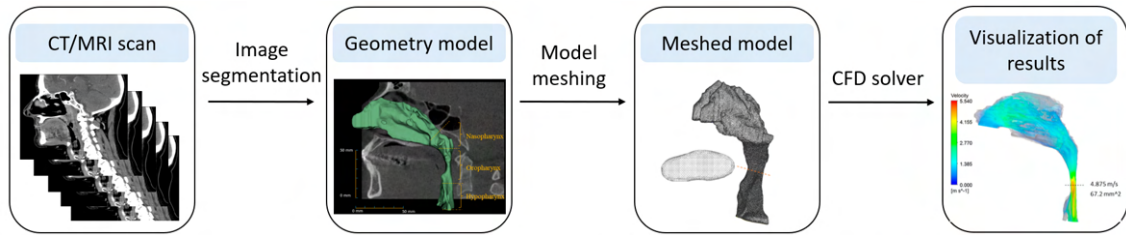


Fig. 1.8: Computational fluid dynamics scheme [30].

In the first step of the CFD analysis of the upper airways, an **anatomical geometric model** is created based on MRI or CT scans processed by image processing software. **Image segmentation** is a key step in this process. After creating the three-dimensional fluid domain of interest, **model meshing** is carried out to further divide (spatially discretize) the 3D airflow domain into a grid formed by a number of smaller elements. Model meshing is crucial as it enables computations of **Navier-Stokes equations** within smaller known structures (elements), enhancing convergence rate, accuracy of simulation results, and computation time. Determining the optimal number of elements for a domain is an important step in mesh generation, as it reduces computational time and ensures reliable and accurate CFD results. The rapid development of commercial software facilitates mesh generation through various popular tools, such as ANSYS Workbench [28, 29].

The next step is fluid dynamics simulation, where numerical methods are applied to discretize the governing equations of fluid dynamics (Navier-Stokes equations) over the mesh. This step models airflow within the airway geometry model. Choosing the right flow model is crucial for accurately simulating average flow characteristics that match real-life conditions. There are six turbulence models in CFD, which can be grouped into three main models: Reynolds-averaged Navier-Stokes (RANS), large-eddy simulation (LES), and direct numerical simulation (DNS). Selecting an appropriate **CFD solver** is also important, as it computes discretized equations and iteratively solves for pressure, velocity, and other flow parameters until convergence is reached [28].

In the analysis of the human upper airways using CFD simulation, **post-processing** is essential for visualizing and examining flow properties such as airflow velocity, pressure, turbulence, and wall shear stress. Post-processing tools include **numerical reporting**, which calculate quantitative results, and **visualization**, which display simulation results in different types of plots. These plots can show contour lines,

vectors, streamlines, and surfaces in both 2D and 3D. Visualization tools can also create animations of flow properties [28].

2 Material and Methods

This chapter describes the practical part of the thesis. The general objective of the thesis was to implement segmentation or annotation algorithms on CT scans with the purpose of generating a three-dimensional model of the human upper airways. The schematic representation of the general workflow is presented in Figure 2.1. A variety of segmentation and annotation methods, which will be further described in the following chapters, were employed, and the resulting 3D models of HUA were subjected to comparative analysis. Furthermore, a CFD simulation was conducted on one of the models to evaluate the quality of the generated 3D model.

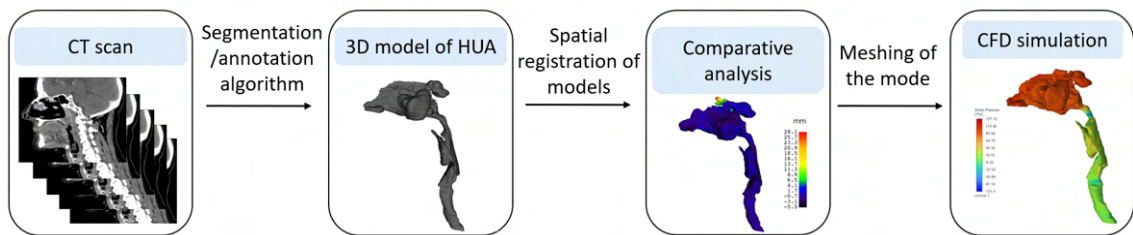


Fig. 2.1: Scheme of general workflow.

2.1 Dataset

For this thesis, a dataset comprising 6 CT scans was available. The selection of CT scans was designed to represent three distinct groups based on the age and sex of the patients. The first group was representative of „children and young adolescents“ age group (under 15 years old) and comprised a 7-year-old male and a 12-year-old female. Subsequently, the second and third group represented the „working-age population“ age group (15–64 years). The second group included a 15-year-old male and a 17-year-old female, while the third group consisted of a 59-year-old male and a 63-year-old female.

Given the considerable variability in the geometry of upper airways within the human population, this diversity of available CT scans might be useful for capturing a spectrum of anatomical geometries, that differ particularly across different age groups and sexes.

All CT scans were stored in the Digital Imaging and Communications in Medicine (DICOM) format, which is the standard and widely used format for medical images, such as X-rays, CT and MRI scans, as well as ultrasound images. The DICOM format, in addition to the image data, contains a header, where metadata are stored. The metadata includes information about the patient, imaging system, acquisition

parameters, and image reconstruction parameters. A selection of key parameters for our CT scans is listed in the Table 2.1.

Patient	Image size [pixels]	Voxel size [mm]	Plane view	Pixel value [HU]
X1_63YF	512 x 512 x 424	1.0 x 1.0 x 1.0	axial	- 1024 to 1578
X2_59YM	512 x 651 x 70	0.42 x 0.42 x 2.0	sagittal	- 1024 to 1532
X3_15YM	512 x 512 x 35	0.39 x 0.39 x 3.07	sagittal	-1024 to 1601
X4_17YF	512 x 512 x 40	0.39 x 0.39 x 2.63	sagittal	-1024 to 1554
X5_12YF	512 x 512 x 70	0.49 x 0.49 x 2.02	sagittal	-1024 to 1130
X6_7YM	512 x 512 x 39	0.31 x 0.31 x 2.1	sagittal	-1024 to 1615

Table 2.1: Table with selected metadata for 6 CT scans.

2.2 Annotation and Segmentation of the HUA

Annotation and segmentation of anatomical structures in CT images play a vital role in helping medical professionals identify and assess pathological changes. For upper airways, such changes may include tumors, narrowing, or obstructions. Manual annotation or segmentation of CT scans can be exceedingly time-consuming, especially for complex anatomical structures. Consequently, efforts are underway to develop and utilize automated methods and algorithms, which not only provide more reliable results but also save time and effort for experts.

During CT image annotation, upper airway regions were marked and assigned labels on a slice-by-slice basis. The annotated CT volumes, comprising labeled slices, were exported in the NIfTI (Neuroimaging Informatics Technology Initiative) file format. As part of the export process, the labeled slices were automatically converted to binary format, with labeled structures considered as foreground and remaining unlabeled parts as background. Subsequently, 3D models of the upper airways were reconstructed from the resulting binary volumes (NIfTI files).

In the CT image segmentation process, binarization of the image occurs directly. The upper airway area is transformed to foreground, with binary image values of 1, while surrounding tissues are transformed to background, with binary image values of 0. The binary segmentation results were exported in NIfTI file format, which was then utilized for reconstructing the 3D upper airway model.

The process of reconstructing the 3D upper airway model from the binary volume was common for both annotation and segmentation algorithms. The NIfTI file was imported into the 3D Slicer software. Given that the binary volume comprises the object (foreground = 1) and background (0), a simple thresholding method

with a threshold value of 1 was applied to extract only the object of interest. The resulting 3D upper airways model was exported as a triangular surface model in STL (stereolithography) file format.

2.3 Methods for HUA Annotation

In this section, the methods used for HUA annotation will first be briefly introduced and then the whole procedure of using the method will be described in detail.

2.3.1 Medical Volume Annotator

Medical Volume Annotator (MVA) software provides the option for either on-site (local) installation or a cloud-hosted version. Opting for local installation on a user's computer grants complete control over data and annotations, offering MVA a distinct advantage over other software options. The MVA software doesn't necessitate advanced hardware and facilitates fast viewing, editing, and annotating of various 2D and 3D image types, including whole-body CTs and diverse MRI imaging sequences. MVA allows the upload of existing annotation projects for editing or expert feedback. For annotating 2D and 3D images, the MVA offers a wide array of tools, including paint tool, superpixel-based tool or thresholding-based tool. Users can assign single or multiple labels per voxel, and the software enables label propagation from one slice to the next while automatically deforming annotations to align with the new image. A unique feature is called negative labels, specifying the absence of a label in a slice or volume. MVA provides precise management of users/teams, along with their roles and permissions. It enables the regulation of visibility, annotation, and case review capabilities for different individuals or teams. At each stage, distinct users can be assigned with specific settings, dictating their permissible actions. Medical image data in MVA can be imported in DICOM series or NifTI volumes, as well as common 2D image formats. The pixel/voxel annotations generated are exported in NifTI file format and JSON file. MVA stands out for its notable advantage in being adaptable to a variety of annotation project requirements. The extensive support from software developers ensures that MVA can be tailored to individual workflows, accommodating different data formats or reporting needs [31].

Use of the MVA

In this work, the on-site installed version was utilized, mainly to ensure the security of the CT data.

A notable feature offered by the MVA software is **superpixels** tool. Superpixels partition the entire image into a dense mesh of connected polygons (cells), enabling the delineation of sharp boundaries between different anatomical structures based on different pixel intensities. This feature helps annotators to easily mark areas of interest without inadvertently painting outside the desired region. The density of the polygonal superpixel mesh can be adjusted by the user, with a finer mesh (high number of small elements) capturing more details and small anatomical structures, see Figure 2.2.

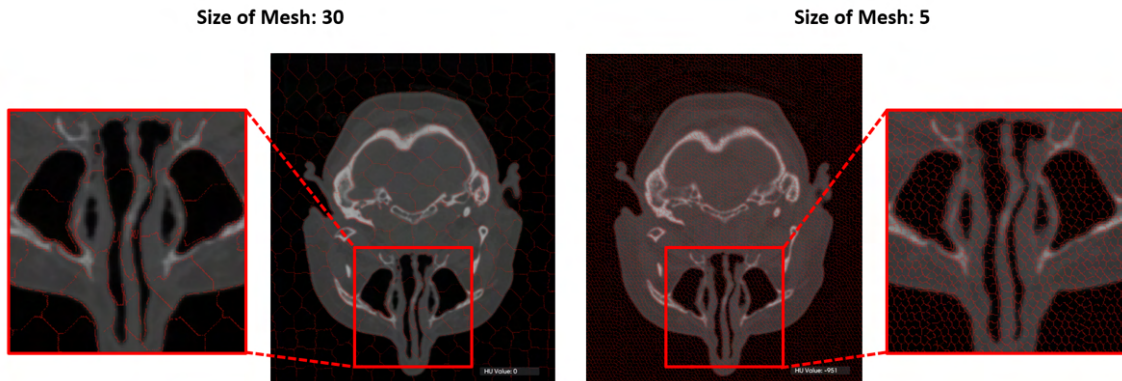


Fig. 2.2: The MVA polygonal superpixel mesh with different size of elements. The image on the left-hand side (size of mesh: 30) illustrates a coarse grid with a smaller number of larger cells, whereas the image on the right-hand side (size of mesh: 5) depicts a finer mesh with a higher number of smaller elements.

The superpixels tool can be employed in combination with the **paint tool** or the **thresholding tool**. The paint tool marks individual selected elements of the superpixel mesh. The thresholding tool operates on the principle of region growing method. Once the seed point is placed, elements of the superpixel mesh are marked based on a user-defined threshold value.

Following the labeling of the anatomical structure of interest, the MVA offers a useful tool called **propagation of the label**, which propagates the labeled area to the following slice. For labels created by the paint tool, propagated labeled area is automatically adjusted based on the overlap of superpixel mesh elements between consecutive slices. For propagation of labels created by the thresholding tool, a movable central point with a specified threshold value is defined inside the anatomical structure of interest, and the labeled area is propagated to the following slice based on this threshold value.

Labels for anatomical parts of the upper airways, including the trachea, larynx, pharynx, and nasal cavity, were assigned directly within the MVA software during

the annotation process. The final annotated CT volumes were exported in the NIfTI file format.

2.3.2 V7

V7 is an automated annotation tool designed to simplify various annotation tasks, including image classification, instance, panoptic, or semantic segmentation, object detection, and volumetric segmentation [32]. V7 offers both a full commercial version and a free trial version, which is limited by the number of images that can be uploaded. Alongside a diverse set of tools such as polygons, brushes, or bounding boxes, V7 provides volumetric annotation (3D labeling) and a valuable auto-annotate feature. This automated annotation feature rapidly creates pixel-perfect polygon masks, facilitating the automatic segmentation of complex shapes within a selected area.

There are no special hardware requirements for using V7, except for a stable internet connection. V7 finds applications in a wide range of medical use cases, spanning CT and MRI scans analysis, X-rays, mammography, dental image analysis, to ultrasound image and video analysis. It supports common 2D image formats like JPG, PNG, video format MP4, and medical image volume formats DICOM and NIfTI. V7 natively supports DICOM in 16-bit, preserving original image quality.

V7 allows customizable data workflows¹ and real-time collaboration among annotators. This enables users to annotate images collaboratively, add multiple labels to a single image simultaneously, and communicate in real-time to ensure label accuracy. The tool also offers advanced image manipulation features, including windowing, orientation markers, reference lines, histograms, color maps, and contrast control.

For exporting annotations, V7 recommends Darwin JSON 2.0 format or NIfTI format. In Darwin JSON 2.0, annotations from each plane are saved in separate slots, while in NIfTI, exported annotations can be viewed in external 3D NIfTI viewers. Notably, V7 supports custom labeling pipelines, combining human labeling with machine learning model input to accelerate the annotation process. Users can contact software developers to create a customized segmentation model for their specific use case. V7 also provides professional on-demand labelers [32].

¹Customizable data workflow is typically focused on the number of review stages. Project workflows enable the explicit definition of a sequence of annotation and review stages within the project. Once an annotated data has successfully passed through all stages of a workflow, it will reach the export stage. A typical workflow involves a single annotation stage followed by two review stages, where distinct groups of reviewers validate the annotations.

Use of the V7

For this work, the free trial version of V7 was utilized. Among the range of annotation tools available in V7, only a select few were employed for our specific task, which will be described in detail below.

The **auto-annotate tool** automatically recognizes, marks and labels anatomical structure of interest within a specified bounding box. Initially, a rectangular bounding box was created to define the area of interest containing the anatomical structure. Subsequently, the auto-annotate tool created a polygonal mask that ideally delineates the anatomical structure of interest and assigned a corresponding label. If the created polygonal mask is inaccurate, the auto-annotation tool offers a one-click correction tool to adjust and improve the annotation mask by placing correction points. Green correction points were placed in areas where the desired label was missing, while red correction points were placed to exclude incorrectly labeled parts. If the corrected annotation mask was still not accurate enough, the mask boundary points were manually shifted.

The next tool utilized was the **polygon tool**, which was employed for manually creating polygon-shaped masks by placing points along the border of the anatomical structure of interest. This tool was primarily used for complex-shaped anatomical structures where the auto-annotate tool failed and produced inadequate annotation masks.

Annotation of CT scans was conducted in a slice-by-slice approach and final annotated CT volumes were exported in NIfTI file format.

2.4 Methods for HUA Segmentation

In this section, the methods used for HUA segmentation will first be briefly introduced and then the whole procedure of using the method will be described in detail.

2.4.1 3D Slicer

The 3D Slicer software represents an open-source, versatile platform for the analysis and visualization of medical images. As a comprehensive desktop solution, 3D Slicer serves a diverse spectrum of medical image processing applications, involving visualization, processing, segmentation, and registration of medical images.

A notable advantage of 3D Slicer lies in its huge community of experienced users and developers, collaboratively engaged in enhancing existing tools and developing novel modules and extensions. 3D Slicer benefits from the collective experience of

its global user community and experts in the field and hosts a robust online support forum that addresses numerous tasks and challenges encountered in medical image analysis. This platform serves as a valuable resource for users seeking guidance and solutions to complex problems.

Distinguished by its user-friendly interface, extensive feature set and robust capabilities, 3D Slicer is a valuable tool in medical research and clinical practice. It empowers users to analyze, segment and visualize complex medical image datasets with accuracy and efficiency [33].

Use of the 3D Slicer

After the installation of the 3D Slicer software, the CT data were imported as a *volume*.

For the segmentation of the upper airways, the **threshold tool** was selected from the *segment editor module*. To initiate a new segmentation, it was required to specify the *source volume*, which comprised our uploaded CT scan itself. The threshold tool delineates and fills areas based on the intensity range of the source volume and the set threshold values. Given the distinct contrast between the airways (filled with air, CT values approximately around -1000 Hounsfield Units (HU) [34]) and surrounding soft tissues (with significantly higher CT values ranging between -100 HU and 100 HU [34]), the threshold values were established and fine-tuned through slice-by-slice visual assessment of the segmentation masks generated and color displayed in axial, frontal, and sagittal views (refer to Figure 2.3).

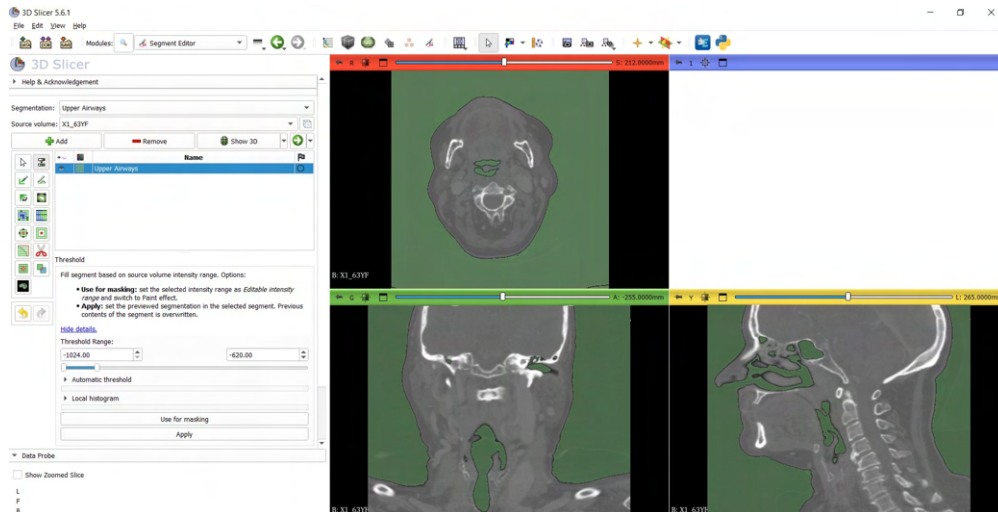


Fig. 2.3: The 3D Slicer user-interface for the segment editor module depicts the chosen threshold tool. Areas to be segmented are marked in green color based on the set threshold range. For example, for the CT scan of patient X1_63YF, the threshold range was set from -1024 HU to -620 HU.

The **threshold ranges** varied for different CT scans due to differences in the intensity ranges of source volumes, as well as fine-tunings made to create a user-subjective best-fitting upper airways segmentation mask. After applying the threshold tool, the segmentation mask and 3D model were generated. However, in addition to the desired upper airway anatomical structures, they included all parts containing air, such as ear canals, lungs, and mostly the background (refer to Figure 2.4).

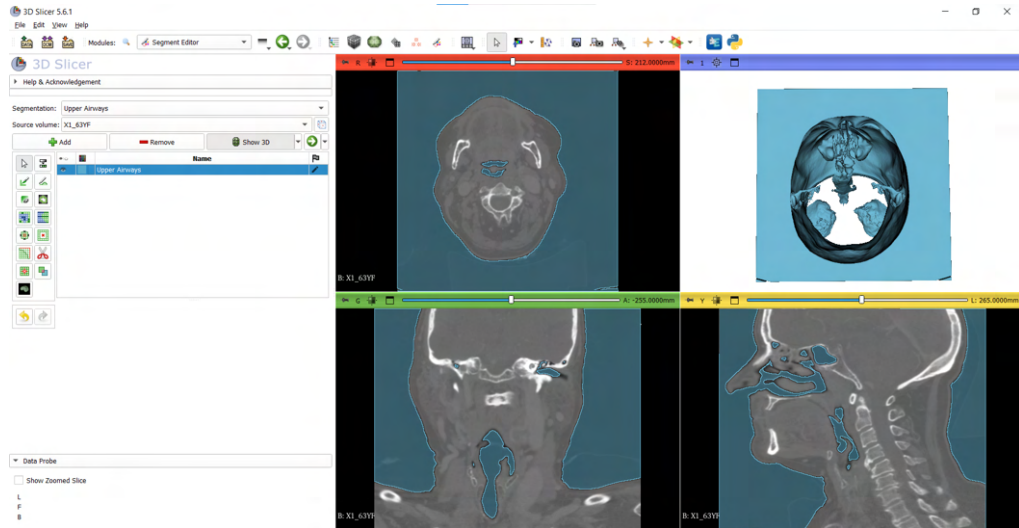


Fig. 2.4: Segmentation results after applying the threshold tool in 3D Slicer. The created segmentation masks are displayed in blue color in the three plane views, with the 3D model shown in the upper right-hand corner. In addition to the airways, the segmentation masks also encompass surrounding air-filled regions.

The **scissor tool** was utilized to remove unwanted parts from the created segmentation masks and model, both in the 3D view and in the 2D planes. In the 3D view, rough deletion of disconnected structures and marked areas distant from the upper airways model was performed, while in the 2D slice-by-slice approach, fine erasing of unwanted parts close to the airways was carried out. Segmentation masks and the model of the upper airways after removing unwanted parts can be observed in Figure 2.5.

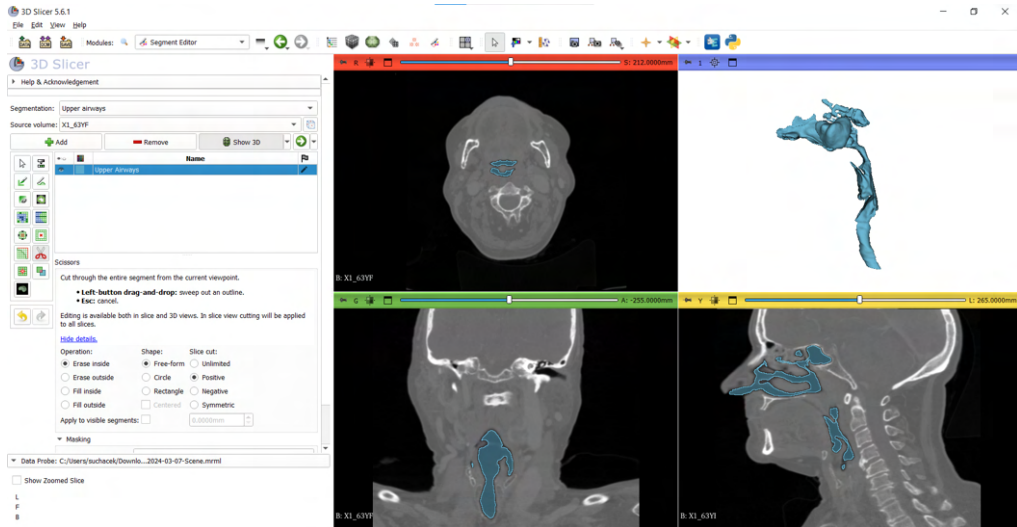


Fig. 2.5: The final adjusted segmentation results in 3D Slicer. Following manual removal of unwanted parts, the resulting segmentation masks and 3D model of the upper airways are depicted in blue color.

The resulting segmented upper airways models were exported as a surface model in STL format.

2.4.2 Synopsys Simpleware Software

Simpleware Software from Synopsys is a commercial software that provides advanced 3D image processing capabilities, facilitating tasks like 3D image data visualization, segmentation, and model generation from scans.

The Simpleware Software includes a range of anatomy-specific auto segmentation modules tailored to different anatomical areas, such as orthopedics and craniomaxillofacial (CMF) applications, or cardiology applications. For instance, the **auto segmenter for orthopedics** is specifically designed for processing orthopedic data covering ankle CT, hip CT, knee MRI/CT, and shoulder CT scans. Similarly, the **auto segmenter for CMF CT** module automates segmentation for areas such as skull, mandible, teeth, cervical spine, airways, ear canal, cranial cavity, eyes and optic nerves. Additionally, there's a special **auto segmenter for cardiology** module designed for segmentation of heart data covering blood pool and selected muscle tissues. These auto segmentation tools are powered by AI technology employing machine learning algorithms. While detailed information about the specific ML algorithms used is limited due to Synopsys's policies, based on studies [35, 36, 37, 38], where authors utilized U-Net or its 3D extension for similar medical image segmentation tasks, it can be assumed that Simpleware Software auto segmentation tools are based on U-Net architecture.

In addition to AI-powered tools, Simpleware Software offers semi-automatic segmentation options, including the **region growing, split regions and watershed tools**. The software also provides a range of basic 2D and 3D segmentation tools such as the **paint, threshold, paint with threshold, erase, and scissors tools** [39].

Use of the Simpleware Software

In this work, an on-site installed trial version of Simpleware Software from Synopsys was utilized for advanced 3D image processing.

For upper airways segmentation from CT scans, the **CMF CT auto segmentation tool** was employed. After importing the CT scan into the software and selecting the auto segmentation CMF CT tool (as shown in the left-hand side image of Figure 2.6), the anatomical structures to be segmented were determined by selecting the appropriate parts in the model of the head and neck (as illustrated in the right-hand side image of Figure 2.6). Among the anatomical areas offered for segmentation by the CMF CT tool (such as skull, mandible, teeth, cervical spine, airways, ear canal, cranial cavity, eyes, and optic nerves), only the *airways* were toggled on (depicted by the blue color in the nasal and trachea regions). Subsequently, after applying auto segmentation, a segmentation mask of the upper airways was created within a few minutes.

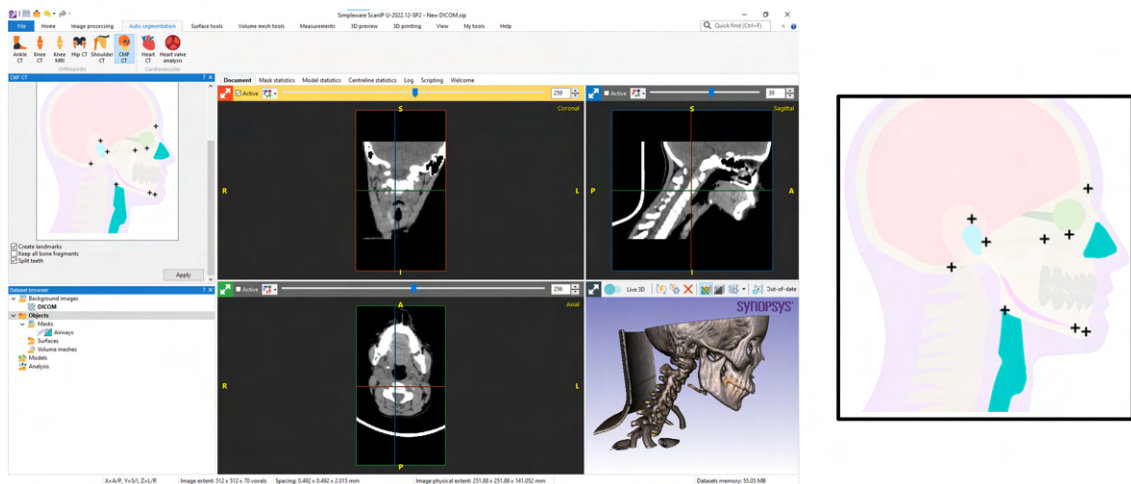


Fig. 2.6: The user-interface of Simpleware Software after importing the CT scan and choosing the auto segmentation CMF CT tool is depicted in the left-hand side image. In the right-hand side image, a model of the head and neck is displayed, indicating the anatomical structures that can be segmented.

After a visual assessment of the original segmentation results, in both 2D and 3D views, it became evident that some additional clean-up and adjustments were

necessary due to false positive marked areas and missing parts of the upper airways.

To eliminate unwanted regions and false positive marked parts, the **crop tool** in 3D view was used to bound and delete unwanted areas, while the **erase tool** in 2D slice view was utilized for fine adjustments.

To fill in the regions missed by the auto-segmentation tool, the **pen tool** and **region growing tool** were employed in a slice-by-slice approach. Particularly, the region growing tool proved to be very useful for filling in the missed regions of the airway due to the high contrast between the air and the surrounding tissues. In each slice, a seed point was placed inside the unmarked upper airways anatomy region, and the threshold value was optimized based on visual control of the marked area.

The final adjusted 3D models of the upper airways were directly converted to surface models and exported in STL format.

2.4.3 3D U-Net Model for Automatic Segmentation of the Upper Airways

The 3D U-Net model for automatic segmentation of the human upper airways from CT images was developed as part of the master’s thesis [40]. This automatic deep learning-based tool generates precise 3D models of the upper airways from CT scans of the head and upper body.

For data loading and model training, a PyTorch-based framework for deep learning called Medical Open Network for AI (MONAI) was utilized. MONAI’s built-in U-Net architecture, combined with the ADAM optimizer, was used. Training of the model was conducted on an augmented dataset comprising 154 manually labeled CT scans. All the scans were recorded in the transversal plane. Pixel intensity values were normalized to [0, 1] range. The 3D U-Net model was trained with the following hyperparameters: learning rate: 10^{-3} , weight decay: 10^{-5} , number of residual units: 5, number of layers in 3D U-Net: 5, number of epochs: 100.

The output of the U-Net model is a confidence map, which is an array with the same dimensions as the input and each pixel is classified as either part of the target or not. Each pixel is assigned a score between 0 (background) and 1 (foreground/object), representing the model’s certainty of classification. The default threshold for the foreground was set to 0.5 (during the model training). Pixels with values above this threshold were considered as object (foreground).

During testing, the 3D U-Net model achieved a Dice score of 0.923 and a Hausdorff distance of 102 pixels. The model has shown generalizability for segmenting coronal, sagittal, and transverse acquisitions. The resulting output of the model is an upper airways segmentation in NIfTI file format [40].

Use of the 3D U-Net Model for Automatic Segmentation of the Upper Airways

The process of automatic segmentation of the upper airways using the 3D U-Net model was performed in the Jupyter Notebook environment.

Initially, CT scans in NIfTI file format were loaded. Subsequently, image transformations were applied to each CT scan (input sample) using the MONAI library's **Compose** functionality based on PyTorch. These transformations included loading the image, scaling intensity into the range $[0, 1]$, and padding to ensure the volume depth was divisible by 16. The transformed data were stored for later availability.

Next, the 3D U-Net architecture was initialized with specific parameters, and an optimizer (Adam) was initialized with a specified learning rate and weight decay. These parameters were set appropriately for the used model (learning rate: 10^{-3} , weight decay: 10^{-5} , number of residual units: 5, number of layers in 3D U-Net: 5). The trained 3D U-Net model was then loaded with saved weights and optimizer state. Inference was performed on the transformed CT data using the trained 3D U-Net model.

Since the model's output is a probability map where each value represents the probability of the corresponding pixel being part of the upper airways, it was thresholded at 0.1 to obtain binary segmentation mask. The binary segmentation results (numpy array) were saved as NIfTI image files.

Following a visual inspection of the original segmentation results in the 3D Slicer software, it became apparent that additional clean-up steps were necessary. The original models contained numerous false positive marked areas and structures, that has to be manually removed using the **crop tool**.

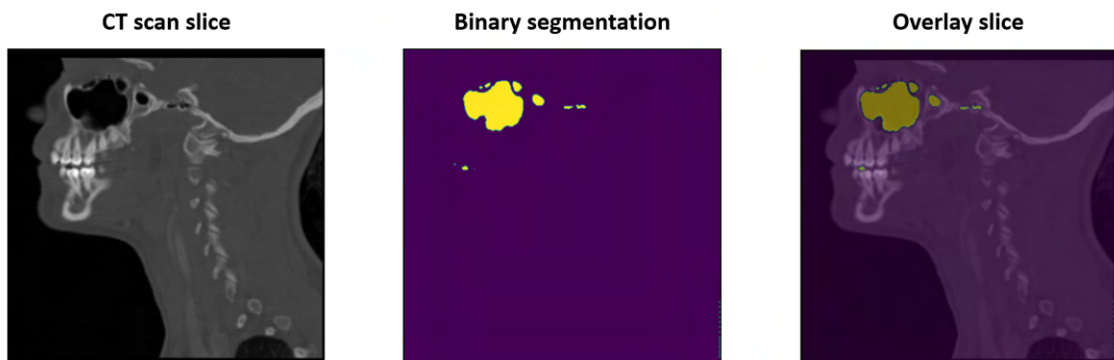


Fig. 2.7: The original segmentation mask created by the 3D U-Net model for one CT slice.

In Figure 2.7, the left-hand side image depicts one selected slice of the CT scan of patient X4_17YF. In the middle image, the original binary segmentation mask created by the 3D U-Net model method is displayed. The right-hand side image

shows an overlay of the binary segmentation mask and the original CT slice. In this overlay slice, false-positive marked structures in the ear and mouth areas can be observed.

The Jupyter Notebook and Python code utilized for automatic upper airways segmentation can be provided upon request and approval from the author [40].

2.5 Spatial Registration of Models

The upper airway models generated from individual CT scans using the five above-described methods were imported into 3D Slicer as individual *models* in groups, with one group containing five models for a particular CT scan. Upon inspection, it was observed that the 3D models exported from different software exhibited in 3D view spatial shifts or rotations, resulting in their spatial misalignment. For comparative analysis of resulting models, which is going to be described in the following Chapter 2.6, it was necessary to align all the models to spatially fit each other. Therefore, manual registration of the models was conducted using the transforms module in 3D Slicer.

Within the *transforms module*, **linear transformation** was employed. Through manual manipulation of sliders, the model to be transformed was translated or rotated along three axes to achieve position and orientation alignment of models in 3D space. The registration process involved careful visual examination of the models alignment from various orientations in 3D view, with multiple fine adjustments made to ensure accurate alignment.

It is worth noting that due to the high complexity and certain differences in the shapes of the models, the final registration of the models is an approximation that was subjectively visually assessed as the best fitting alignment of the models.

2.6 Comparative Analysis

2.6.1 Quantitative Characterization of Models' Geometry

For the quantitative characterization of the resulting models' geometry, three metrics were employed: the number of triangles, the model surface area, and the volume of the surface model. These metrics were calculated using the *segment statistics* module in 3D Slicer.

- **The number of triangles:** This metric offers insights into the complexity, smoothness, and level of detail of the 3D triangular surface model. A higher number of triangles indicates a smoother and more complex and detailed surface, as it allows for finer-grained representation of curves and complex shapes.

- **The model surface area:** Measured in square millimeters (mm^2), this metric represents the total area of the 3D model surface. It reflects the complexity and the extent of detail present in the model.
- **The volume of the surface model:** Measured in cubic millimeters (mm^3), this metric represents the space enclosed by the surfaces of the 3D model. Essentially, it quantifies the total volume occupied by the model's geometry.

2.6.2 Characterization of Models' Geometry in Relation to the Target Model

For further characterization of the models' geometry in relation to the target model, two numerical metrics were utilized: the volume of models intersection and the Dice coefficient. Additionally, a model-to-model distance map was used for visual comparison of the models. These approaches involved the use of spatially registered models, with the models created by the MVA method designated as the target model, serving as the equivalent of the ground truth model.

- **Volume of models intersection:** This metric, measured in cubic millimeters (mm^3), represents the overlapping regions and shared volume between the target model (MVA model) and the compared model created by another method.

The calculation of this metric was performed using 3D Slicer. Firstly, the two models were uploaded as *segmentations* and added to a common segmentation node in *data* module. Then, in the *segment editor* module, the target segmentation mask (created by the MVA method) was activated, and the **logical operators** tool was used to apply the **intersect** operation for the target and compared segmentation masks. Subsequently, the *segment statistics* module was employed to calculate the shared volume.

- **Dice coefficient:** This coefficient, described in Section 1.2.4, was calculated for the target model and compared model using the *segment comparison* module in 3D Slicer. After uploading the two models as *segmentations*, the *segment comparison* module was launched, and the Dice similarity metrics computation was applied.
- **Model-to-model distance:** This metric describes the geometry differences between two models. The resulting color-coded model illustrates the shape distances between the compared model and the target model (created by the MVA method). Distance is measured in millimetres (mm).

To create the colored distance model, the *model-to-model distance* module in 3D Slicer was utilized. The compared upper airways model was set as the **source model**, while the upper airways model created by the MVA method

was set as the **target model**. The distance metric chosen was **signed closest point**. After applying the method, a color-coded model describing the distance from the target model was generated. For the color representation of model-to-model distance, the *PET-Rainbow2* color map was selected in the *colors* module.

The **signed closest point** distance metric indicates that the sign of the distance (negative vs. positive) depends on whether one model is inside the other. This computation is relative to the target model, meaning that if the compared model is inside the target model at a given point, then that distance will be negative and color-coded based on the color legend.

For a more detailed analysis, the upper airway models created from one CT scan (X1_63YM) using all the 5 methods were subdivided into four anatomical parts: trachea, larynx, pharynx, and nasal cavity with sinuses (as depicted in the Figure 2.8). All the above-mentioned metrics were also determined for these anatomical parts.

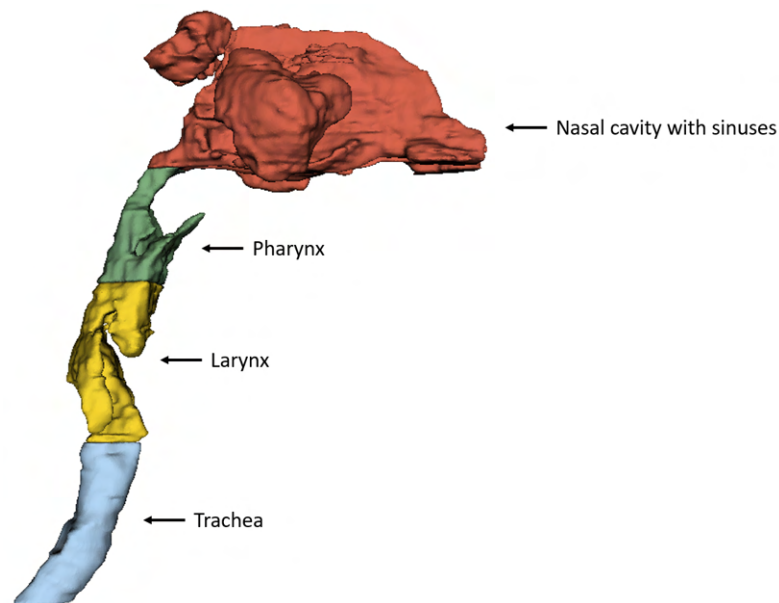


Fig. 2.8: The upper airways model divided into 4 anatomical parts - red marked nasal cavity with sinuses, green marked pharynx, yellow marked larynx and blue marked trachea.

2.7 CFD Simulation

The final stage of the workflow, as depicted in Figure 2.1, involved CFD simulation. A crucial step of CFD simulation is the generation of the model mesh, which means

dividing the geometry model into numerous small connected elements. Before meshing the model, it was necessary to repair the upper airways model and define model boundaries, including inlets, outlets, and wall.

2.7.1 Repair of the Model

Since the geometric model to be meshed must be relatively clean and error-free, it was necessary to address errors such as overlapping regions, non-manifold geometry and self-intersecting triangles present in the original upper airway models.

To address these errors, the model was repaired using **cleaning and repairing filters** available in MeshLab software. These filters included:

- **Merge close vertices filter:** This filter merged vertices that were closer together than a specified threshold (set at 0.1 mm).
- **Remove duplicate faces filter:** This filter eliminated faces (elements) composed of the same set of vertices.
- **Remove isolated pieces filter:** This filter removed isolated connected components with a diameter smaller than a specified constant. The maximum diameter of isolated pieces to be removed was determined based on visual assessment of the model.
- **Remove unreferenced vertices filter:** This filter checked each vertex on the mesh. If a vertex was not referenced by a face, the filter removed it.

2.7.2 Definition of Model Boundaries

Defining the boundaries of the model involved specifying the inlets, outlet, and wall. **Inlets** represent the points where air enters the respiratory system, while **outlet** represent the point where air exits the upper respiratory system. **Wall** represent the surfaces within the model that restrict air flow, including nasal cavity, pharynx, larynx, and trachea.

The repaired model was imported into ANSYS (2024) Space Claim, where the model's inlets and outlet were defined using the **select tool**. The left and right nostrils were defined as inlets, and surface mesh triangles in the region of the nostrils were marked using the select tool. **Named selections** (in the *groups table*) were created for these marked regions. Similarly, the model's outlet was defined in the tracheal closure area using the same procedure. The remaining surface of the model was designated as the wall. Model inlets, outlet, and wall are depicted in Figure 2.9.

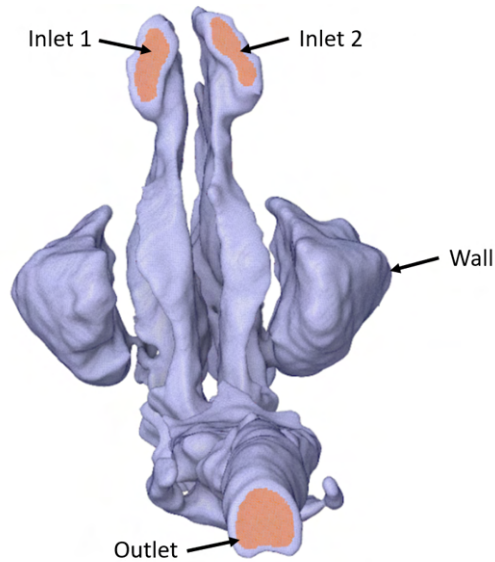


Fig. 2.9: Defined model's boundaries. The model's boundaries were defined in the nostril area, labeled as inlet 1 and inlet 2, and in the tracheal closure area, labeled as outlet. The remaining surface of the model was designated as the wall.

The repaired model with defined boundaries was exported in ANSYS .scdoc format.

2.7.3 Meshing of the Model

For meshing of the geometry model, ANSYS (2024) Fluent software with **meshing** mode was utilized. The **watertight geometry workflow** was selected, and predefined steps of the workflow were followed. The upper airways model (repaired and with defined boundary conditions) was imported as a CAD file format, and subsequently, the **surface mesh** was generated. Inlet boundaries were designated as **velocity inlet**, and the outlet boundary was designated as **pressure outlet**. The model wall was designated as the **fluid domain**. The **volume mesh** was generated with poly-hexcore meshing elements (a combination of polyhedral and hexahedral elements).

2.7.4 CFD Simulation Computation

For the computation of the CFD simulation was employed ANSYS (2024) Fluent software with **solution** mode. Upon uploading the meshed model into solution mode, boundary conditions for inlets, outlet, and wall were defined. The fluid material used was **air**, with default physical properties. A **velocity magnitude** of 5 m/s was set for inlet 1 and 2. For **pressure outlet** were retained default

parameters with a Gauge pressure of 0 Pa. Default conditions were also retained for the model wall. For the CFD solution calculation, 50 iterations were set. Following the CFD simulation calculation, contours plot was utilized for the visualization of the CFD simulation results.

3 Results

In this chapter will be displayed, described, and compared the resulting 3D upper airway models generated by the 5 used methods. For visualization purposes only the models generated from one CT scan (X1_63YF) will be used. All other models generated by the 5 methods from the remaining CT scans will be provided for viewing in the Appendix.

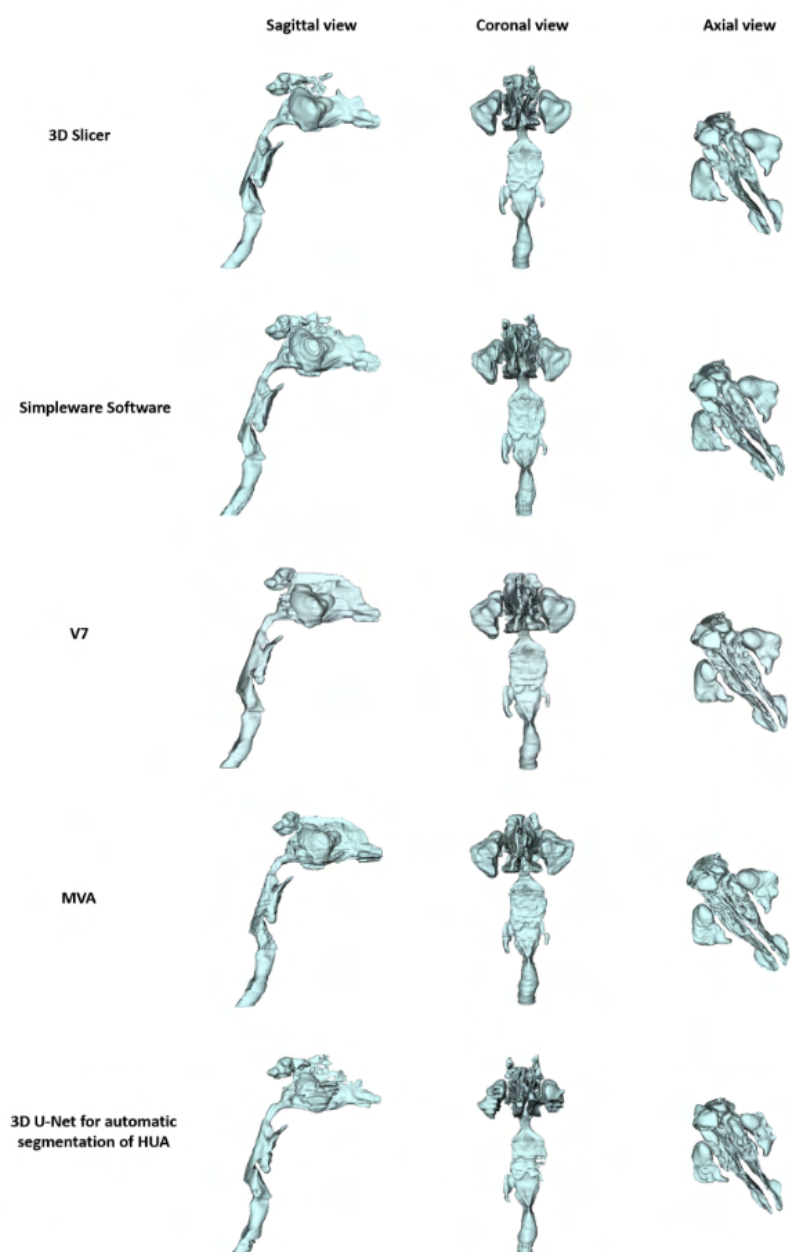


Fig. 3.1: Table of resulting 3D upper airway models for CT scan of patient X1_63YF. Models obtained by all the 5 methods are shown in 3 views: sagittal, coronal, and axial.

In Figure 5.5, the resulting 3D upper airway models generated by the 5 methods from one CT scan are presented. These models are shown in three views: sagittal, coronal, and axial. In the following sections, metrics calculated for characterization of all the 3D upper airway models generated from the 6 CT scans using the 5 methods will be presented. Based on the calculated values of the metrics, the 5 methods used will be compared and evaluated.

3.1 Comparative Analysis

3.1.1 Quantitative Characterization of Models' Geometry

All three metrics utilized for the quantitative characterization of the resulting models' geometry, described in detail in Section 2.6.1, were calculated for all models generated by the 5 methods from the 6 CT scans. The results are presented in Table 3.1 to Table 3.6.

To address the space constraints of the cells within the table, the names of the individual metrics will be abbreviated as follows:

- **NoT** stands for „number of triangles“
- **MSA** stands for „model surface area“
- **VotSM** stands for „volume of the surface model“

Method	NoT	MSA (mm ²)	VotSM (mm ³)
3D Slicer	395168	130612	595502
Simpleware Software	467652	159160	721249
V7	475844	155749	718416
MVA	516552	158612	694507
3D U-Net model	401156	136644	518418

Table 3.1: Table of metrics for the quantitative characterization of the resulting models' geometry - CT scan of patient **X1_63YF**.

Method	NoT	MSA (mm ²)	VotSM (mm ³)
3D Slicer	414068	46200	123955
Simpleware Software	420140	46526	137504
V7	341628	42383	116999
MVA	439416	47081	120723
3D U-Net model	371568	42635	151054

Table 3.2: Table of metrics for the quantitative characterization of the resulting models' geometry - CT scan of patient **X2_59YM**.

Method	NoT	MSA (mm ²)	VotSM (mm ³)
3D Slicer	210136	23772	53231
Simpleware Software	177392	22862	45060
V7	207072	24074	46294
MVA	211456	23505	52281
3D U-Net model	210600	22104	52536

Table 3.3: Table of metrics for the quantitative characterization of the resulting models' geometry - CT scan of patient **X3_15YM**.

Method	NoT	MSA (mm ²)	VotSM (mm ³)
3D Slicer	324688	35429	82066
Simpleware Software	305852	36196	98012
V7	322952	35469	113402
MVA	342584	36752	84253
3D U-Net model	332744	33338	85635

Table 3.4: Table of metrics for the quantitative characterization of the resulting models' geometry - CT scan of patient **X4_17YF**.

Method	NoT	MSA (mm ²)	VotSM (mm ³)
3D Slicer	175820	25388	77861
Simpleware Software	186789	28442	82637
V7	189592	26666	92000
MVA	188300	26578	65358
3D U-Net model	194888	27166	65489

Table 3.5: Table of metrics for the quantitative characterization of the resulting models' geometry - CT scan of patient **X5_12YF**.

Method	NoT	MSA (mm ²)	VotSM (mm ³)
3D Slicer	290204	19900	34618
Simpleware Software	266316	19419	29875
V7	280968	19529	30221
MVA	278572	18776	31202
3D U-Net model	277448	17975	29729

Table 3.6: Table of metrics for the quantitative characterization of the resulting models' geometry - CT scan of patient **X6_7YM**.

For comparison of the 5 methods used for generation of the upper airway models, the **mean values of the 3 metrics** were calculated for each method (see Table 3.7). These mean values were computed from the corresponding 6 values (6 models) listed in Table 3.1 to Table 3.6. The highest mean value for each metric is highlighted in **bold**.

Method	Mean NoT	Mean MSA (mm ²)	Mean VotSM (mm ³)
3D Slicer	301681	46884	161206
Simpleware Software	304024	52101	185723
V7	303009	50645	186222
MVA	329480	51884	174721
3D U-Net model	298067	46644	150477

Table 3.7: Table of the mean values of the 3 metrics for the 5 methods.

The mean values of the 3 metrics for each of the 5 methods are also visualized in Figure 3.4.

QUANTITATIVE CHARACTERIZATION OF MODEL GEOMETRY

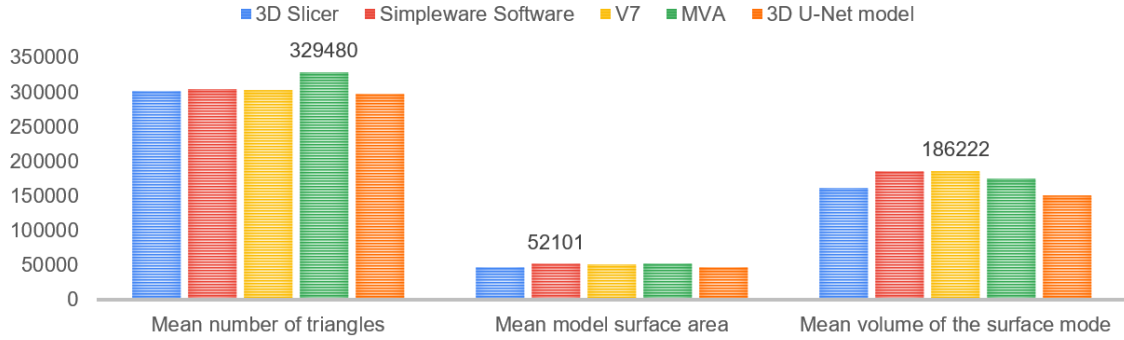


Fig. 3.2: Graph of the mean values of the number of triangles, model surface area and volume of the surface model metrics for the 5 methods.

Based on the mean values of the metrics in Table 3.7 and Figure 3.2, it is observed that the models created by the MVA method have the highest mean number of triangles (NoT 329480). The models created by the Simpleware Software method reached the highest mean model surface area (MSA 52101 mm²) and the highest mean volume of the surface model (VotSM 186222 mm³) achieved the models created by the V7 method. On the other hand, the models created by the 3D U-Net model method showed the lowest mean values for all metrics.

Method	Mean difference of NoT	STD of NoT differences	Mean difference of MSA	STD of MSA differences	Mean difference of VotSM	STD of VotSM differences
3D Slicer	-8,44%	14%	-9,64%	22%	-7,74%	24%
Simpleware Software	-7,73%	5,32%	0,418%	2%	6,30%	7%
V7	-8,03%	12%	-2,39%	4%	6,58%	10%
3D U-Net model	-9,53%	14,96%	-10,10%	16%	-13,88%	43%

Table 3.8: Table of the mean difference and standard deviation of differences of the four methods compared to the MVA (reference) method. The mean difference and the STD of differences are expressed in percentages (%) and were calculated for the three quantitative metrics.

Additionally, based on Table 3.8, it can be argued that the upper airway models most closely resembling those created by the MVA method were generated by the Simpleware Software method. The models created by the Simpleware Software method differ from those created by the MVA method in the mean NoT by -7.73%

(with STD of 5,32%), mean MSA by 0.418% (with STD of 2%), and mean VotSM by 6.3% (with STD of 7%).

3.1.2 Characterization of Models' Geometry in Relation to the Target Model

For a further characterization of the resulting models' geometry, the upper airway models created using 3D Slicer, Simpleware Software, V7, and 3D U-Net model were compared to those created using the MVA method.

The metrics employed for this characterization, described in detail in Section 2.6.2, were calculated for all models generated by the 5 methods from the 6 CT scans.

Dice Coefficient

In Table 3.17, Dice coefficients calculated for all the upper airway models are presented. To accommodate the space constraints of the cells within the table, the names of the 6 CT scans will be abbreviated:

- **X1** stands for CT scan of patinet X1_63YF
- **X2** stands for CT scan of patinet X2_59YM
- **X3** stands for CT scan of patinet X3_15YM
- **X4** stands for CT scan of patinet X4_17YF
- **X5** stands for CT scan of patinet X5_12YF
- **X6** stands for CT scan of patinet X6_7YM

Method	X1	X2	X3	X4	X5	X6
3D Slicer	0,89	0,91	0,90	0,90	0,83	0,83
Simpleware Software	0,89	0,91	0,84	0,88	0,82	0,77
V7	0,90	0,88	0,84	0,83	0,78	0,81
MVA						
3D U-Net model	0,79	0,85	0,87	0,88	0,81	0,83

Table 3.9: Table of Dice coefficients calculated for all the upper airway models created from the 6 CT scans. To the models created by the MVA method, the models generated using the remaining methods were compared.

Mean values and standard deviations (STD) of the Dice coefficients were calculated for each method to compare which of the methods generated the most spatially similar upper airway models to those produced by the MVA method.

Method	Mean of the Dice coefficient	STD of the Dice coefficient
3D Slicer	0,883	0,030
Simpleware Software	0,852	0,048
V7	0,844	0,040
MVA		
3D U-Net model	0,839	0,033

Table 3.10: Table of mean values and standard deviations of the Dice coefficients for each method.

Based on the mean values and standard deviations of the Dice coefficient presented in Table 3.10, it was found that the models generated by the **3D Slicer method** reached the highest mean Dice coefficient (0.0883) with the standard deviation (0.03). Conversely, the models created by the 3D U-Net model method showed the lowest mean Dice coefficient (0.839).

Table 3.17 displays the Dice coefficients calculated for all the upper airway models created from 6 CT scans. The highest Dice coefficients were calculated for the 3D upper airway models generated by the 3D Slicer and Simpleware Software methods from the CT scan X2_59YM, both reached a value of 0.91. In contrast, the upper airway model created by the Simpleware Software method from the CT scan X6_7YM exhibited the lowest Dice coefficient value (0.77).

Volume of Models Intersection

The volume of models intersection metric was originally calculated in cubic millimeters (mm^3), however, conversion to percentages was performed for better clarity.

In Table 3.11, the results of the volume intersection between the MVA upper airway models and the models created by another methods are presented.

Due to the space constraints of the cells within the table, the same abbreviations of CT scan names will be used as in the previous section for Dice coefficient.

Method	X1	X2	X3	X4	X5	X6
3D Slicer	82%	93%	91%	89%	91%	91%
Simpleware Software	91%	98%	78%	95%	93%	75%
V7	92%	87%	80%	98%	94%	80%
MVA						
3D U-Net model	69%	97%	87%	89%	81%	82%

Table 3.11: Table of the volume of models intersection metric (in %) calculated for all the upper airway models created from the 6 CT scans. To the models created by the MVA method, the models generated using the remaining methods were compared.

Mean values (in %) and standard deviations of the volume of models intersection were calculated for each method.

Method	Mean intersection volume	STD of the intersection volume
3D Slicer	89%	0,03
Simpleware Software	88%	0,09
V7	89%	0,07
MVA		
3D U-Net model	84%	0,08

Table 3.12: Table of mean values (in %) and standard deviations of the volume of models intersection for each method.

Based on the mean values (in %) and standard deviations of the volume of models intersection presented in Table 3.12, it was found that the highest mean intersection volume (89%) was between upper airway models generated by the MVA method and the **3D Slicer** method. The models generated by the V7 method also achieved a 89% mean intersection volume with the MVA-generated models, but the STD of the intersection volume (0.07) was higher than that of the 3D Slicer method (0.03). On the other hand, the lowest mean intersection volume (84%) was between models created by the MVA method and the 3D U-Net model method.

Table 3.11 shows the volume of models intersection metric (in %) calculated for all the upper airway models created from 6 CT scans. The highest intersection volumes (98%) were calculated between upper airway models generated from CT scan X2_59YM by the MVA method and the Simpleware Software method, and between upper airway models generated from CT scan X4_17YF by the MVA method and the V7 method. In contrast, the upper airway model created by the 3D U-Net model

method from the CT scan X1_63YF exhibited the lowest volume intersection (69%) with the upper airway model created by the MVA method.

Model-to-model Distance Maps

Model-to-model distance maps were created for visual comparison of the upper airway models generated by the 5 methods from the 6 CT scans. In this section, only the model-to-model distance maps created for upper airway models generated from one CT scan (X1_63YF) using the 5 methods will be used for visualization (see Figure 3.3). All remaining model-to-model distance maps will be provided for viewing in the Appendix.

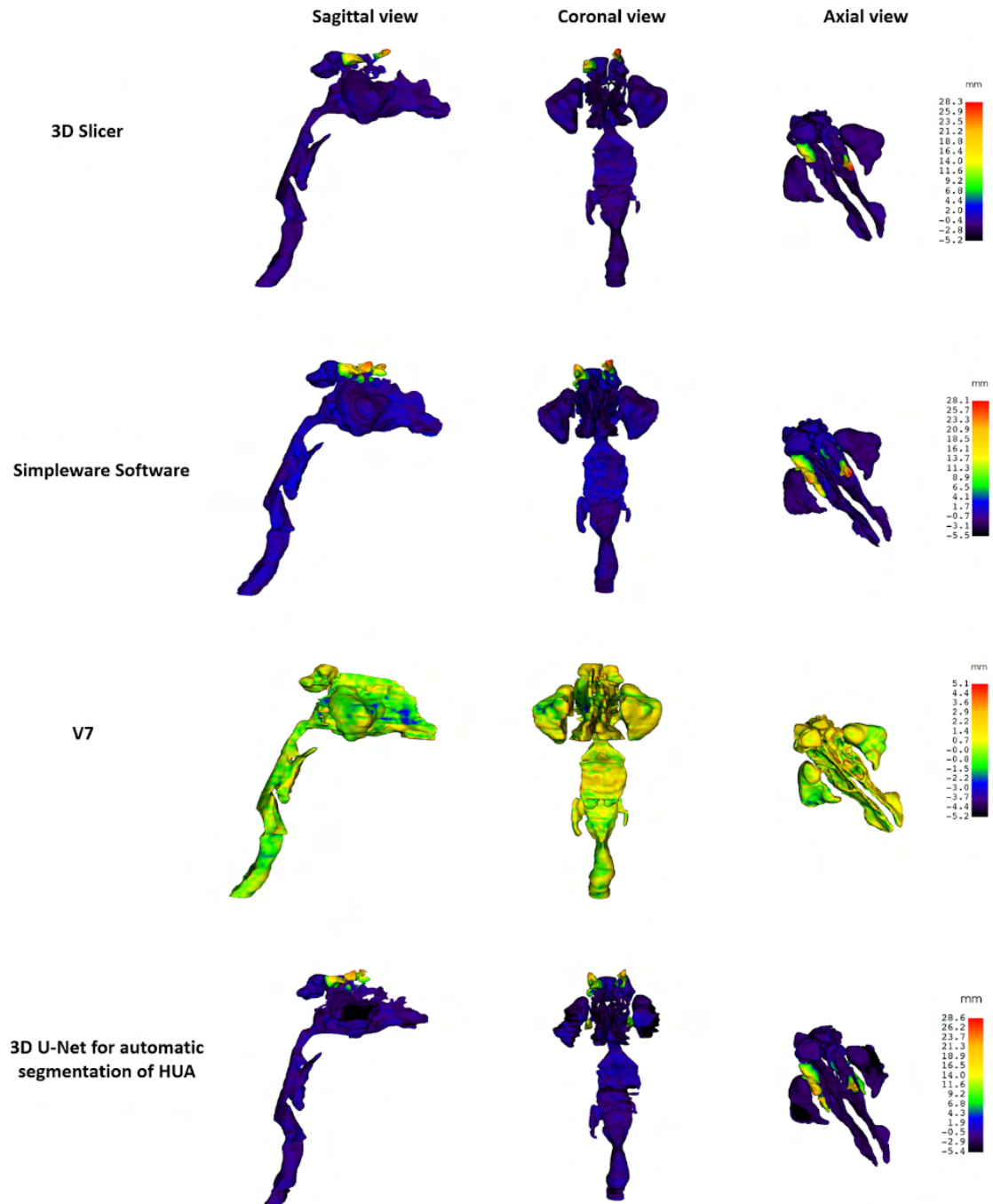


Fig. 3.3: The model-to-model distance maps created for upper airway models generated from CT scan X1_63YF using the 5 methods. The color-coded upper airway models are presented in sagittal, coronal and axial views. For each color-coded upper airway model is shown color scale explaining color coding of shape distances between models.

In Figure 3.3, color-coded upper airway models are depicted, illustrating the shape differences of the source models (created by the 3D Slicer, Simpleware Soft-

ware, V7 and 3D U-Net model methods) compared to the target model (created by the MVA method). The resulting color-coded models retain the original shape of the source model, with the surface of the model colored based on the shape difference with the target model (created by MVA method). Based on the shape distances between models, expressed in *mm* (see color scale on the right-hand side), the narrowest range of distance values can be observed between the upper airway models created by the MVA method and the V7 method, ranging from 5.1 mm to -5.2 mm. Conversely, the widest range of distance values is observed between the models generated by the MVA method and the 3D U-Net model method, spanning from 28.6 mm to -5.4 mm.

3.1.3 Detailed Analysis of Upper Airway Models by Individual Anatomical Parts

For a more detailed and deeper analysis, all the used metrics were calculated also for 4 separated anatomical parts of the 5 upper airways models generated from the CT scan of patient X1_63YF. The 5 upper airway models divided into 4 individual anatomical parts (nasal cavity with sinuses, pharynx, larynx, trachea) are depicted in Figure 3.4.

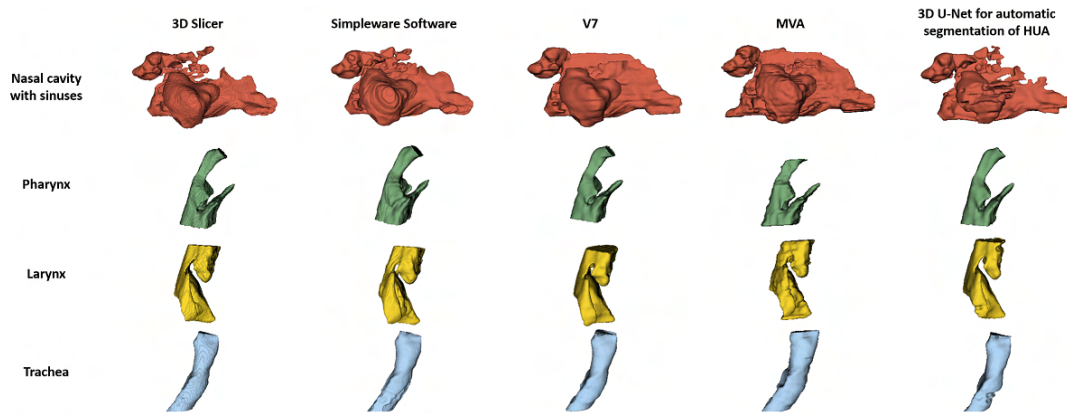


Fig. 3.4: The 5 upper airway models divided into 4 individual anatomical parts. The nasal cavity with sinuses is coloured red, pharynx green, larynx yellow, and trachea blue.

Quantitative Characterization of Anatomical Parts' Geometry

The metrics calculated for individual anatomical parts of upper airway models generated by the 5 methods are presented in Table 3.13 to Table 3.16.

The names of the individual metrics will be abbreviated as in the Section 3.1.1.

Method	NoT	MSA (mm ²)	VotSM (mm ³)
3D Slicer	265388	91774	364146
Simpleware Software	312708	109534	459234
V7	309500	107749	452574
MVA	366420	112537	438793
3D U-Net model	270256	92052	294460

Table 3.13: Table of metrics for the quantitative characterization of the **nasal cavity and sinuses** geometry.

The quantitative characterization of the **nasal cavity and sinuses** geometry, see Table 3.13, revealed that the MVA method reached the highest values for the metrics NoT (366420) and MSA (112537 mm²), while the Simpleware Software method obtained the highest value for the metric VotSM (459234 mm³). Conversely, the 3D Slicer method exhibited the lowest values for both NoT (265388) and MSA (91774 mm²), whereas the 3D U-Net model method had the lowest value for VotSM (294460 mm³). When compared to the MVA method, which served as the reference, the Simpleware Software method showed the closest results, with percentage differences of approximately -14.66% for NoT, -2.67% for MSA, and 4.66% for VotSM.

Method	NoT	MSA (mm ²)	VotSM (mm ³)
3D Slicer	44072	15205	57439
Simpleware Software	48300	16243	68085
V7	47936	16382	68265
MVA	47888	15012	60448
3D U-Net model	44556	15049	58694

Table 3.14: Table of metrics for the quantitative characterization of the **pharynx** geometry.

The quantitative characterization of the **pharynx** geometry, see Table 3.14, showed that among the methods examined, the V7 method reached the highest values for the MSA (16382 mm²) and VotSM (68265 mm³), while the Simpleware Software method recorded the highest NoT value (48300). Conversely, the 3D Slicer method showed the lowest NoT (44072) and VotSM (57439 mm³) values, with the MVA method having the lowest MSA value (15012 mm²). In comparison to the MVA method, which acted as the reference, the 3D U-Net model method showed results closest to it, with percentage differences of approximately -6.95% for NoT, 0.25% for MSA, and -2.9% for VotSM.

Method	NoT	MSA (mm ²)	VotSM (mm ³)
3D Slicer	63436	22083	108907
Simpleware Software	70576	23725	121932
V7	66804	23204	122896
MVA	76340	23814	124399
3D U-Net model	60844	20627	98725

Table 3.15: Table of metrics for the quantitative characterization of the **larynx** geometry.

The quantitative characterization of the **larynx** geometry, see Table 3.15, led to the highest values of all metrics for the MVA method, reaching values for NoT (76340), MSA (23814 mm²) and VotSM (124399 mm³). Conversely, the 3D U-Net model method showed the lowest values for all metrics, with values for NoT (60844), MSA (20627 mm²) and VotSM (98725 mm³). When compared to the MVA method (used as a reference), the Simpleware Software method showed the closest results with percentage differences of approximately -7.55% for NoT, -0.37% for MSA, and -1.98% for VotSM.

Method	NoT	MSA (mm ²)	VotSM (mm ³)
3D Slicer	33268	11597	63711
Simpleware Software	35584	12261	69264
V7	35240	12168	71411
MVA	35700	11789	70767
3D U-Net model	33072	11373	63116

Table 3.16: Table of metrics for the quantitative characterization of the **trachea** geometry.

The quantitative characterization of the **trachea** geometry, see Table 3.16, showed that the MVA method achieved the highest value of NoT (35700). The highest value of MSA (12261 mm²) reached the Simpleware Software method, and the V7 method show highest values of VotSM (71411 mm³). On the other hand, the 3D U-Net model method exhibited the lowest values for all metrics, with values of NoT (33072), MSA (11373 mm²), and VotSM (63116 mm³). When compared to the MVA method (serving as the reference), the V7 method showed the closest results, with percentage differences of approximately -1.29% for NoT, 3.21% for MSA, and 0.91% for VotSM.

Characterization of Anatomical Parts' Geometry in Relation to the Target Model

The anatomical parts' models obtained by subdividing upper airway models created using 3D Slicer, Simpleware Software, V7, and 3D U-Net model were compared to those obtained by subdividing the model created using the MVA method.

Dice Coefficient

In Table 3.17, Dice coefficient values calculated for all the individual anatomical parts of upper airway models are presented.

Method	Nasal cavity with sinuses	Pharynx	Larynx	Trachea
3D Slicer	0,858	0,877	0,915	0,917
Simpleware Software	0,875	0,853	0,909	0,929
V7	0,867	0,884	0,93	0,928
MVA				
3D U-Net model	0,722	0,843	0,85	0,903

Table 3.17: Table of Dice coefficients calculated for all the anatomical parts' models.

Based on the calculated Dice coefficient values presented in Table 3.17, it was observed that the nasal cavity with sinuses anatomical model and the trachea anatomical model obtained by subdividing the upper airways model created by the **Simpleware Software** method exhibited the highest spatial overlap with the corresponding anatomical models obtained by subdividing the MVA-generated upper airways model. The nasal cavity and sinuses anatomical model reached a Dice coefficient value of 0.875, and the trachea anatomical model reached a value of 0.929. Additionally, the pharynx and larynx anatomical models obtained by subdividing the upper airways model created by the **V7** method showed the highest Dice coefficient values (0.884 and 0.93), indicating the highest spatial overlap with those anatomical models obtained by subdividing the MVA-generated upper airways model.

Volume of Models Intersection

Similarly to Section 3.1.2, the volume of models intersection metric was converted from cubic millimeters (mm^3) to percentages.

In Table 3.18, the results of the volume intersection between the anatomical parts' models obtained from the MVA upper airways model and the anatomical parts' models created by subdividing the upper airway models generated by other methods are presented.

Method	Nasal cavity with sinuses	Pharynx	Larynx	Trachea
3D Slicer	79%	85%	86%	87%
Simpleware Software	90%	91%	90%	92%
V7	88%	94%	92%	93%
MVA				
3D U-Net model	60%	83%	76%	85%

Table 3.18: Table of volume of models intersectio calculated for all the anatomical parts' models.

Based on the values (in %) of the volume of models intersection presented in Table 3.18, it was found that the nasal cavity with sinuses anatomical model obtained from the upper airways model created by the **Simpleware Software** method exhibited the highest volume intersection (90%) with the corresponding anatomical model obtained from the upper airways model generated by the MVA method. The pharynx, larynx, and trachea anatomical models obtained from the upper airways model created by the **V7** method showed the highest volume intersection (94%, 92%, and 93%) with the corresponding anatomical models obtained by subdividing the MVA-generated upper airways model.

Model-to-model Distance Maps

In Figures 3.5 to 3.8, model-to-model distance maps for the anatomical parts' models obtained by subdividing the upper airway models generated by the 5 methods are presented. These color-coded anatomical parts' models describe the shape differences between the source models (derived from the upper airway models created by the 3D Slicer, Simpleware Software, V7, and 3D U-Net model methods) and the target anatomical model (created by subdividing the upper airways model generated by the MVA method).

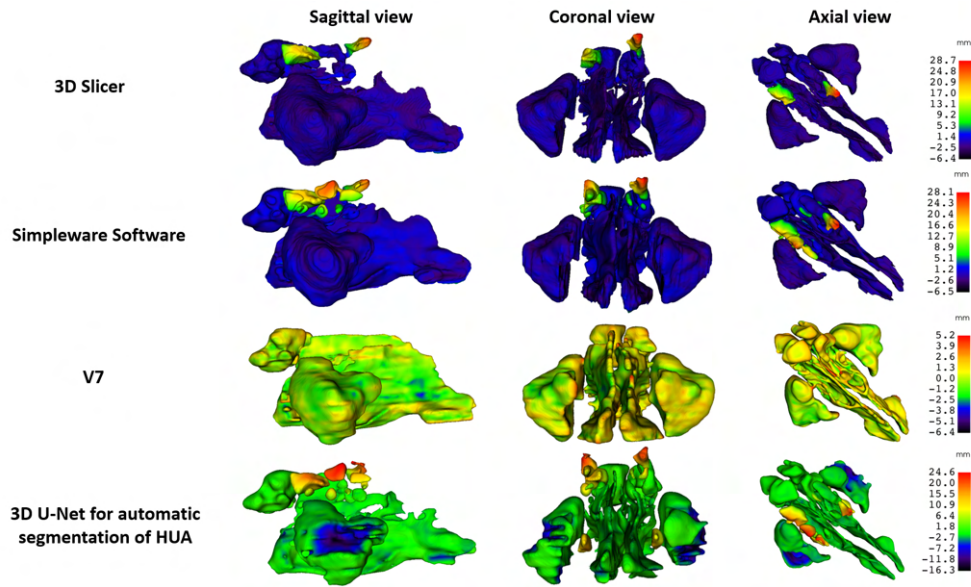


Fig. 3.5: The model-to-model distance maps created for **nasal cavity and sinuses** geometry models.

The model-to-model distance maps created for the **nasal cavity and sinuses** geometry models show that the narrowest range of shape distance values can be observed between the models derived from the upper airway models created by the MVA method and the V7 method, ranging from 5.2 mm to -6.4 mm. Conversely, the widest range of distance values is observed between the models derived from the upper airway models created by the MVA method and the 3D U-Net model method, spanning from 24.6 mm to -16.3 mm.

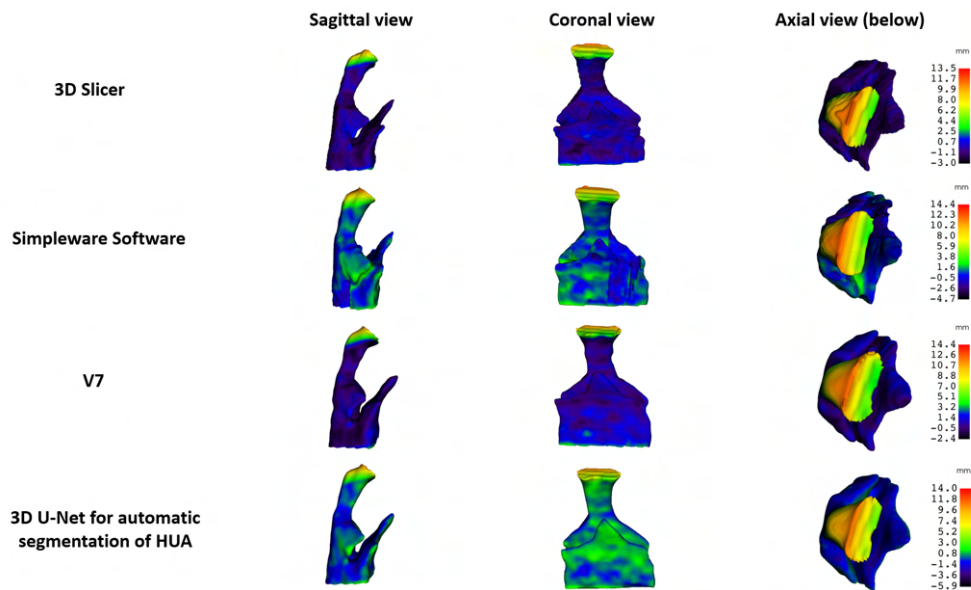


Fig. 3.6: The model-to-model distance maps created for **pharynx** geometry models.

The model-to-model distance maps created for the **pharynx** geometry models show that the narrowest range of shape distance values can be observed between the models derived from the upper airway models created by the MVA method and the 3D Slicer method, ranging from 13.5 mm to -3.0 mm. Conversely, the widest range of distance values is observed between the models derived from the upper airway models created by the MVA method and the 3D U-Net model method, spanning from 14.0 mm to -5.9 mm.

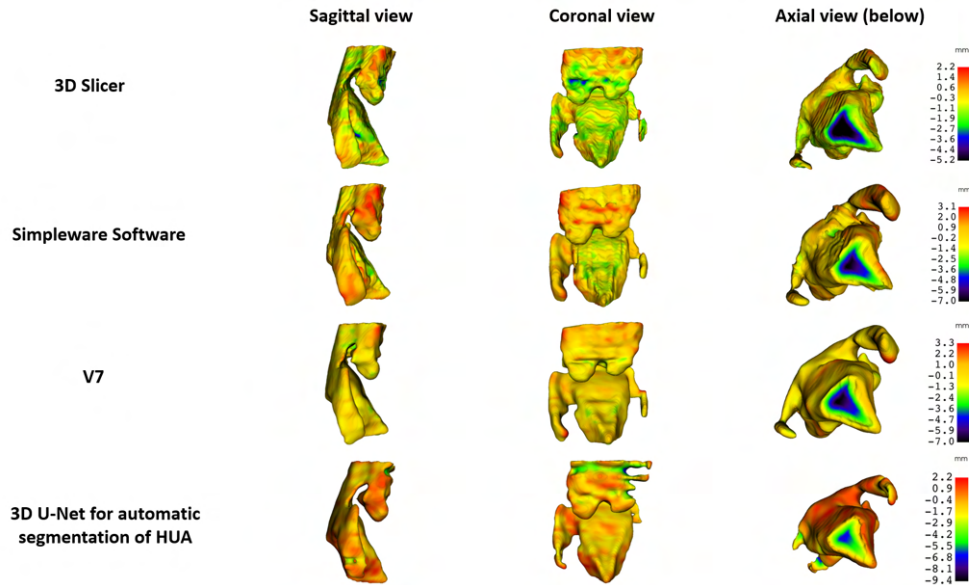


Fig. 3.7: The model-to-model distance maps created for **larynx** geometry models.

The model-to-model distance maps created for the **larynx** geometry models show that the narrowest range of shape distance values can be observed between the models derived from the upper airway models created by the MVA method and the 3D Slicer method, ranging from 2.2 mm to -5.2 mm. Conversely, the widest range of distance values is observed between the models derived from the upper airway models created by the MVA method and the 3D U-Net model method, spanning from 2.2 mm to -9.4 mm.

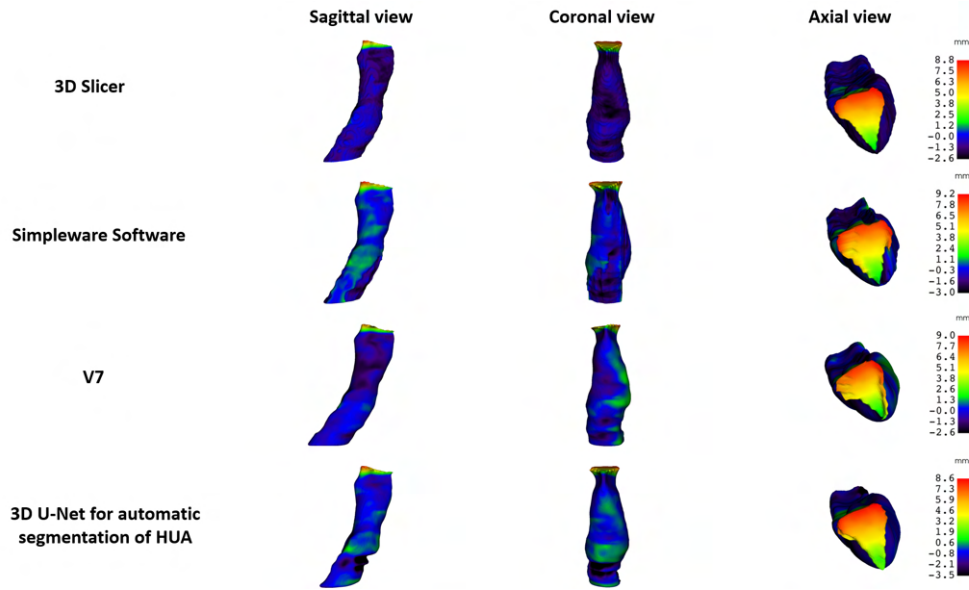


Fig. 3.8: The model-to-model distance maps created for **trachea** geometry models.

The model-to-model distance maps created for the **trachea** geometry models show that the narrowest range of shape distance values can be observed between the models derived from the upper airway models created by the MVA method and the 3D Slicer method, ranging from 8.8 mm to -2.6 mm. Conversely, the widest range of distance values is observed between the models derived from the upper airway models created by the MVA method and the Simpleware Software method, spanning from 9.2 mm to -3.0 mm.

3.2 CFD Simulation

In this work, CFD simulation was performed on the upper airway model created by the MVA method from the CT scan of patient X1_63YF.

3.2.1 Meshing of the Model

Following the workflow described in Section 2.7.3, the **surface mesh** (displayed in Figure 3.9, left-hand side image) and the **volume mesh** (depicted in Figure 3.9, right-hand side image) of the upper airways model were generated.

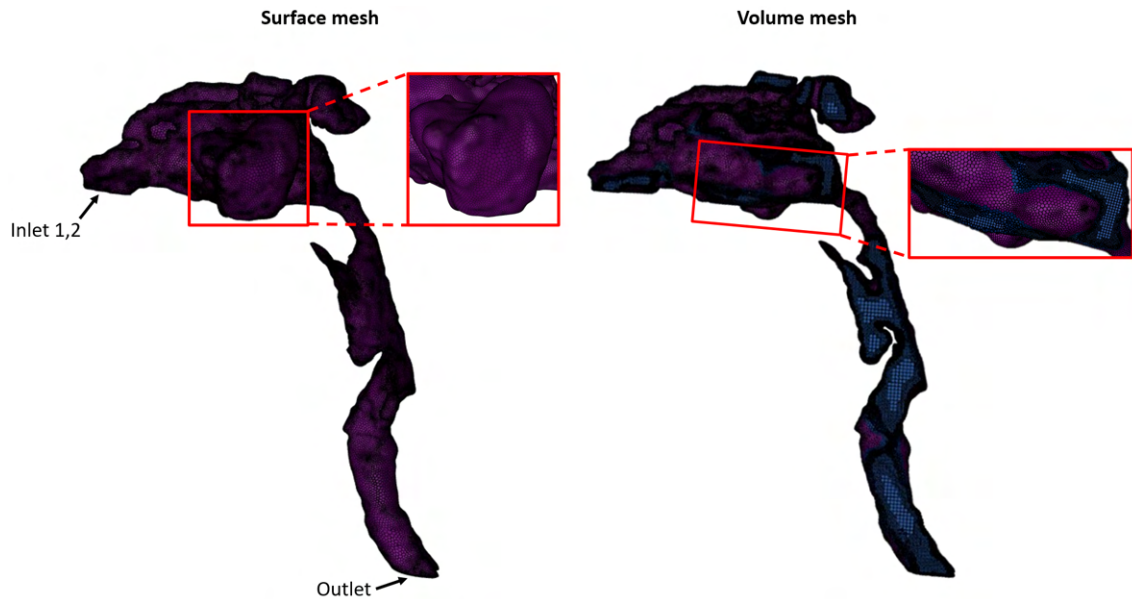


Fig. 3.9: The surface and volume mesh generated for the 3D upper airways model. The left-hand side image displays the 3D surface mesh of the model with defined inlets and outlets. A detailed view shows elements (faces) forming the surface mesh. In the right-hand side image, the volume mesh of the model is shown in longitudinal cross-section. A detailed view depicts poly-hexcore elements forming the volume mesh.

The surface mesh comprised 420434 elements (faces), while the volume mesh consisted of 1038236 cells.

3.2.2 CFD Simulation Computation

The **pressure and velocity contours** were utilized to visualize the CFD results. Figure 3.10 presents the absolute pressure contour model in 4 views. According to the color scale on the left-hand side, the absolute pressure ranged from a minimum of approximately 101250 Pa to a maximum of approximately 101505 Pa. The pressure difference along the path from the nostrils to the end of the trachea was approximately 255 Pa.

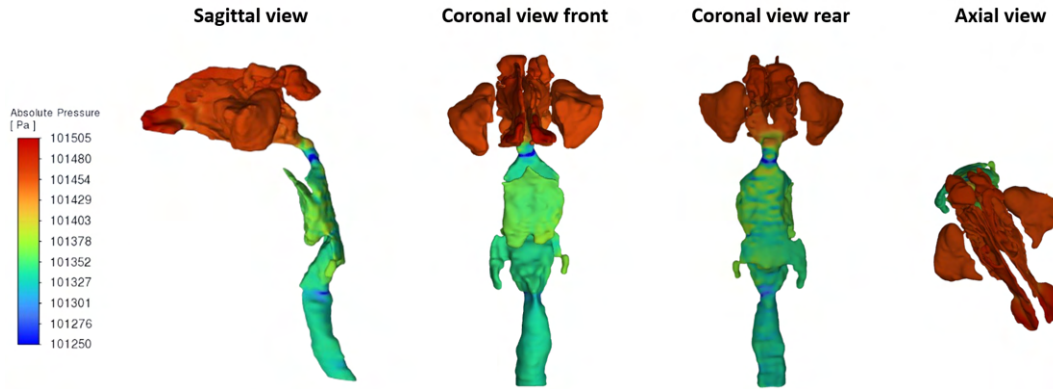


Fig. 3.10: The absolute pressure contour model is displayed in 4 views - sagittal, coronal front and rear, axial. On the left-hand side is depicted color scale explaining color coding of pressure values.

To facilitate understanding of the internal dynamics of the model, the velocity magnitude and absolute pressure contours were displayed in cross-section.

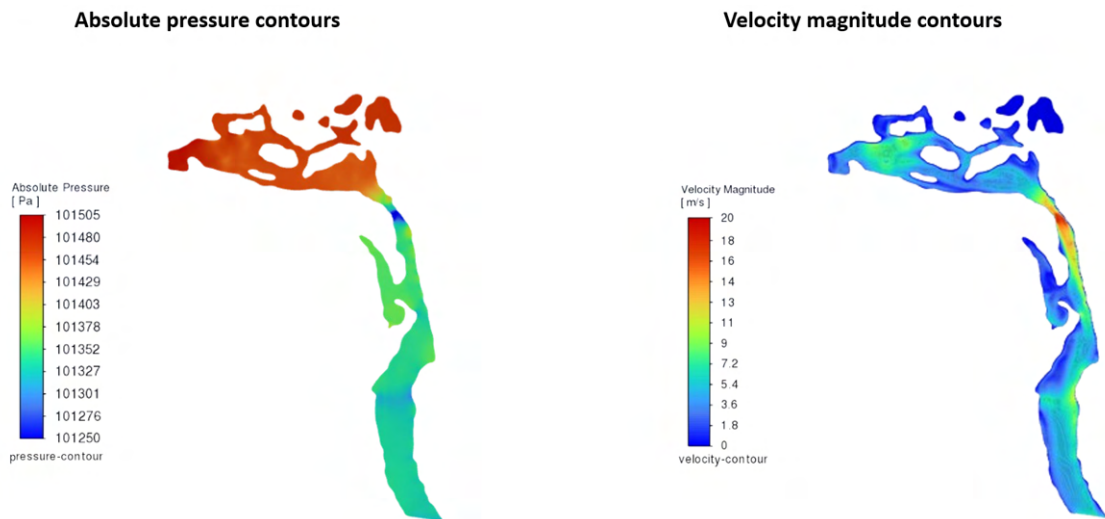


Fig. 3.11: The velocity magnitude and absolute pressure contours in cross-section.

In Figure 3.11, the left-hand side displays the absolute pressure contours cross-section, while the right-hand side shows the velocity magnitude contours cross-section.

In the **velocity magnitude contours** cross-section, a rapid increase in velocity can be observed in the narrowing sections of the model. The first significant increase in velocity magnitude is noticeable in the area behind the nostrils (approximately 8 m/s). The maximum airflow velocity occurs at the connection of the nasal cavity

and pharynx, where the airway anatomy is the narrowest (in this specific cross-section), and the velocity magnitude reaches up to 20 m/s. In the pharynx and larynx, the maximum airflow velocity occurs near the surface of the posterior wall and the epiglottis region (approximately 7 m/s to 11 m/s). A slight decrease in velocity magnitude can be observed in the area of the tracheal outlet (approximately 5 m/s).

In the **absolute pressure contours** cross-section, a slight pressure decrease can be observed through the nasal cavity (approximately up to 101403 Pa). The pressure minimum occurs in the area of the connection between the nasal cavity and pharynx (101250 Pa). The pressure in the pharynx and larynx slightly decreases (approximately up to 101352 Pa), followed by a bit more significant pressure drop in the area where the larynx connects to the trachea (approximately 101276 Pa). The pressure in the trachea remains consistently low (approximately around 101327 Pa).

4 Discussion

4.1 Methods for HUA Models Generation

In the following sections, an evaluation of each method utilized for 3D upper airway models generation will be conducted, considering aspects such as user experience, functionality of the offered tools, and the need for post-processing adjustments.

4.1.1 Medical Volume Annotator

While the **propagation of the label** feature, described in the section 2.3.1, is valuable and time-saving, it requires user-controlled adjustments slice-by-slice. Inaccuracies in labeling, such as leakage into surrounding regions, can accumulate during propagation if not checked and corrected manually slice-by-slice. In the scenario of propagating the area labeled by the thresholding tool, it is essential to regulate both the threshold value of the movable central point and ensure the point remains within the area of interest. Slice-to-slice propagation of labels is generally advantageous in regions where anatomical changes occur less rapidly, such as the trachea, pharynx, and larynx. However, due to the intricate nature of the anatomy in the nasal cavity, extensive user involvement is necessary.

The MVA software also incorporates useful keyboard shortcuts, enabling users to quickly edit, add, or remove labels without continuously holding down the mouse button. It is worth noting that the MVA software restricts annotation to the axial plane only, which may be considered a limitation compared to other software that allows annotation in multiple planes (e.g. coronal, axial, and sagittal).

Given the slice-wise approach of annotations, marked anatomy regions were checked continuously, eliminating the need for any time-consuming post-processing operations, such as the removal of falsely marked regions.

The estimated average time spent annotating the upper airway from a single CT scan is 120 minutes.

Overall, the combination of tools offered by the MVA software can serve as a very effective approach for upper airway annotation. Additionally, the use of keyboard shortcuts speeds up and simplifies the entire annotation process. The overall good impression of the MVA software is enhanced by the pleasant and clear user interface.

4.1.2 V7

In this work, the auto-annotate tool, described in Section 2.3.2, reliably generated precise annotation masks only for anatomical structures with simple shapes, such as the maxillary sinuses - see Figure 4.1.

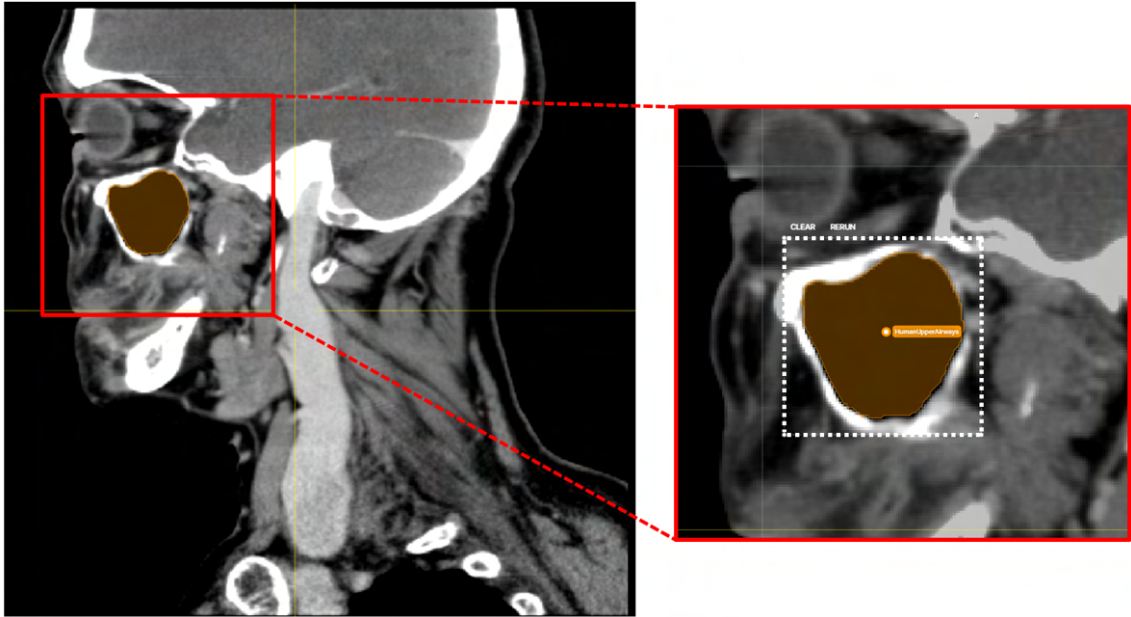


Fig. 4.1: The accurately labeled maxillary sinus area by the auto-annotate tool in the V7 software. On the left-hand side is the sagittal view of the labeled maxillary sinus. On the right-hand side is a detailed depiction of the annotation mask and the rectangular bounding box created to specify the area of interest.

In the case of more complex-shaped anatomical structures, the auto-annotate tool often encountered difficulties and did not accurately delineate the desired areas. When the initial annotation mask was inaccurate or incomplete, the correction tool provided by the auto-annotate tool was utilized to adjust and improve the annotation mask by placing green and red correction points, as illustrated in Figure 4.2 (right-hand side detailed image). Green points were positioned in areas where the desired label was originally missing but expected to be present, while red points were used to exclude parts where the marked area leaked out of the desired anatomical structure of interest. However, despite the correction dots, the marked region was typically only roughly improved - many sharp edges and peaks were created, and some areas were not completely marked. Therefore, to delineate anatomical structures of interest accurately, smoothly, and completely, manual adjustment of the mask boundary points was necessary.

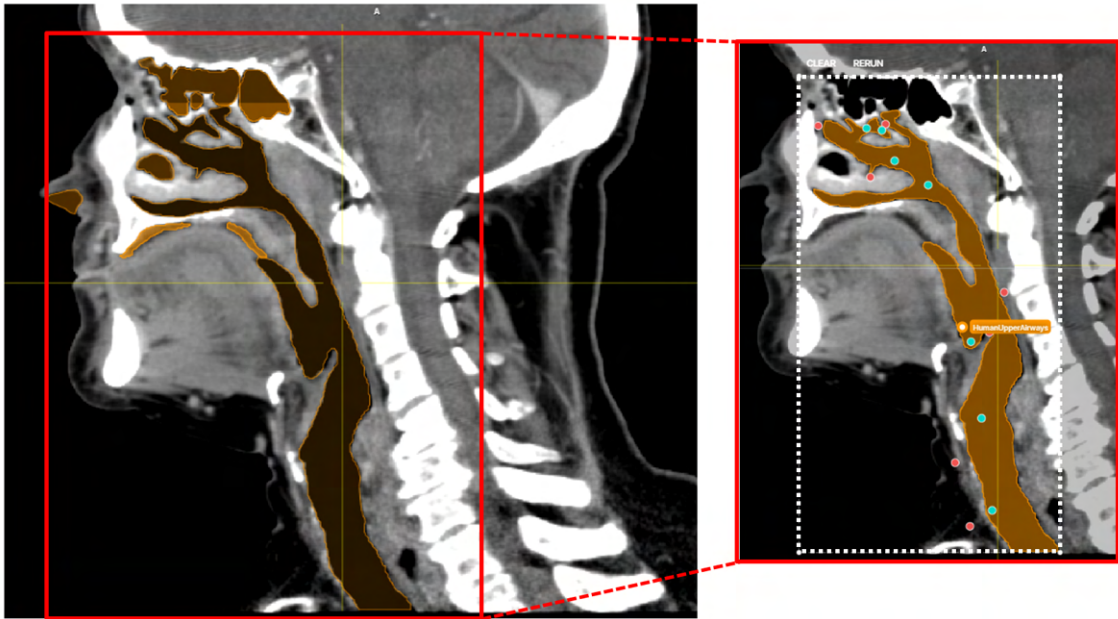


Fig. 4.2: The adjusted annotation mask of a more complex anatomical structure in the V7 software. On the left-hand side is the sagittal view of the final annotated CT slice containing fine-tuned annotations of 7 separated regions of upper airways. In the detailed picture on the right-hand side, only one annotated part is visible, demonstrating how the red and green correction dots were positioned to refine the initially imprecise annotation mask. Initially, the annotation mask was incorrectly placed in the background area under the chin. Subsequently, by placing correction dots, the upper airways area was accurately delineated.

Overall, the auto-annotate tool did not provide satisfactory and precise annotation masks. The original annotation masks of the upper airways created by the auto-annotate tool served more as a rough starting point for subsequent manual editing of the annotation mask boundaries.

A significant limitation of the V7 software was the lack of an option for propagating the annotation mask to the following slice. The annotation mask was simply copied to the following slice without any adjustment for changes in anatomy, resulting in a significant increase in annotation time.

For our specific task and desired results, the annotation of the human upper airways in the V7 software required a substantial amount of manual operations and adjustments, which were exceedingly time-consuming and prone to user-biased errors.

The estimated average time spent annotating the upper airways from a single CT scan is 150 minutes.

4.1.3 3D Slicer

Despite being a fundamental segmentation approach, thresholding proved to be highly effective for our objective of obtaining segmented upper airways models. The entire procedure was straightforward, convenient, and notably faster compared to other methods. The key aspect of this procedure lies in precisely setting the **threshold range** to cover all parts of the upper airway's anatomy. With the correct threshold range, all upper airway anatomical structures were accurately segmented, eliminating the need for any manual painting to mark missed airways structures.

The sole post-processing step involved removing unwanted parts from the original segmentation result. Since the original segmentation volume contained ear canals, lungs, and especially the surrounding background, it was necessary to remove these unwanted areas. The post-processing of the original segmentation using scissors tool was efficient and time-saving.

The estimated average time spent segmenting the upper airways from a single CT scan is 45 minutes.

4.1.4 Simpleware Software

The original segmentation results of the CMF CT tool contained numerous false-positive marked areas and structures, including the left and right lung, which were considered unwanted for the upper airways model generation. Additionally, many parts of the upper airways were missing in the original model, and the model was separated into disconnected parts (refer to Figure 4.3 for original segmentation masks and Figure 4.4 for original segmentation model). Therefore manual adjustment of the segmentation results was conducted, resulting in adjusted segmentation masks (as depicted in Figure 4.3) and adjusted segmentation model (as shown in Figure 4.4).

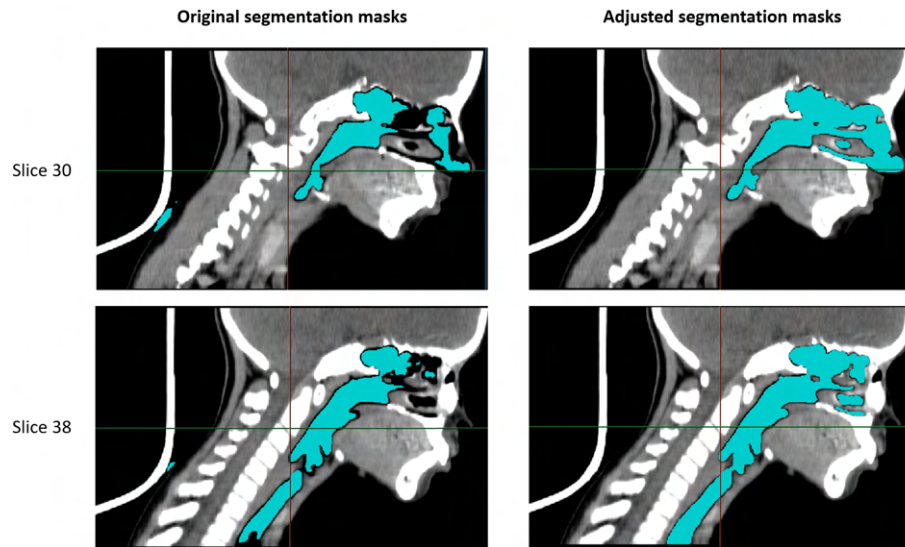


Fig. 4.3: Original and adjusted segmentation masks generated by Simpleware Software from CT scan X5_12YF. The left-hand side displays original segmentation masks (slice 30 and slice 38) showing both unwanted areas and missing parts of the upper airways. Correspondingly, the right-hand side exhibits adjusted segmentation masks for the respective slices, with missing areas filled in and unwanted areas removed.

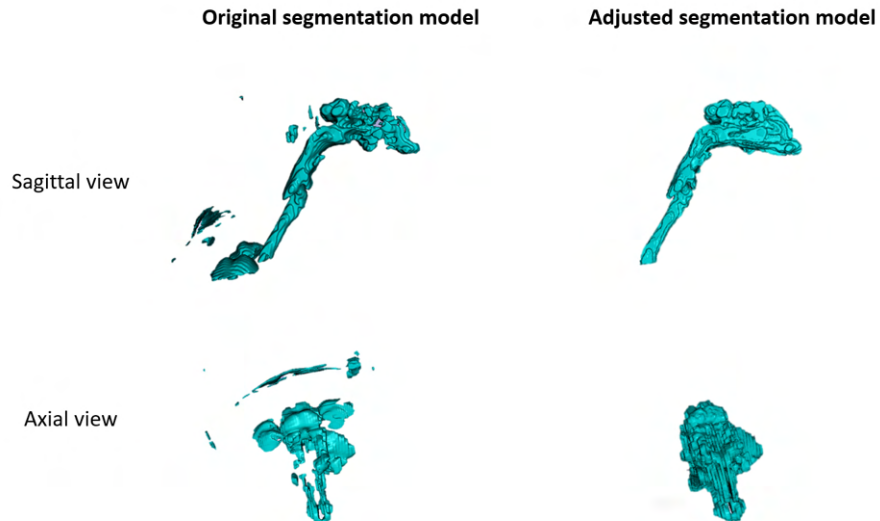


Fig. 4.4: Original and adjusted segmentation model generated by Simpleware Software from CT scan X5_12YF. The left-hand side displays the original segmentation model in sagittal and axial views, containing unwanted areas and missing parts of the upper airways. Correspondingly, the right-hand side exhibits the adjusted segmentation model in both views, with missing areas filled in and unwanted areas removed.

Overall, the original results of the CMF CT auto-segmentation tool were unsatisfactory, requiring extensive manual adjustment of segmentation masks. To understand the poor quality of the original results obtained, it is worth noting that the performance of machine learning models strongly depends on the similarity of the data used for training the ML model and the data processed by the ML model. In simple terms, the closer the processed data are to the data used to train the auto-segmentation tool, the better the results will be. In our CT scans, the interslice distance is much larger than in the training CT data, which comprised voxels of uniform size (cubic-shaped voxels).

The estimated average time spent segmenting the upper airways from a single CT scan is 120 minutes.

4.1.5 3D U-Net Model for Automatic Airway Segmentation

The original upper airway models segmented by the 3D U-Net model contained numerous false-positive marked areas and structures, such as the clearly recognizable ear canals, as depicted in Figure 4.5 illustrating the original segmentation model. These false-positive marked structures were manually removed in post-processing steps, resulting in the adjusted segmentation model shown in Figure 4.5.

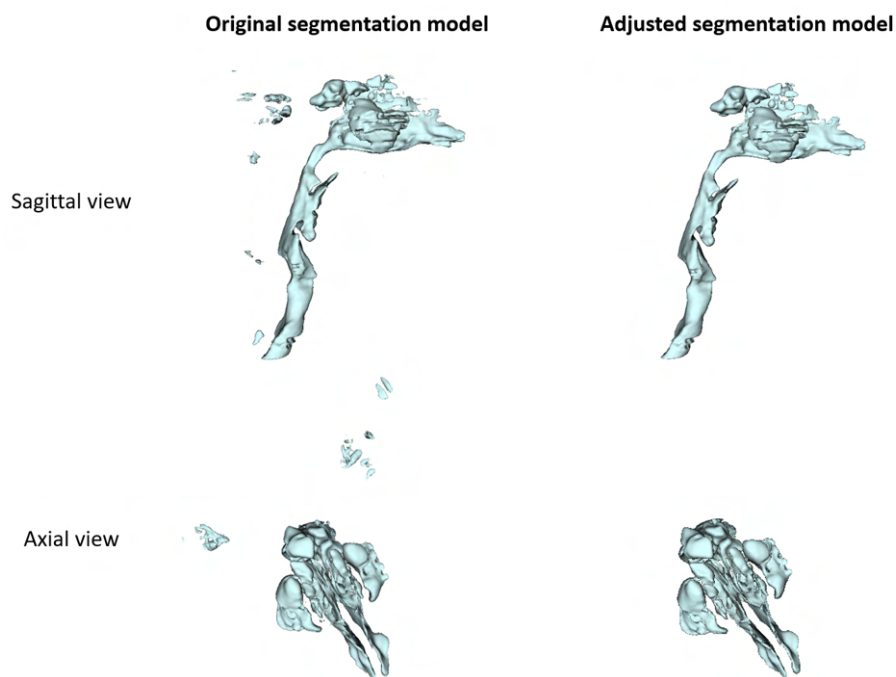


Fig. 4.5: Original and adjusted upper airway model segmented by the 3D U-Net model. The left-hand side displays the original segmentation model in sagittal and axial views, containing numerous unwanted areas. Correspondingly, the right-hand side exhibits the adjusted segmentation model in both views.

Despite the need for post-processing adjustments of the upper airway models generated by the 3D U-Net model, the entire method proved to be time-effective and convenient for the generation of 3D upper airway models.

The estimated average time spent segmenting the upper airways from a single CT scan is 15 minutes.

Regarding the original results of automatic segmentation tools (the CMF CT auto-segmentation and the 3D U-Net model method), it is worth noting that these tools are designed to serve as segmentation helper rather than fully automated segmentation solutions. Their primary purpose is to provide users with an advanced starting point for segmenting desired anatomical structures. It is expected that users will need to review and refine the segmentation to achieve the desired final result. However, these tools should significantly reduce the time required to achieve the desired segmentation compared to manual segmentation processes without automated assistance.

4.2 Spatial Registration of Models

As stated in Section 2.5, the 3D models exported from different software exhibited spatial shifts or rotations when viewed in 3D. The spatial registration of models was performed through manual manipulation and careful visual checks of the models alignment. Despite multiple fine adjustments made to ensure the best fitting alignment of the models, the final registration remains subjective. Objective spatial registration of the models can be achieved using semi-automatic or automatic registration tools, which are mathematically precise.

Semi-automatic registration is computed automatically from corresponding landmark point pairs specified on the surface of two objects. However, accurately placing landmark points at the same position in both models posed a challenge for our resulting upper airway models. Since the models created using different methods varied in shape, it was difficult to find exactly the same position on the surface of two models to place corresponding landmarks. Consequently, if the landmarks were not placed accurately in the same location on both models, the semi-automatic registration tool failed to provide precise results.

Automatic registration tools, such as the iterative closest points (ICP) algorithm, minimize the distance between corresponding point clouds to achieve convergence between a source and target point cloud. However, due to the high complexity and differences in the shapes of the models, automatic registration tools also failed to provide accurate results.

4.3 Comparative Analysis

4.3.1 Quantitative Characterization of Models' Geometry

Based on the mean values of the metrics in Table 3.7 and Figure 3.2, it is observed that the models created by the MVA method have the highest number of triangles (NoT 329480), while their model surface area is the second highest (behind Simpleware Software (521101)), and the volume of the surface model is even the third highest (behind V7 (186222) and Simpleware Software (185723)). These values suggest that the upper airway models created by the MVA method are generally smoother and contain a greater amount of detail.

For further analysis, to determine which method generated upper airway models most resembling those created by the MVA method, the mean difference and standard deviation of differences of the four investigated methods (3D Slicer, Simpleware Software, V7, and 3D U-Net model) compared to the MVA (reference) method were calculated, as shown in Table 3.8. The mean difference (in %) and standard deviation of differences (in %) were calculated for three metrics: mean number of triangles, mean model surface area, and mean volume of the surface model. The mean difference of a specific metric also provides information about the direction of the difference between the methods: a positive sign of percentage means that the method of interest provides higher values of the specific metric (overestimates), while a negative sign of percentage difference means the investigated method provides lower values of the specific metric (underestimates). For calculation of the standard deviation of differences, the values of differences between the method of interest and the reference method in the six CT scans were used.

According to Table 3.8, the upper airway models most closely resembling those created by the MVA method were created using Simpleware Software. The cause for such close results to the MVA method results is that an extensive amount of manual post-processing adjustments was used in the upper airway segmentation process using the Simpleware Software. The fine-tuning in post-processing resulted in good and complete upper airway models, but cost a large amount of working time.

4.3.2 Characterization of Models' Geometry in Relation to the Target Model

To further characterize the resulting models' geometry, the upper airway models generated by the 3D Slicer, Simpleware Software, V7, and 3D U-Net model were compared to the target models created using the MVA method.

Dice Coefficient

Based on the mean values and standard deviations of the Dice coefficient presented in Table 3.10, it was found that the 3D upper airway models generated by the **3D Slicer method** exhibited the highest mean spatial overlap (mean Dice coefficient: 88,3%) with the models generated using the MVA method.

Volume of Models Intersection and Model-to-model Distance Maps

The model-to-model distance maps, used for visualization of the shape differences between two models, can be valuable in conjunction with the volume of models intersection metric. The volume of intersection between upper airway models generated from the CT scan X1_63YF by the 3D U-Net model method and the MVA method is 69%, which is the lowest value in our results (see Table 3.11). To gain a better understanding of the anatomical areas where the two models differ the most (do not intersect), the color-coded distance model of the upper airways could be utilized. For further description, the distance map for the upper airway models generated by the 3D U-Net model method and the MVA method is show in Figure 4.6.

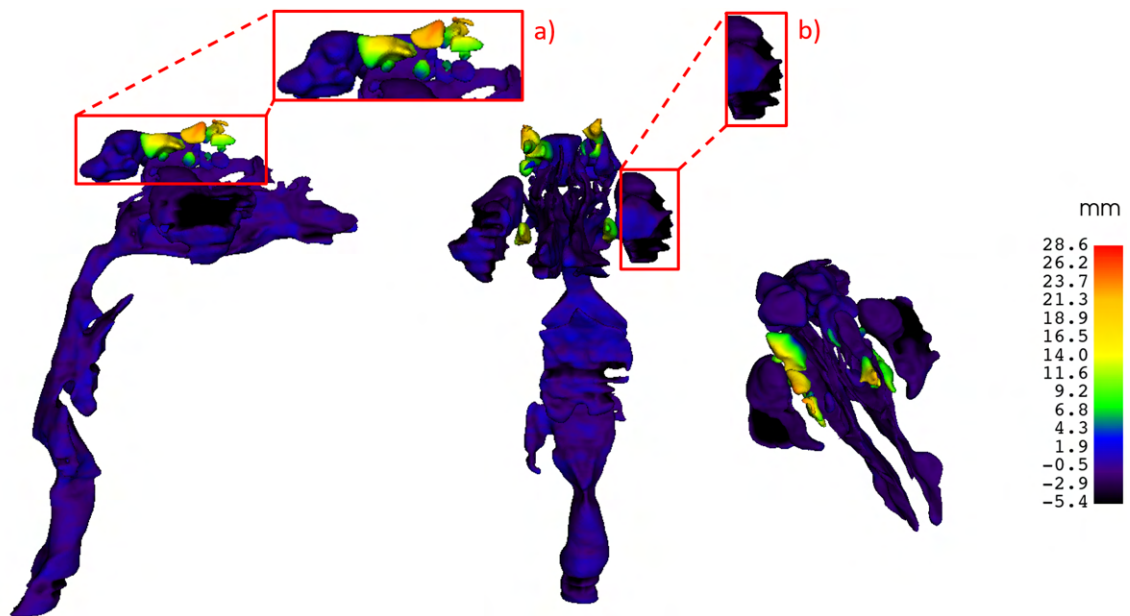


Fig. 4.6: The distance map for upper airways model generated by the 3D U-Net model method and model generated by the MVA method. The upper airway color-coded model is show in 3 views with color legend on the right hand side. The distance between models is measured in *milimeters*.

The upper airway color-coded model, depicted in Figure 4.6, describes the geometric differences between the source model, created by the 3D U-Net model

method, and the target model generated by the MVA method. The color legend (on the right-hand side of the image) explains the colors used to encode the distance between the two models.

Areas on the model surface colored dark blue/purple/black, as seen in detail b) in Figure 4.6, indicate negative distances between models. This implies that the source model is, at a given point, inside the target model. In simpler terms, the source model is narrower/smaller than the target model at certain points, or some parts of the source model are missing, resulting in a negative model-to-model distance. Conversely, areas on the distance model surface colored green/yellow/red, as seen in detail a) in Figure 4.6, indicate positive distances between the two models. This suggests that the source model exceeds the shape of the target model at certain points. In simpler terms, the source model is wider/bigger than the target model at certain points, or contains areas that are missing in the target model.

Investigation of the color-coded upper airway model, shown in Figure 4.6, may lead to a better understanding of the reason for the low intersection volume (69%) between the upper airway models created from the X1_63YF CT image by the 3D U-Net model method and the MVA method. The 69% intersection volume between the two models is due to a significant amount of missing parts (detail b) in Figure 4.6) and, conversely, some extra anatomical parts (detail a) in Figure 4.6) in the upper airway model created by the 3D U-Net model method compared to the upper airway model created by the MVA method.

4.4 Detailed Analysis of Upper Airway Models by Individual Anatomical Parts

The upper airway models created from the CT scan X1_63YF using the 3D Slicer, Simpleware Software, V7 and 3D U-Net model methods were divided into four individual anatomical parts using the same procedure. Initially, the 3D upper airway models were generated and exported from their respective software. Subsequently, these models were uploaded into the Simpleware Software and using the *3D editing tool* the models were cut into four anatomical parts. This process involved the creation of polygonal bounding box in 3D view to define the boundaries of each anatomical part. Following this, the individual anatomical parts for each model were exported separately. By employing this method, the four models were precisely divided (in 3D view) into the four anatomical parts at the same position, ensuring consistency in the delineation of anatomical parts' boundaries with a specific orientation of the cutting plane.

In contrast, the model generated by the MVA method underwent division into

the four anatomical parts directly during the CT scan annotation process. Since CT scans in the MVA method were annotated in the axial plane, simply altering the label type on the border of two anatomical parts was sufficient. This approach allowed the definition of anatomical parts' boundaries solely parallel to the axial plane, resulting in slight differences in shape compared to the anatomical parts divided using the aforementioned 3D view approach, see detailed views in Figure 4.7.

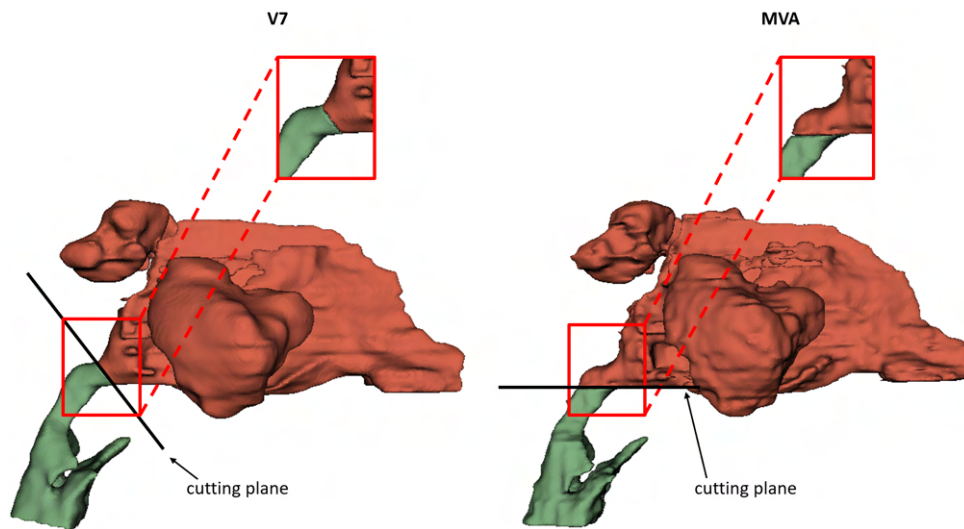


Fig. 4.7: Illustration of shape differences between the anatomical parts of the nasal cavity and sinuses and pharynx obtained by dividing upper airway models created by the V7 and MVA methods.

In Figure 4.7, the left-hand side image displays the nasal cavity with sinuses and pharynx anatomical parts obtained by dividing the upper airways model generated by the V7 method. The cutting plane, depicted by the black line, has a certain angle of orientation dividing the two anatomical parts. A detailed view of the border between these two anatomical parts is provided. In the right-hand side image, the nasal cavity with sinuses and pharynx anatomical parts obtained by dividing the upper airways model generated by the MVA method is shown. The cutting plane, parallel to the axial plane, divides the two anatomical parts. A detailed view of the border between these two anatomical parts is also provided.

The differences in shape of anatomical parts may contribute to slightly contrasting metric values when comparing anatomical parts obtained from the MVA-generated upper airways model with those from models generated using other methods. However, the results of the four different (non-MVA) methods share the same systematic bias. And therefore a comparison of the relative differences between the four different methods is still valid since they are all shifted equally.

4.4.1 Quantitative Characterization of Anatomical Parts' Geometry

The metrics, including the number of triangles, model surface area, and volume of the surface model, were calculated for each individual anatomical part of the upper airway models generated by the 5 methods. An analysis was conducted to determine which methods showed results closest to those obtained using the MVA method for each anatomical part.

From the metric values presented in Table 3.13 to Table 3.16, it was observed that the highest percentage differences were generally found in the nasal cavity and sinuses models. The closest results were noted between the MVA method and the Simpleware Software method, with differences of approximately -14.66% for NoT, -2.67% for MSA, and 4.66% for VotSM. These significant differences in the nasal cavity and sinuses anatomical models are likely caused, in addition to the shape differences described in Figure 4.7, by the intricate structure of the nasal cavity and sinuses anatomy. Specifically, the tools encounter challenges in areas where the wall between two sinuses has low contrast and the tool may connect these regions, or conversely, where the areas of the nasal cavity are too narrow and the tool may miss connecting parts.

Overall, the lowest percentage differences were observed for the trachea anatomy models. The closest results were found between the MVA method and the V7 method. The trachea anatomy models obtained from the upper airway models created by these two methods differed approximately by -1.29% for NoT, 3.21% for MSA, and 0.91% for VotSM. These similar results are attributed to the simple tube-shaped anatomy of the trachea.

4.4.2 Characterization of Anatomical Parts' Geometry in Relation to the Target Model

Dice coefficient, volume of models intersection, and model-to-model distance maps were calculated for the anatomical parts' models obtained by subdividing the upper airway models generated by the 5 methods. The anatomical parts obtained from the MVA-generated upper airways model served as the target model for these comparisons.

Dice Coefficient, Volume of Models Intersection and Model-to-model Distance Maps

For the anatomical models of the nasal cavity and sinuses, the Simpleware Software method achieved the highest Dice coefficient and volume of models intersection

values, while the model-to-model distance map showed the second narrowest range of shape distance values. Regarding the pharynx anatomical models, the V7 method attained the highest Dice coefficient and volume of models intersection values, with the model-to-model distance map displaying the second narrowest range of shape distance values. Similarly, for the larynx anatomy models, the V7 method yielded the highest Dice coefficient and volume of models intersection values, while the model-to-model distance map exhibited the second widest range of shape distance values. As for the trachea anatomical models, the Simpleware Software method achieved the highest Dice coefficient, whereas the V7 method showed the highest volume of models intersection and the second narrowest range of distance values for the model-to-model distance map.

Except for the model-to-model distance map of the nasal cavity and sinuses anatomical part, the 3D Slicer method exhibited the narrowest ranges of distance values for all other anatomical parts.

The 3D U-Net model method achieved the lowest Dice coefficient values and the lowest volume of models intersection values for all anatomical parts. Additionally, the model-to-model distance maps show that the 3D U-Net model method exhibited the widest range of distance values for the nasal cavity, pharynx, and larynx anatomical models.

4.5 CFD Simulation

Computational fluid dynamics has proven to be a very useful tool for understanding airflow dynamics within upper airway models created from patient CT scans. This tool allows physicians to simulate various airflow conditions within the upper airways, unveiling potential pathologies like obstructions or anatomical changes, all without invasive examinations. In this thesis, CFD simulation was performed on the upper airway model generated by the MVA method from the CT scan of patient X1_63YF.

4.5.1 Repair of the Model and Definition of Model Boundaries

The crucial step in CFD simulation is mesh generation. Since only error-free geometry models can be meshed, it was necessary to repair the model and define its boundaries before proceeding with meshing the upper airway model. To address errors in the upper airways model, such as overlapping regions and non-manifold geometry, MeshLab software filters were employed. Additionally, ANSYS (2024) Space Claim was utilized for defining the inlets, outlet, and walls.

4.5.2 Meshing of the Model

After repairing the model and defining its boundaries, the upper airway model underwent spatial discretization during the meshing process. ANSYS (2024) Fluent software with meshing mode was utilized for both surface and volume mesh generation. The meshed model comprised a combination of polyhedral and hexahedral elements, known as a poly-hexcore mesh. Polyhedral elements were positioned near the wall, while the inner part of the fluid region consisted of hexahedral elements. Due to the limitation of the student license of ANSYS (2024), which restricts the number of mesh elements that can be exported (1048576), it was necessary to adjust the element size to comply with the export element limit. Consequently, the final volume mesh of the upper airways model consisted of 1038236 elements.

4.5.3 CFD Simulation Computation

Based on the velocity magnitude and the absolute pressure contours, displayed in Figure 3.11, it can be argued that as the flow velocity increases, the pressure decreases. This relationship is particularly evident in the narrowest parts of the model, such as at the connection of the nasal cavity and pharynx, where the velocity reaches its highest values and the pressure drops to its lowest values.

5 Conclusion

The 3D models of the human upper airways help healthcare professionals to fully understand the intricate anatomical details of the upper airways, aiding in the detection of life-threatening pathological changes and facilitating confident therapeutic decision-making. Additionally, such 3D models can be used for simulating and assessing inner airflow characteristics within the upper airways.

In this thesis, two annotation and three segmentation methods were utilized for generating 3D upper airway models from CT scans. The dataset containing six patient CT scans was available for this work. Furthermore, different metrics, including the number of triangles, model surface area, volume of the surface model, volume of models intersection, Dice coefficient, and model-to-model distance, were calculated for all resulting 3D upper airway models, created by the five methods from the six CT scans, which were subsequently used for models characterization and methods comparison. A detailed analysis of upper airway models created from one CT scan using the five methods was performed on four anatomical parts: nasal cavity with sinuses, pharynx, larynx, and trachea.

For one of the models, computational fluid dynamics simulation of airflow in the upper airways was performed. The CFD simulation helps to understand what happens inside the airway during breathing, potentially reducing the need for invasive examinations to assess the cause and severity of respiratory tract diseases. All the steps, comprising model repair and boundaries definition, meshing of the model, and CFD simulation computation, were described, and the resulting surface and volume mesh of the model, as well as CFD results, were visualized.

The significance of this thesis lies in its potential to enhance diagnostic accuracy, treatment planning, and patient outcomes in respiratory medicine with the use of 3D upper airway models created from patient CT scans. By leveraging cutting-edge computational tools, such as computational fluid dynamics, clinicians can gain deeper insights into the underlying mechanisms of airway-related pathologies, paving the way for personalized and targeted therapeutic interventions.

Bibliography

- [1] OECD, 2018. Mortality from respiratory diseases. Online. *Health at a Glance: Europe 2018: State of Health in the EU Cycle*. S. 94 - 95. Available at: https://doi.org/10.1787/health_glance_eur-2018-12-en.
- [2] CATHAIN, Eadaoin and GAFFEY, Megan, 2024. Upper Airway Obstruction. Online. *StatPearls [Internet]*. Available at: <https://www.ncbi.nlm.nih.gov/books/NBK564399/>.
- [3] METE, Asli and AKBUDAK, İlknur Hatice. Functional Anatomy and Physiology of Airway. Online. *Tracheal Intubation*. 2018. ISBN 978-1-78923-488-6. Available at: <https://doi.org/10.5772/intechopen.77037>. [cit. 2024-01-07].
- [4] ROBINSON, Edward and FURLOW, Paul. Anatomy of the Respiratory System. Online. *Equine Respiratory Medicine and Surgery*. 2003, s. 3-17. ISBN 978-0-7020-2759-8. Available at: <https://doi.org/10.1016/B978-0-7020-2759-8.50006-4>. [cit. 2024-01-07].
- [5] *Respiratory system*. Online. In: Wikipedia.org. Available at: https://en.wikipedia.org/wiki/Respiratory_system.
- [6] FABIANO, Sarah and LEMA, Penelope. Airway Anatomy. Online. In: PAPADAKOS, Peter J. and GESTRING, Mark L. (ed.). *Encyclopedia of Trauma Care*. Berlin, Heidelberg: Springer Berlin Heidelberg, 2015, s. 93-98. ISBN 978-3-642-29611-6. Available at: https://doi.org/10.1007/978-3-642-29613-0_4. [cit. 2024-01-07].
- [7] *Lung Anatomy and Physiology*. Online. In: Wizeprep. Available at: <https://www.wizeprep.com/textbooks/undergrad/physiology/17078/sections/2331428>. [cit. 2024-01-07].
- [8] BALL, M.; HOSSAIN, M. and PADALIA, D. *Anatomy, Airway*. Online. In: StatPearls Publishing. Available at: <https://www.ncbi.nlm.nih.gov/books/NBK459258/figure/article-17308.image.f1/>. [cit. 2024-01-07].
- [9] CHAUDHRY, Raheel and BORDONI, Bruno. Anatomy, Thorax, Lungs. Online. *Treasure Island (FL): StatPearls Publishing*. 2023 Jan. Available at: <https://www.ncbi.nlm.nih.gov/books/NBK470197/>. [cit. 2024-01-08].
- [10] BRANDT, Josiah and MANDIGA, Pujyitha. Histology, Alveolar Cells. Online. *Treasure Island (FL): StatPearls Publishing*. 2023 Jan. Available at: <https://www.ncbi.nlm.nih.gov/books/NBK557542/>. [cit. 2024-01-08].

- [11] MAHABADI, Navid; GOIZUETA, Alberto and BORDON, Bruno. Anatomy, Thorax, Lung Pleura And Mediastinum. Online. *Treasure Island (FL): Stat-Pearls Publishing*. 2023 Jan. Available at: <https://www.ncbi.nlm.nih.gov/books/NBK519048/>. [cit. 2024-01-08].
- [12] JAN, Jiri. Medical Image Processing, Reconstruction and Restoration. Online. Available at: <https://doi.org/10.1201/9781420030679>. [cit. 2023-11-30].
- [13] DHANACHANDRA, Nameirakpam; MANGLEM, Khumanthem and CHANU, Yambem Jina. Image Segmentation Using K -means Clustering Algorithm and Subtractive Clustering Algorithm. Online. *Procedia Computer Science*. 2015, vol. 54, s. 764-771. ISSN 18770509. Available at: <https://doi.org/10.1016/j.procs.2015.06.090>. [cit. 2023-11-30].
- [14] HARIS, K.; EFSTRATIADIS, S.N.; MAGLAVERAS, N. and KATSAGGELLOS, A.K. Hybrid image segmentation using watersheds and fast region merging. Online. *IEEE Transactions on Image Processing*. Vol. 7, no. 12, s. 1684-1699. ISSN 10577149. Available at: <https://doi.org/10.1109/83.730380>. [cit. 2023-11-30].
- [15] BISHOP, Christopher. *Pattern recognition and machine learning*. Online. Information science and statistics. [New York]: Springer, 2006. ISBN 978-0387-31073-2. [cit. 2023-11-30].
- [16] STEWART, Matthew. *Simple Introduction to Convolutional Neural Networks*. Online. Medium. Available at: <https://towardsdatascience.com/simple-introduction-to-convolutional-neural-networks-cdf8d3077bac>. [cit. 2023-11-30].
- [17] SUMIT, Saha. *A Comprehensive Guide to Convolutional Neural Networks - the ELI5 way*. Online. Medium. Available at: <https://towardsdatascience.com/a-comprehensive-guide-to-convolutional-neural-networks-the-eli5-way-3bd2b1164a53>. [cit. 2023-11-30].
- [18] IBM. *What are convolutional neural networks?* Online. IBM. Available at: <https://www.ibm.com/topics/convolutional-neural-networks>. [cit. 2023-11-30].
- [19] AL-BATAINEH, Ali; KAUR, Devinder; AL-KHASSAWENEH, Mahmood and AL-SHAROA, Esraa. Automated CNN Architectural Design: A Simple and Efficient Methodology for Computer Vision Tasks. Online. *Mathematics*. 2023, vol. 11, no. 5. ISSN 2227-7390. Available at: <https://doi.org/10.3390/math11051141>. [cit. 2024-01-06].

- [20] RONNEBERGER, Olaf; FISCHER, Philipp and BROX, Thomas. U-Net: Convolutional Networks for Biomedical Image Segmentation. Online. *Medical Image Computing and Computer-Assisted Intervention - MICCAI 2015*. Lecture Notes in Computer Science. 2015, s. 234-241. ISBN 978-3-319-24573-7. Available at: https://doi.org/10.1007/978-3-319-24574-4_28. [cit. 2024-01-06].
- [21] LIU, Xiangbin; SONG, Liping; LIU, Shuai and ZHANG, Yudong. A Review of Deep-Learning-Based Medical Image Segmentation Methods. Online. *Sustainability*. 2021, vol. 13, no. 3. ISSN 2071-1050. Available at: <https://doi.org/10.3390/su13031224>. [cit. 2023-11-30].
- [22] TAHA, Abdel Aziz and HANBURY, Allan. Metrics for evaluating 3D medical image segmentation: analysis, selection, and tool. Online. *BMC Medical Imaging*. 2015, vol. 15, no. 1. ISSN 1471-2342. Available at: <https://doi.org/10.1186/s12880-015-0068-x>. [cit. 2023-11-30].
- [23] YEGHIAZARYAN, Varduhi a VOICULESCU, Irina. Family of boundary overlap metrics for the evaluation of medical image segmentation. Online. *Journal of Medical Imaging*. 2018, vol. 5, no. 01. ISSN 2329-4302. Available at: <https://doi.org/10.1117/1.JMI.5.1.015006>. [cit. 2024-01-06].
- [24] SUPERANNOTATE, 2022. *What is image annotation? Introduction to image annotation for machine learning*. Online. Available at: <https://www.superannotate.com/blog/introduction-to-image-annotation>.
- [25] DATAGEN, 2024. *Image Annotation for Computer Vision: A Practical Guide*. Online. Available at: <https://datagen.tech/guides/image-annotation/image-annotation/#>.
- [26] CLOUDFACTORY, 2024. *Image Annotation for Computer Vision: A Guide to Labeling Visual Data for Your Machine Learning Project*. Online. Available at: <https://www.cloudfactory.com/image-annotation-guide#Types-of-Image-Annotation3>.
- [27] BANDYOPADHYAY, Hmrishav, 2023. *Image Annotation: Definition, Use Cases and Types*. Online. Available at: <https://www.v7labs.com/blog/image-annotation-guide>.
- [28] FAIZAL, W. M.; GHAZALI, N.; KHOR, C. Y.; BADRUDDIN, Irfan Anjum; ZAINON, M. Z. et al. Computational fluid dynamics modelling of human upper airway: A review. Online. *Computer Methods and Programs in Biomedicine*. 2020, vol. 196. ISSN 01692607. Available at: <https://doi.org/10.1016/j.cmpb.2020.105627>. [cit. 2023-12-11].

- [29] JAMES AYODELE, Oyejide; EBENEZER OLUWATOSIN, Atoyebi; CHRISTIAN TAIWO, Olutosoye and ADEBUKOLA DARE, Ademola. Computational Fluid Dynamics Modeling in Respiratory Airways Obstruction. Online. *International Journal of Biomedical Science and Engineering*. 2021, vol. 9, no. 2. ISSN 2376-7227. Available at: <https://doi.org/10.11648/j.ijbse.20210902.12>. [cit. 2023-12-12].
- [30] LIN, Shengmao; PREMARAJ, Thyagaseely Sheela; GAMAGE, Peshala; DONG, Pengfei; PREMARAJ, Sundaralingam et al., 2022. Upper Airway Flow Dynamics in Obstructive Sleep Apnea Patients with Various Apnea-Hypopnea Index. Online. In: *Life*. Available at: <https://doi.org/10.3390/life12071080>.
- [31] *Medical Volume Annotator*, 2023. Online. Medical Volume Annotator. Available at: <https://www.mva.ai/>.
- [32] V7. *A Complete Toolkit for DICOM Annotation and Medical Image Analysis*. Online. V7. Available at: <https://www.v7labs.com/dicom-annotation-tools>.
- [33] *3D Slicer*. Online. 3D Slicer. 2024-03-28. Available at: <https://www.slicer.org/>.
- [34] GREENWAY; SHARMA and VARGAS CARVAJAL. Radiopaedia.org: Hounsfield unit. Online. In: *Radiopaedia.org*. Available at: <https://doi.org/10.53347/rID-38181>.
- [35] ORHAN, Kaan; SHAMSHIEV, Mamat; EZHOV, Matvey; PLAKSIN, Alexander; KURBANOVA, Aida et al. AI-based automatic segmentation of cranio-maxillofacial anatomy from CBCT scans for automatic detection of pharyngeal airway evaluations in OSA patients. Online. *Scientific Reports*. 2022, vol. 12, no. 1. ISSN 2045-2322. Available at: <https://doi.org/10.1038/s41598-022-15920-1>. [cit. 2023-12-01].
- [36] GARCIA-UCEDA, Antonio; SELVAN, Raghavendra; SAGHIR, Zaigham; TIDDENS, Harm A. and DE BRUIJNE, Marleen. Automatic airway segmentation from computed tomography using robust and efficient 3-D convolutional neural networks. Online. *Scientific Reports*. 2021, vol. 11, no. 1. ISSN 2045-2322. Available at: <https://doi.org/10.1038/s41598-021-95364-1>. [cit. 2023-12-01].
- [37] VINAYAHALINGAM, Shankeeth; BERENDS, Bo; BAAN, Frank; MOIN, David Anssari; VAN LUIJN, Rik et al. Deep learning for automated segmentation of the temporomandibular joint. Online. *Journal of Dentistry*. 2023, vol.

132. ISSN 03005712. Available at: <https://doi.org/10.1016/j.jdent.2023.104475>. [cit. 2023-12-01].
- [38] FONTENELE, Rocharles Cavalcante; GERHARDT, Maurício do Nascimento; PICOLI, Fernando Fortes; VAN-GERVEN, Adriaan; NOMIDIS, Stefanos et al. Convolutional neural network-based automated maxillary alveolar bone segmentation on cone-beam computed tomography images. Online. *Clinical Oral Implants Research*. 2023, vol. 34, no. 6, s. 565-574. ISSN 0905-7161. Available at: <https://doi.org/10.1111/clr.14063>. [cit. 2023-12-02].
- [39] SYNOPSISYS, 2024. *Simpleware Software Solutions*. Online. Synopsys. Available at: <https://www.synopsys.com/simpleware.html>.
- [40] KHOSS, Niklas, 2023. *Automatic Segmentation of the Upper Respiratory Airways using CT Scans*. Master Thesis. Wien: FH Technikum Wien.

List of Figures

1.1	Scheme of human respiratory system [5].	10
1.2	Human upper airway system.	11
1.3	Human lower airway system and bronchioli.	13
1.4	CNN architecture scheme.	19
1.5	U-net architecture.	20
1.6	Types of image annotation [26].	23
1.7	Types of image segmentation [27].	25
1.8	Computational fluid dynamics scheme [30].	28
2.1	Scheme of general workflow.	30
2.2	The MVA superpixel mesh with different size of elements.	33
2.3	The 3D Slicer user-interface for the segment editor module.	36
2.4	Segmentation results after applying the threshold tool in 3D Slicer.	37
2.5	The final adjusted segmentation results in 3D Slicer.	38
2.6	User-interface of Simpleware Software and model of head and neck defining anatomical structures for segmentation.	39
2.7	The original segmentation mask created by the 3D U-Net model for one CT slice.	41
2.8	The upper airways model divided into 4 anatomical parts.	44
2.9	Defined model's boundaries.	46
3.1	Table of resulting 3D upper airway models for CT scan of patient X1_63YF.	48
3.2	Graph of the mean values of the number of triangles, model surface area and volume of the surface model metrics for the 5 methods.	52
3.3	The model-to-model distance maps created for upper airway models generated from CT scan X1_63YF using the 5 methods.	57
3.4	The 5 upper airway models divided into 4 individual anatomical parts.	58
3.5	The model-to-model distance maps created for nasal cavity and si- nuses geometry models.	63
3.6	The model-to-model distance maps created for pharynx geometry models.	63
3.7	The model-to-model distance maps created for larynx geometry models.	64
3.8	The model-to-model distance maps created for trachea geometry mod- els.	65
3.9	The surface and volume mesh generated for the 3D upper airways model.	66
3.10	The absolute pressure contour model in 4 views.	67
3.11	The velocity magnitude and absolute pressure contours in cross-section.	67

4.1	Accurately labeled maxillary sinus area by the auto-annotate tool in the V7 software.	70
4.2	The adjusted annotation mask of a more complex anatomical structure in the V7 software.	71
4.3	Original and adjusted segmentation masks generated by Simpleware Software.	73
4.4	Original and adjusted segmentation model generated by Simpleware Software.	73
4.5	Original and adjusted upper airway model segmented by the 3D U-Net model.	74
4.6	The distance map for the upper airways model generated by the 3D U-Net model method and model generated by the MVA method. . . .	77
4.7	Illustration of shape differences between the anatomical parts of the nasal cavity and sinuses and pharynx obtained by dividing upper airway models created by the V7 and MVA methods.	79
5.1	Table of resulting 3D upper airway models for CT scan of patient X2_59YM.	94
5.2	Table of resulting 3D upper airway models for CT scan of patient X3_15YM.	95
5.3	Table of resulting 3D upper airway models for CT scan of patient X4_17YF.	96
5.4	Table of resulting 3D upper airway models for CT scan of patient X5_12YF.	97
5.5	Table of resulting 3D upper airway models for CT scan of patient X6_7YM.	98
5.6	The model-to-model distance maps created for upper airway models generated from CT scan X2_59YM using the 5 methods.	99
5.7	The model-to-model distance maps created for upper airway models generated from CT scan X3_15YM using the 5 methods.	100
5.8	The model-to-model distance maps created for upper airway models generated from CT scan X4_17YF using the 5 methods.	101
5.9	The model-to-model distance maps created for upper airway models generated from CT scan X5_12YF using the 5 methods.	102
5.10	The model-to-model distance maps created for upper airway models generated from CT scan X6_7YM using the 5 methods.	103

List of Tables

2.1	Table with selected metadata for 6 CT scans.	31
3.1	Table of metrics for the quantitative characterization of the resulting models' geometry - CT scan of patient X1_63YF	49
3.2	Table of metrics for the quantitative characterization of the resulting models' geometry - CT scan of patient X2_59YM	50
3.3	Table of metrics for the quantitative characterization of the resulting models' geometry - CT scan of patient X3_15YM	50
3.4	Table of metrics for the quantitative characterization of the resulting models' geometry - CT scan of patient X4_17YF	50
3.5	Table of metrics for the quantitative characterization of the resulting models' geometry - CT scan of patient X5_12YF	51
3.6	Table of metrics for the quantitative characterization of the resulting models' geometry - CT scan of patient X6_7YM	51
3.7	Table of the mean values of the 3 metrics for the 5 methods.	51
3.8	Table of the mean difference and standard deviation of differences calculated for the three quantitative metrics.	52
3.9	Table of Dice coefficients calculated for all the upper airway models created from the 6 CT scans.	53
3.10	Table of mean values and standard deviations of the Dice coefficients for each method.	54
3.11	Table of the volume of models intersection metric (in %) calculated for all the upper airway models created from the 6 CT scans.	55
3.12	Table of mean values (in %) and standard deviations of the volume of models intersection for each method.	55
3.13	Table of metrics for the quantitative characterization of the nasal cavity and sinuses geometry.	59
3.14	Table of metrics for the quantitative characterization of the pharynx geometry.	59
3.15	Table of metrics for the quantitative characterization of the larynx geometry.	60
3.16	Table of metrics for the quantitative characterization of the trachea geometry.	60
3.17	Table of Dice coefficients calculated for all the anatomical parts' models.	61
3.18	Table of volume of models intersectio calculated for all the anatomical parts' models.	62

List of Abbreviations

CT	Computed Tomography
CFD	Computational Fluid Dynamics
MRI	Magnetic Resonance Imaging
HUA	Human Upper Airway
UAS	Upper Airway System
LAS	Lower Airway System
ML	Machine Learning
AI	Artificial Intelligence
CNN	Convolutional Neural Network
SVM	Support Vector Machine
DSC	Dice Similarity Coefficient
IoU	Intersection over Union
ASSD	Average Symmetric Surface Distance
DICOM	Digital Imaging and Communications in Medicine
NIfTI	Neuroimaging Informatics Technology Initiative
STL	Stereolithography
MVA	Medical Volume Annotator
CMF	Craniomaxillofacial
Not	Number of Triangles
MSA	Model Surface Area
VotSM	Volume of the Surface Model
ICP	Iterative Closest Points

Appendix

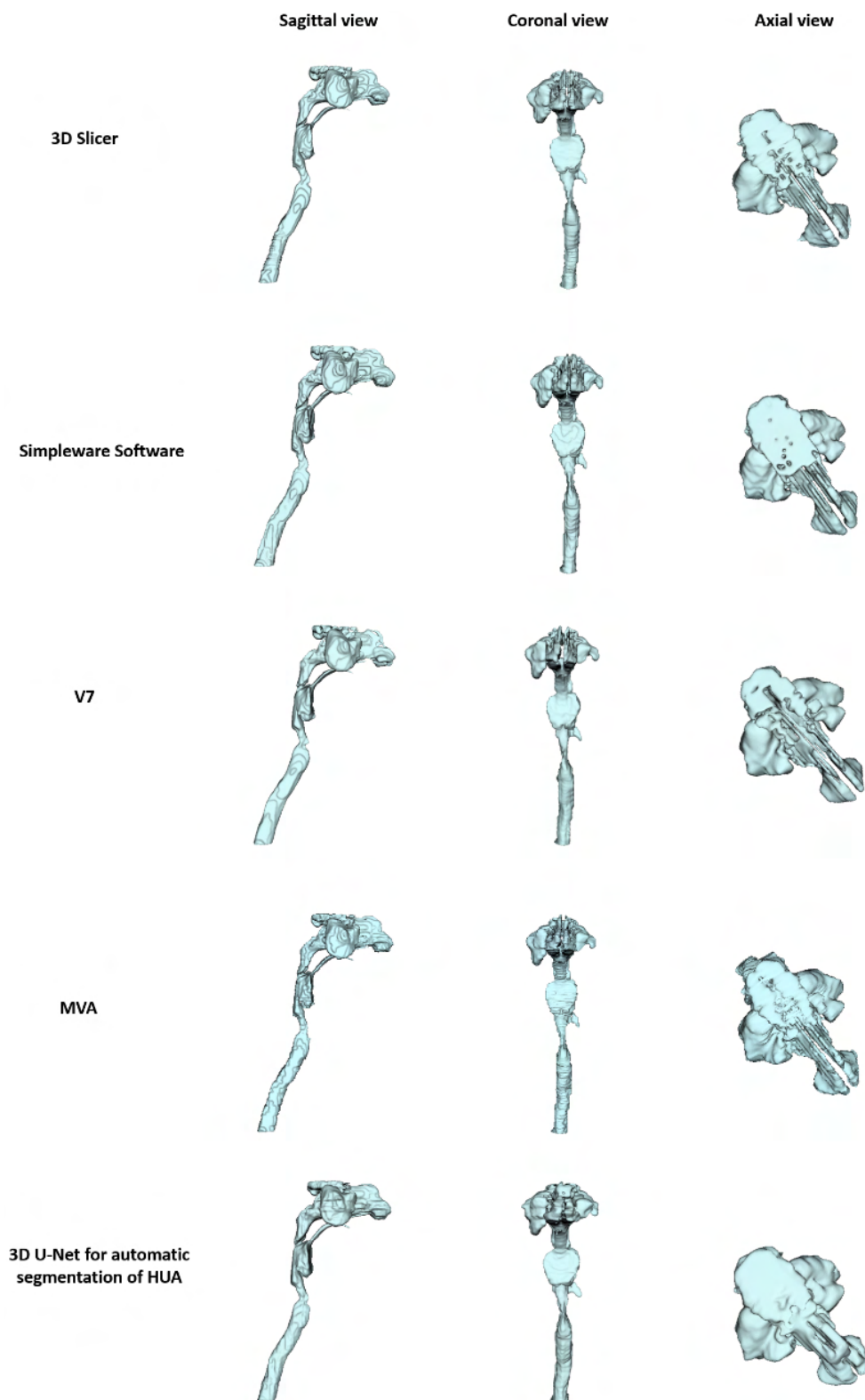


Fig. 5.1: Table of resulting 3D upper airway models for CT scan of patient X2_59YM. Models obtained by all the 5 methods are shown in 3 views: sagittal, coronal, and axial.

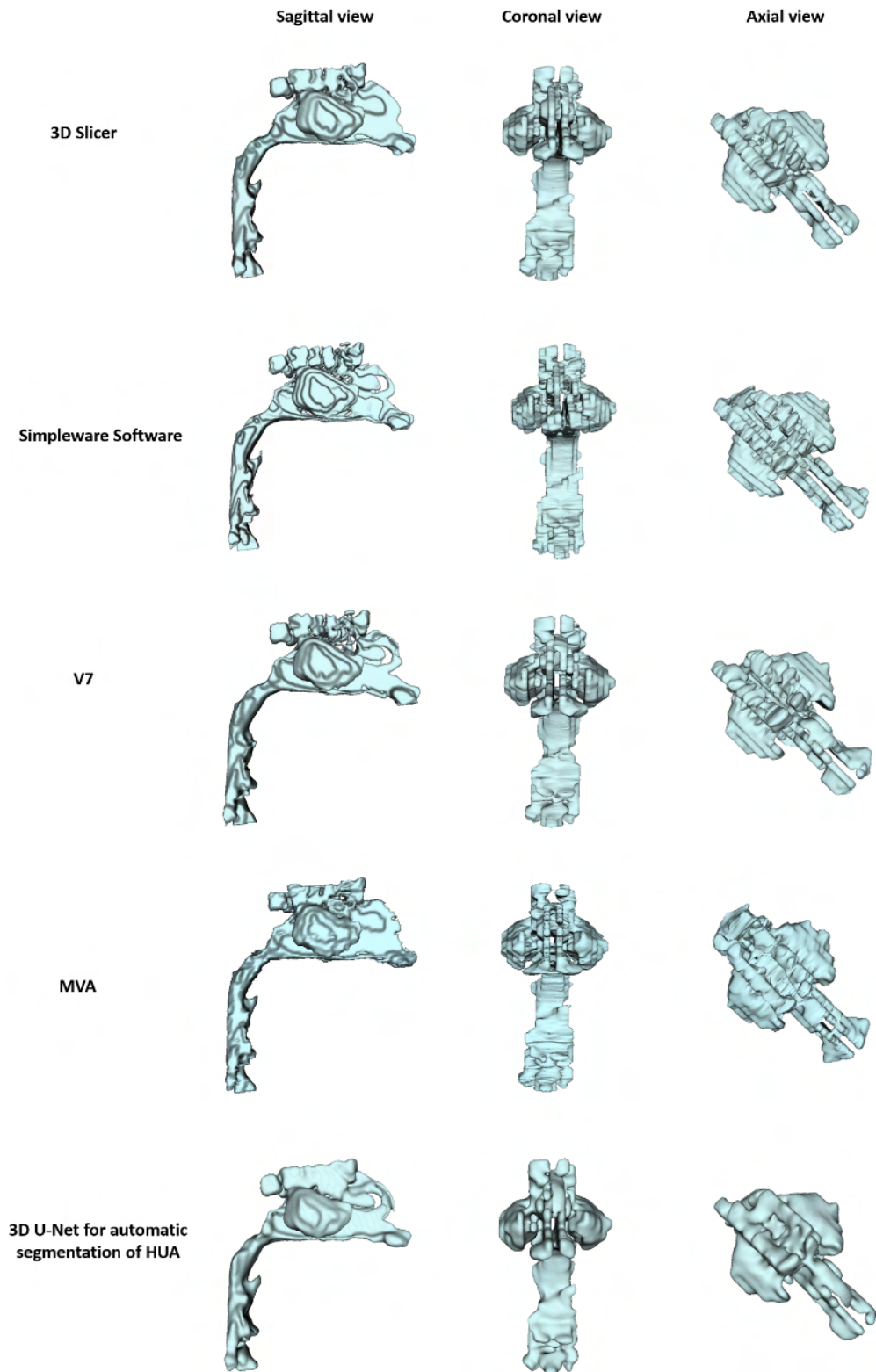


Fig. 5.2: Table of resulting 3D upper airway models for CT scan of patient X3_15YM. Models obtained by all the 5 methods are shown in 3 views: sagittal, coronal, and axial.

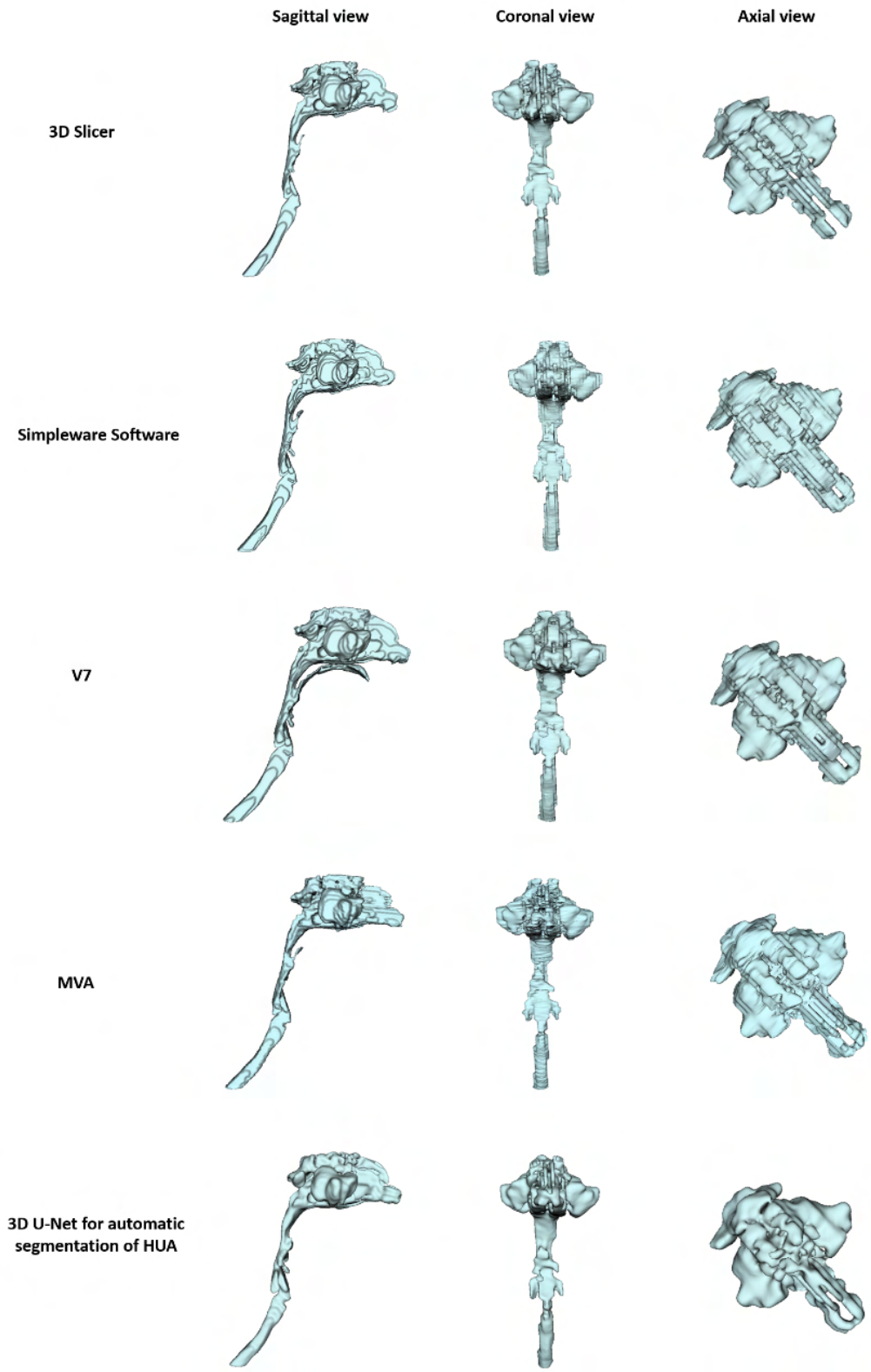


Fig. 5.3: Table of resulting 3D upper airway models for CT scan of patient X4_17YF. Models obtained by all the 5 methods are shown in 3 views: sagittal, coronal, and axial.

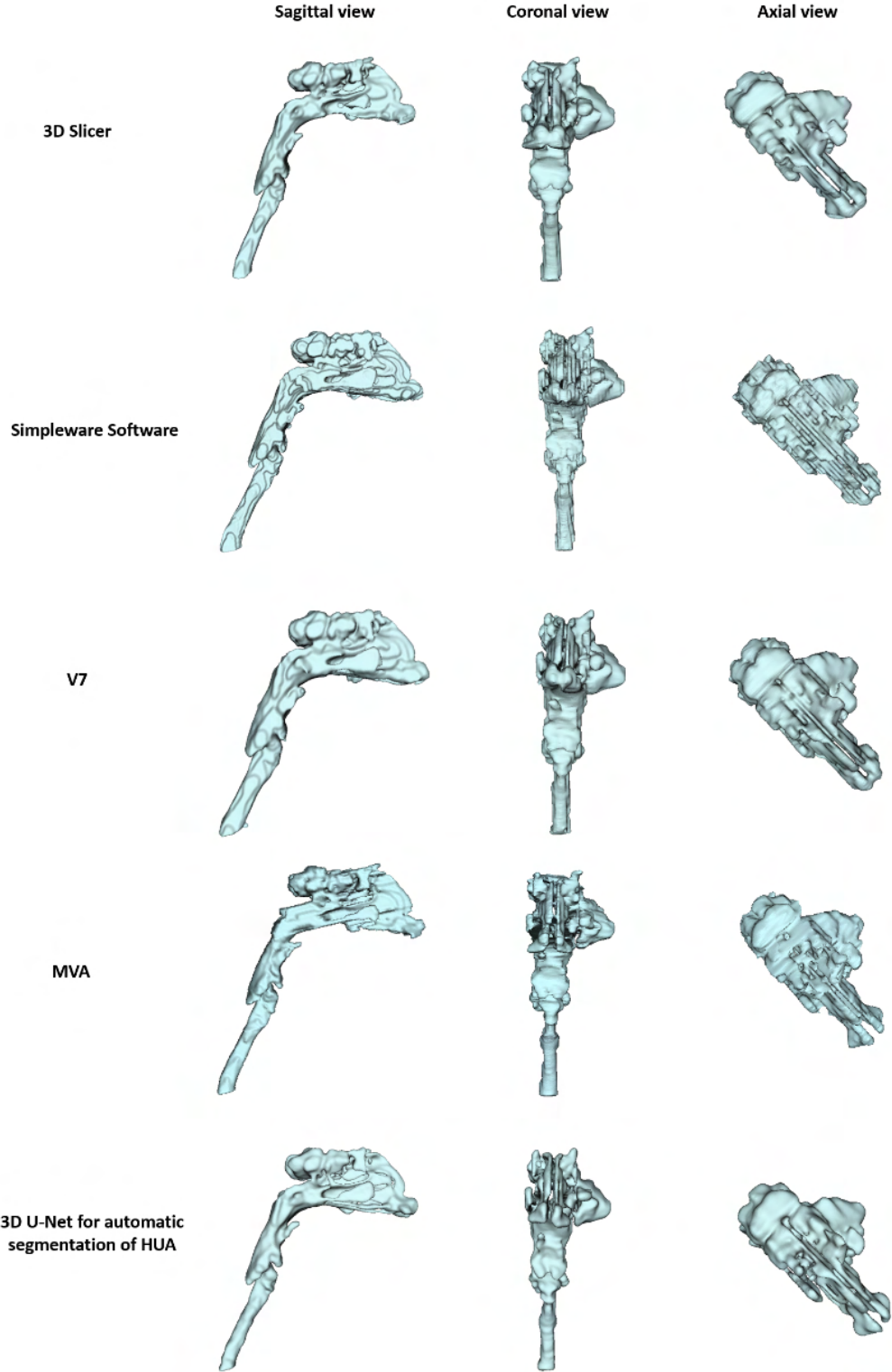


Fig. 5.4: Table of resulting 3D upper airway models for CT scan of patient X5_12YF. Models obtained by all the 5 methods are shown in 3 views: sagittal, coronal, and axial.

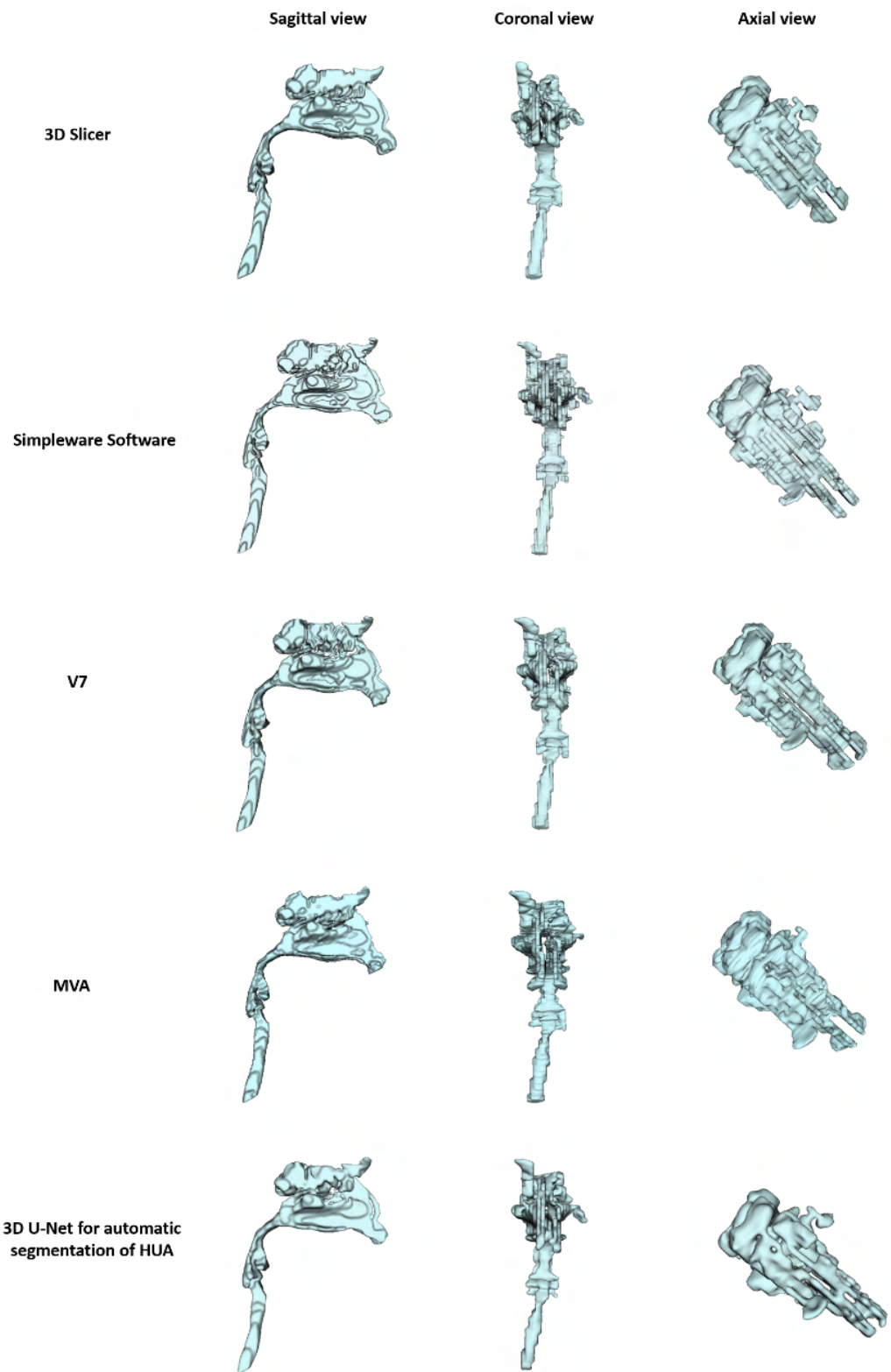


Fig. 5.5: Table of resulting 3D upper airway models for CT scan of patient X6_7YM. Models obtained by all the 5 methods are shown in 3 views: sagittal, coronal, and axial.

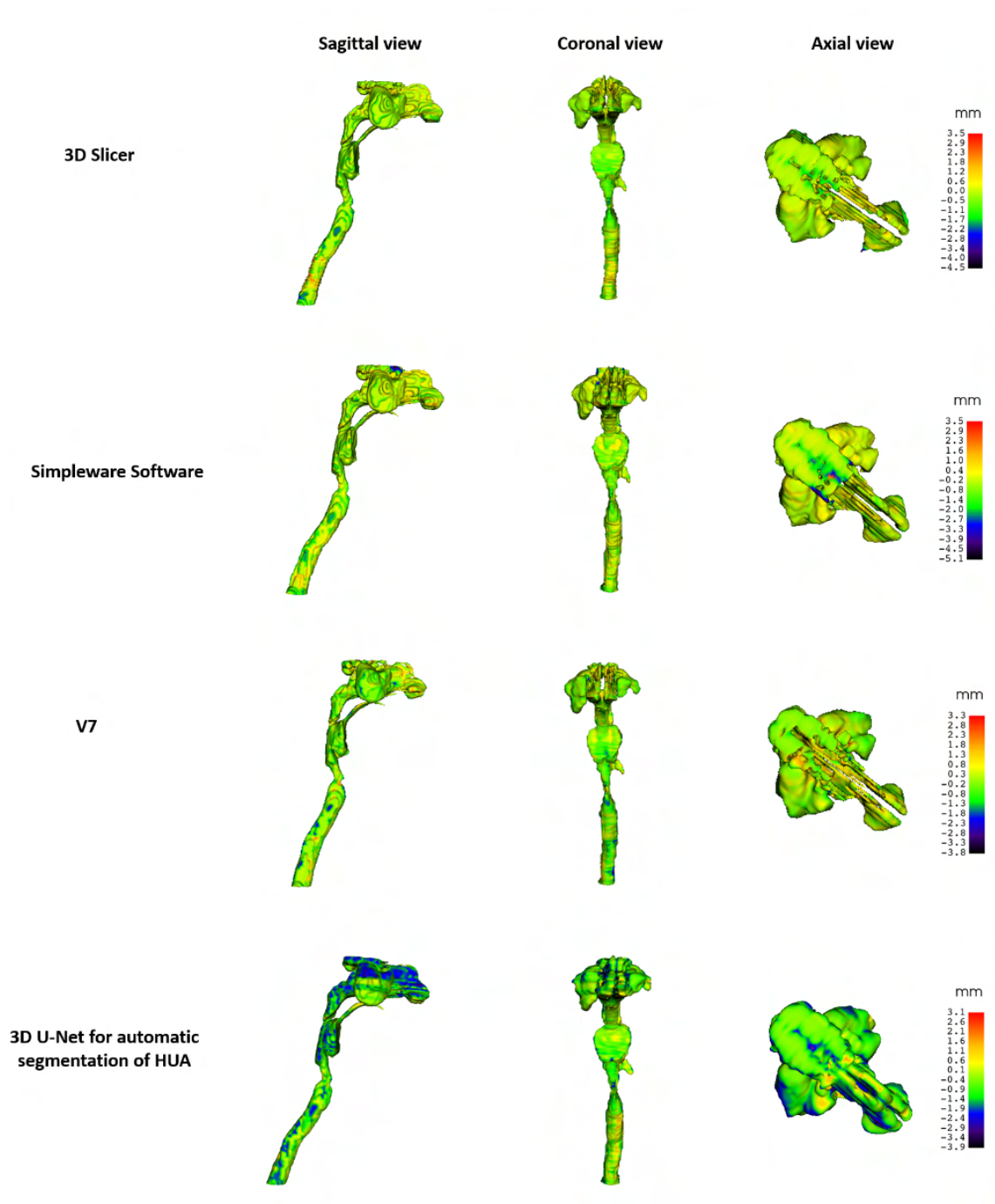


Fig. 5.6: The model-to-model distance maps created for upper airway models generated from CT scan X2_59YM using the 5 methods. The color-coded upper airway models are presented in sagittal, coronal and axial views. For each color-coded upper airway model is shown color scale explaining color coding of shape distances between models.

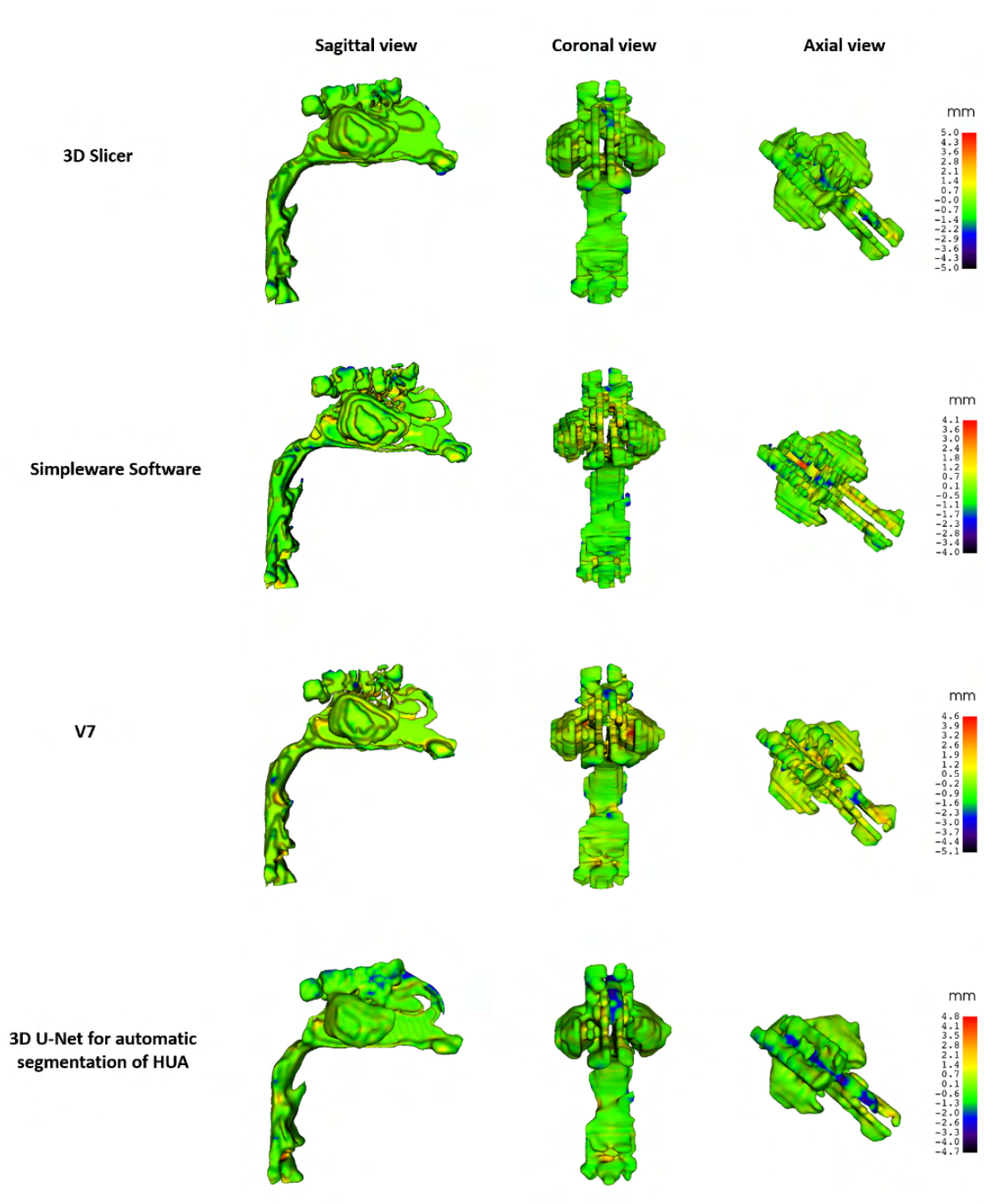


Fig. 5.7: The model-to-model distance maps created for upper airway models generated from CT scan X3_15YM using the 5 methods. The color-coded upper airway models are presented in sagittal, coronal and axial views. For each color-coded upper airway model is shown color scale explaining color coding of shape distances between models.

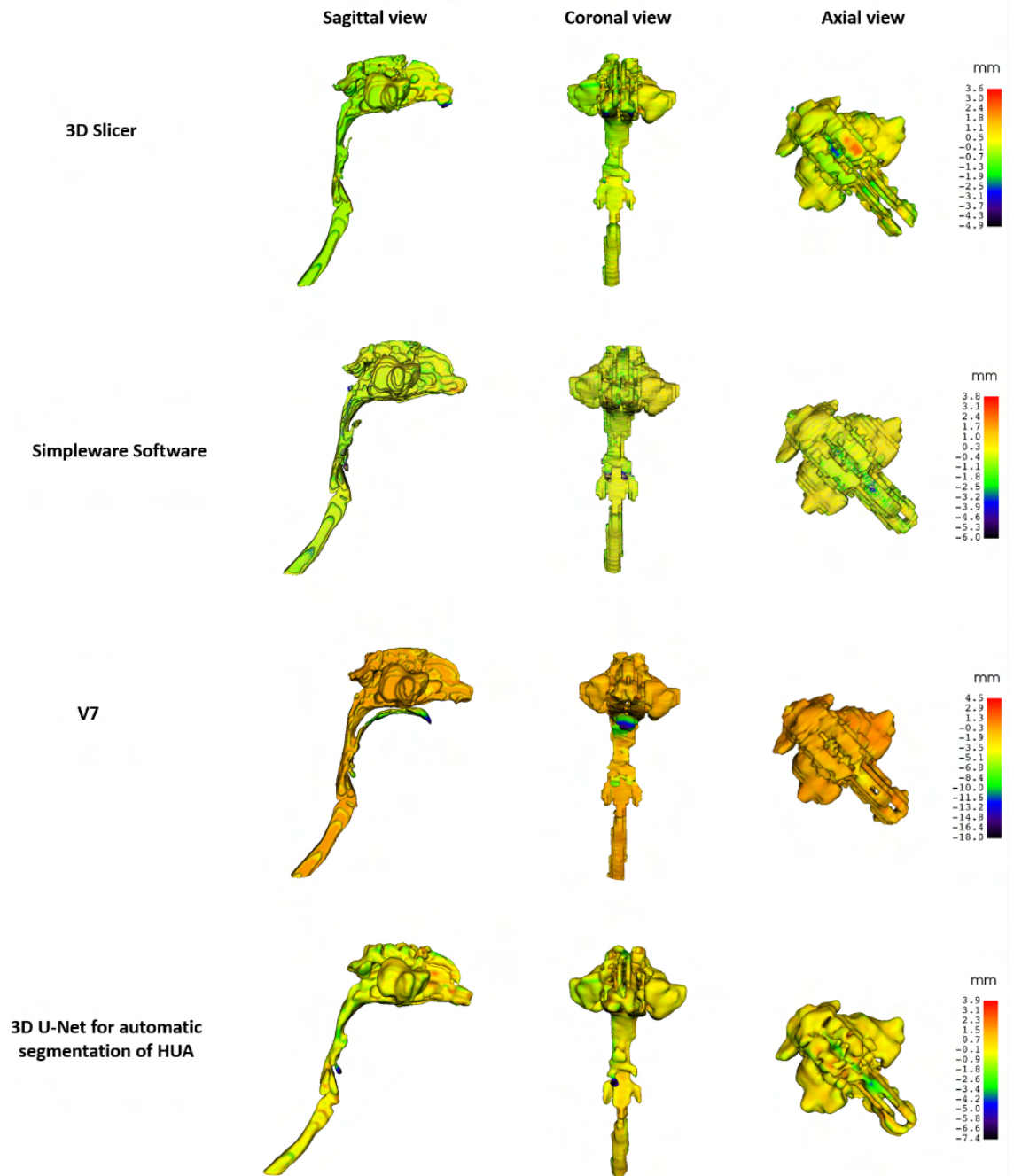


Fig. 5.8: The model-to-model distance maps created for upper airway models generated from CT scan X4_17YF using the 5 methods. The color-coded upper airway models are presented in sagittal, coronal and axial views. For each color-coded upper airway model is shown color scale explaining color coding of shape distances between models.

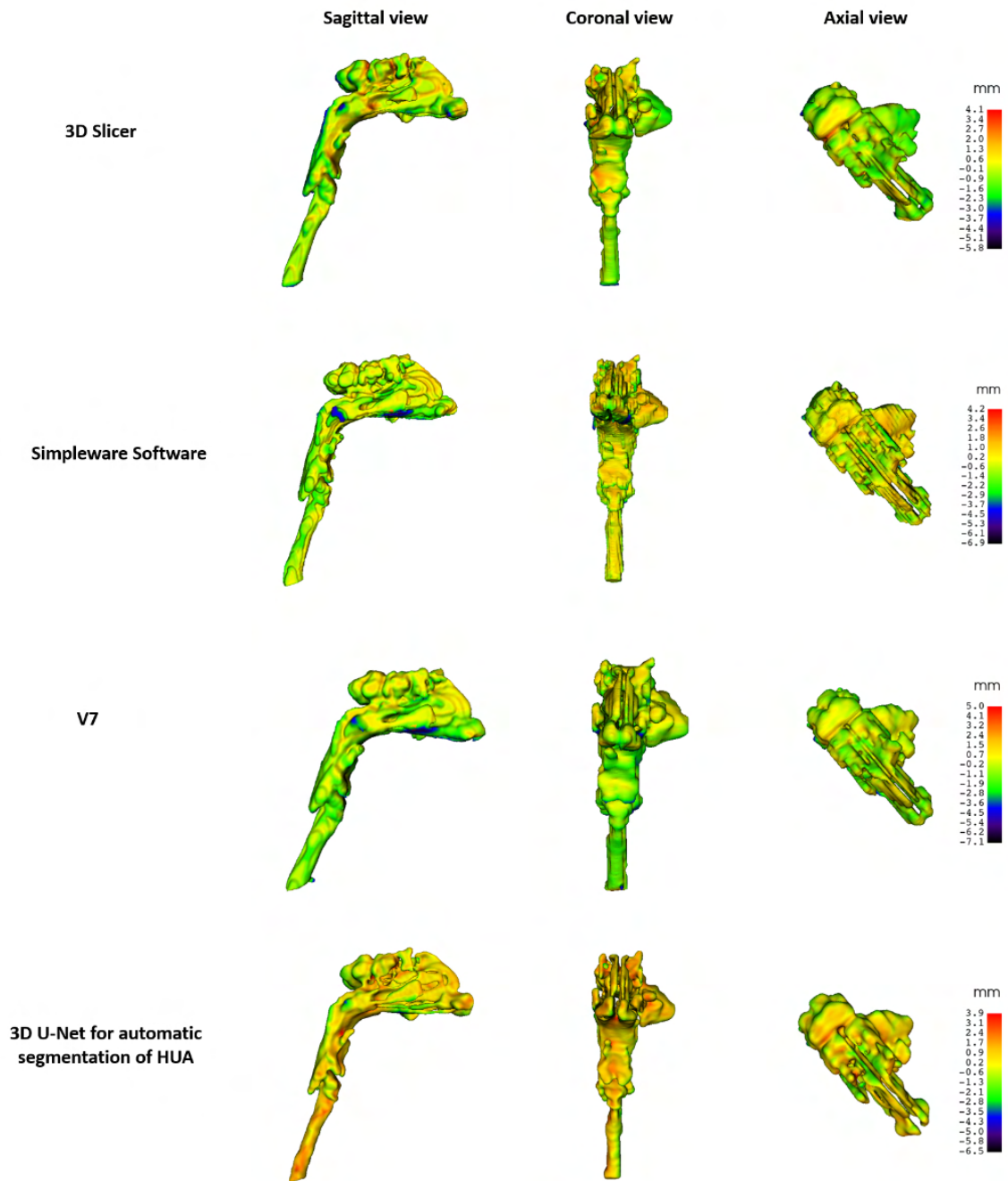


Fig. 5.9: The model-to-model distance maps created for upper airway models generated from CT scan X5_12YF using the 5 methods. The color-coded upper airway models are presented in sagittal, coronal and axial views. For each color-coded upper airway model is shown color scale explaining color coding of shape distances between models.

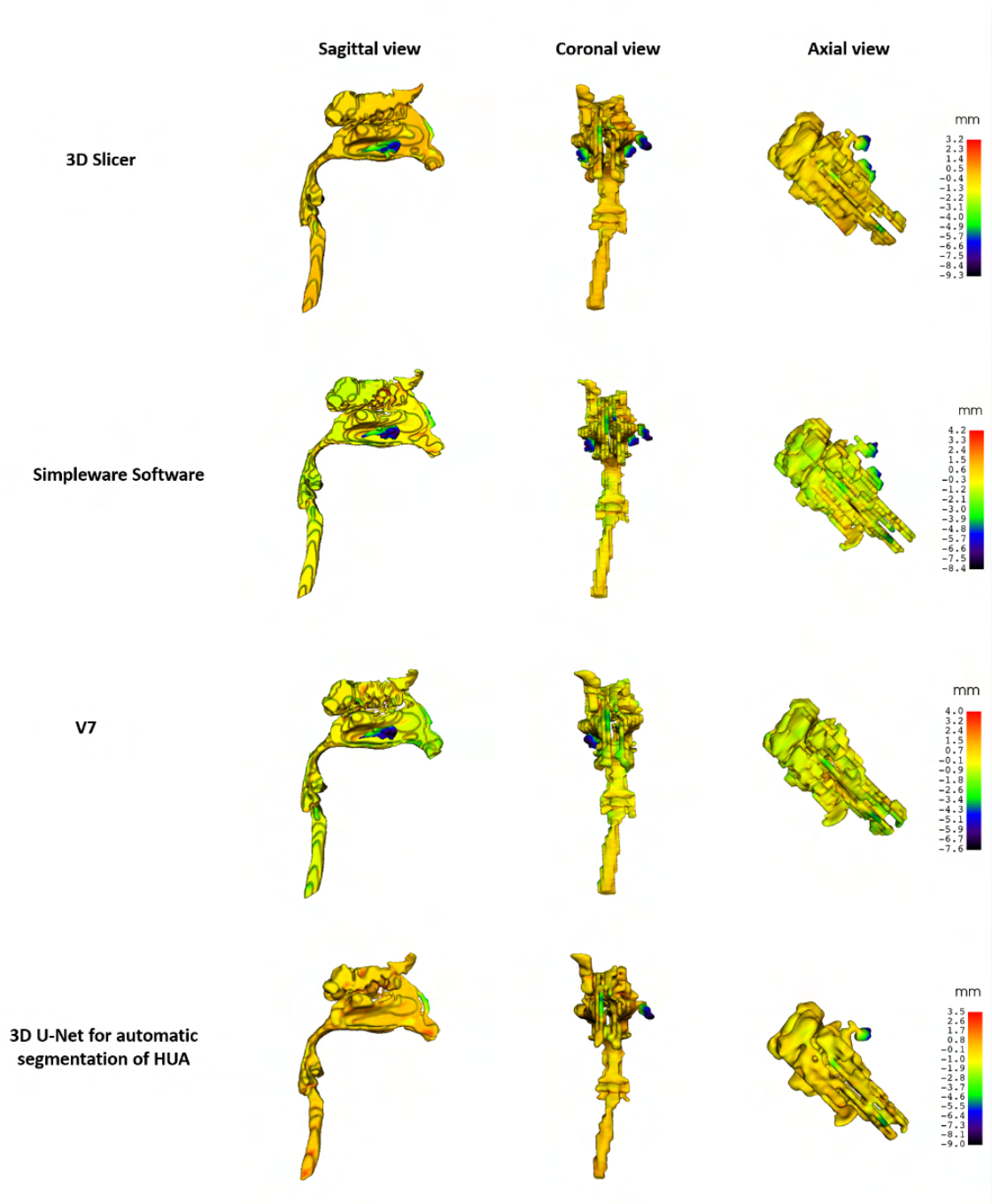


Fig. 5.10: The model-to-model distance maps created for upper airway models generated from CT scan X6_7YM using the 5 methods. The color-coded upper airway models are presented in sagittal, coronal and axial views. For each color-coded upper airway model is shown color scale explaining color coding of shape distances between models.